Title

The Spectroscopic-Assisted Studies on Photophysics and Mechanochemistry of Anthracene-Based Materials

Author

Zhou, Xiaoquan

Publication Date

2012

UNIVERSITY OF CALIFORNIA
RIVERSIDE

Spectroscopic-Assisted Studies on the Photophysics and Mechanochemistry of Anthracene-Based Materials

A Dissertation submitted in partial satisfaction
of the requirements for the degree of

Doctor of Philosophy

in

Chemistry

by

Xiaoquan Zhou

March 2013

Dissertation Committee:
- Dr. Christopher J. Bardeen, Chairperson
- Dr. Jingsong Zhang
- Dr. Chia-En Angelina Chang

The Dissertation of Xiaoquan Zhou is approved:

Committee Chairperson

University of California, Riverside

Acknowledgements

First, I would like to thank my advisor Professor Christopher J. Bardeen for all of the guidance and help he has provided during the past five years. He teaches me how to organize our research plans and complete our projects step by step. Thanks to the intellect and enthusiasm he brings to the lab, we have endeavored to explore in chemistry. I would also like to acknowledge and thank all the other members of our group: Dr. Jon Burdett and Robert Dillon helped me with the laser set-up of the time-resolved fluorescence measurements; Geoff Piland provided the theoretical calculation for my project; Rabih O. Al-Kaysi gave me important suggestions for organic synthesis; Dr. Kathryn Colby offered me a grammar review for my thesis. I cannot complete the road to a Ph.D. without their help. Thanks to my committee members and staff members of the chemistry department for the help they provided in preparing this dissertation.

I would offer a special thanks to my family for their understanding, love and support. Especially, to my husband, who came to my life during the past years in Riverside, and has brought much more sunshine and happiness to my life.

ABSTRACT OF THE DISSERTATION

The Spectroscopic-Assisted Studies on Photophysics and Mechanochemistry of Anthracene-Based Materials

by

Xiaoquan Zhou

Doctor of Philosophy, Graduate Program in Chemistry
University of California, Riverside, March 2013
Dr. Christopher J. Bardeen, Chiarperson

A series of 2,6-dialkoxyanthracenes are synthesized and their photophysical properties in liquid solution and solid state are studied. Both spectral lineshapes and luminescence decay kinetics of these molecules in dilute solution or in a polymer matrix are identical. We identify a conformational change in solution that leads to two emissive states that can interconvert. In the solid state, the crystal structures of 2,6-dialkoxyanthracenes change significantly with lengthening alkoxy chains from methoxy to hexyloxy, evolving from herringbone structures to face-to-face two-dimensional sheets. The results from temperature-dependent experiments on single crystals indicate the intermolecular couplings between molecules with longer alkoxy chains are quite different from the J-type aggregates seen in crystalline anthracene. By tuning the side chain length and modifying the crystal structures of 2,6-dialkoxyanthracenes, we can change the luminescence properties of the Frenkel excitons that exist in the crystals.

9-tert-butylanthracene (TBA) can undergo a reversible photoisomerization to the Dewar isomer. The dependence of both the formation and reversion of the Dewar isomer on pressure was investigated using absorption and fluorescence spectroscopy with TBA doped polystyrene as a model system. It is demonstrated that both the photoisomerization and its reverse reaction rates decrease with higher pressure.

Table of Contents

List of Figures

List of Tables

Chapter 1 Introduction

Organic materials have played an important role in the development of the semiconductor industry. Organic semiconductors combine low-cost fabrication and processing with novel optoelectronic properties that can be modified via the chemical structure to fulfill desired features, thus leading them to be attractive candidates as solar cell materials[1], as well as for other applications such as organic transistors[2] and light-emitting diodes[3-4].

Anthracene is well studied as the prototypical organic semiconductor, both as an isolated molecule and in its crystalline form[5-6]. My research focuses on two topics related to anthracene-based molecules: first, to clarify whether chemical modification could vary the crystal packing and further tune the exciton structures of the anthracene aggregates; second, to investigate the pressure effects on the reversible photoisomerization of 9-tert-butylanthracene (TBA) to see if this single-molecule reaction could be applied in pressure sensors.

1.1 Photophysics of 2,6-Dialkoxyanthracenes

Solar energy conversion has been increasingly drawing interest due to the aggravation of the energy crisis. However, the high cost of traditional inorganic solar cells limits commercial marketability[7]. Compared to their inorganic counterparts, organic photovoltaic cells are behind in aspects of performance or efficiency[8]. However, the advantage they hold in low-cost processing and mechanical flexibility keeps them competitive. Therefore, for the sake of achieving an ideal efficiency that surpasses 10% for marketability, detailed studies should be conducted on organic semiconductors.

In order to enhance the efficiency of organic photovoltaic, the four primary steps involved in their overall mechanism can be optimized: exciton creation, exciton diffusion, charge separation and charge transport to the external electrode. My research concentrates on optimizing the exciton diffusion using designed anthracene molecules. Both their steady-state and time-resolved spectroscopy are studied to help us understand the exciton diffusion process.

Excitations in organic molecular aggregates are called Frenkel excitons or excitonic polarons, which consists of a vibronically excited molecule surrounded by vibrationally excited molecules. The excitation is analogous to a bowling ball on a mattress. The ball together with the spring directly underneath is homologous to the vibronically excited molecule, with springs in the near compressing field corresponding to the adjacent vibrationally excited molecules. The transfer of the actual Frenkel exciton is analogous to the bowling ball rolling on the mattress while the delocalized coherence, corresponding to the adjacent vibrationally excited moleces, is analogous to the distance the ball travels, as shown in **Figure 1-1**. The resulting Franck-Condon (FC) progression responsible for the molecule's spectral shape is distorted by the exciton-vibrational coupling. New optical responses due to this distortion play a key role in determining the overall absorption and fluorescence spectral line shapes. Spectroscopically-extracted data are able to provide useful information such as the excitation bandwidth, the coherence number and the system's state of disorder.

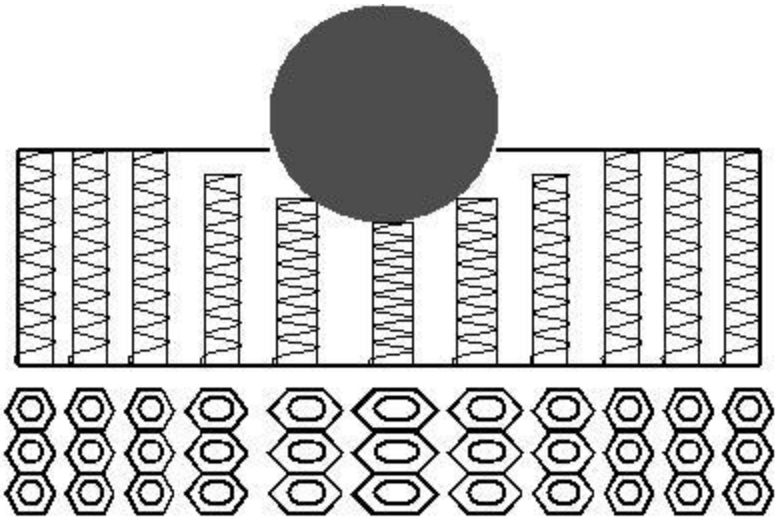

Figure 1-1 Analogy of the motion of a Frenkel exciton in a linear aggregate with a bowling ball on a mattress.

The spectroscopy of polyacenes solids can be accounted for obtaining quantitative information about the states that underlie their interesting electronic properties. Of particular interest is the relative geometrical arrangements of the neighboring molecules. Simplifying, we can take the geometrical arrangements of neighboring transition dipoles to two extremes to discuss the properties associated with the two ideal types of intermolecular couplings[9]: the J-aggregate and H-aggregate. In theory, the transition dipoles in the J-aggregates are oriented head-to-tail while those in the H-aggregates are oriented parallel with each other as shown in Figure 1-2. Within J-aggregates, excitons tend to condense into low energy excitation states in which the resulting transition dipole moments are maximized, thus leading to superradiant emission at low temperatures along the extended dipoles which has been theorized to be beneficial toward exciton diffusion[10]. In contrast, higher energy excitation states are favored in H-aggregates (see the solid arrow transition between the G and E’’ states in Figure 1-2b).

Spectroscopically, the absorption of the J-aggregates will be red-shifted with respect to that in the monomer while that of H-aggregates will be blue-shifted[11-12]

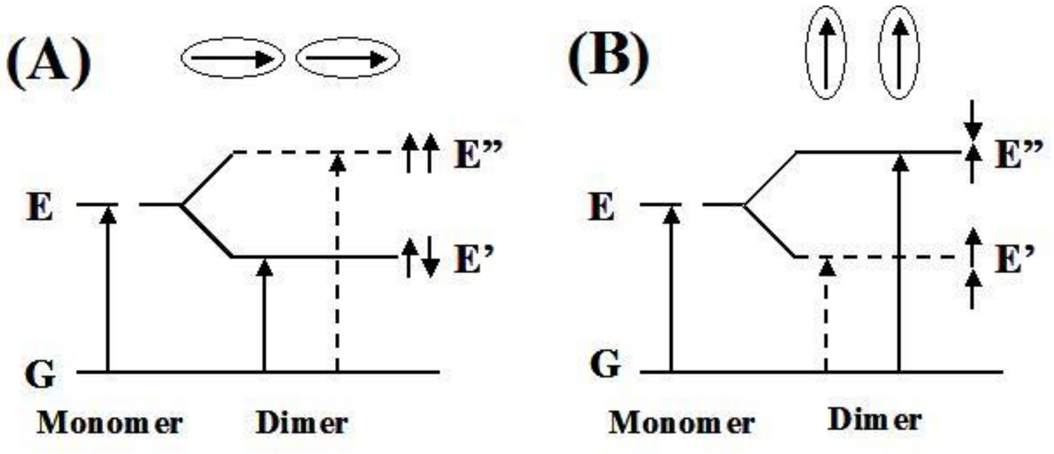

Figure 1-2 Exciton band structure in dimers with various geometrical arrangements of transition dipoles: (A) J aggregate (B) H aggregate, Only in-phase arrangements of dipoles give allowed exciton states (G=ground, E=excited)

Anthracene is perhaps the most widely studied organic semiconductor, yet the precise nature of its electronic states in the solid state remains an open question[13]. Anthracene-based materials have been generally chosen as a model to study organic semiconductor materials for several important reasons. First, anthracene has been reported to obtain very long singlet and triplet exciton diffusion lengths, ranging from 100 nm to several microns[5]. Secondly, the intermolecular coupling in anthracene single crystals creates delocalized electronic states which serves to accelerate exciton diffusion [14] as shown in Figure 1-3. Last but not least, anthracene-based molecules are subject to chemical modification[15-16]. Chemical substitution may tune their spectroscopic properties [17] as well as other physical or chemical properties, such as its solubility[18].

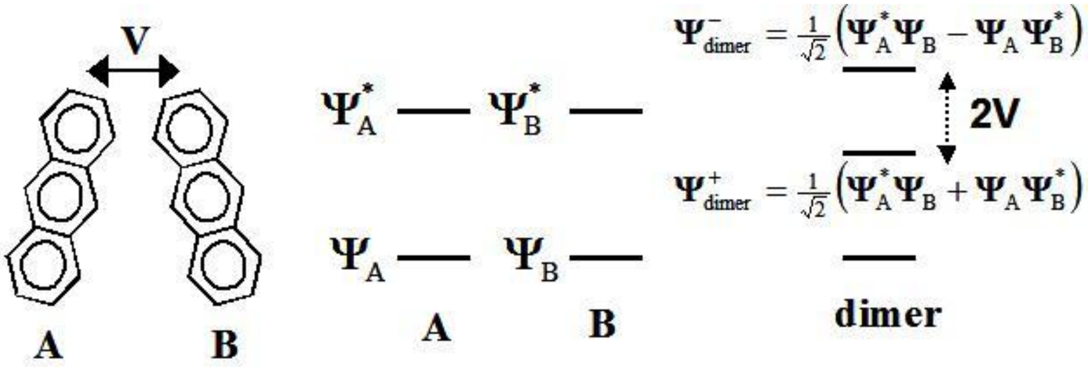

Figure 1-3 Intermolecular coupling between two anthracene molecules leading to delocalized states

Our group has previously studied time-resolved luminescence of anthracene polycrystalline thin films in an effort to clarify the nature of the low-lying Frenkel exciton states that determine its optical properties[19]. In conjunction with a detailed theoretical analysis, we came to the conclusion that the luminescence originates from a delocalized one-dimensional intermolecular exciton that is likely associated with a slip-dislocation defect. The 1D intermolecular exciton is a J-type aggregate with herringbone packing. The 0-0 peak of the intrinsic luminescence emission is responsible for the exciton coherence volume. The intensity ratio of the 0-0 peak to 0-1 peak is a simple measurement of the coherence length as long as self-absorption, index changes, etc. are corrected for. As the temperature is lowered and intramolecular couplings become weraker, the coherence length of the J-type aggregates increase, thus changing the fluorescence spectral shape dramatically.

Solid anthracene is known to support a variety of structural defects due to the weak interactions that control its crystal packing. The first question following our previous work is whether structural defects can be minimized within single anthracene crystals so that its luminescence will come solely from the intrinsic 2D exciton within the anthracene solid aggregates. Anthracene polycrystalline films and single crystals with comparable thickness can be grown and studied to address this concern as long as both samples are thin enough to avoid self-absorption.

To further investigate the role of the crystal packing in determining the exciton structure, we were inspired to create a system that would enable us to tune the exciton structure within anthracene aggregates. It has been reported that the molecular organization of thiophene oligomers can be significantly increased at the mesoscopic level by affixing side carbon substituents to the chromophore [20]. Given the promising results of this study, we became interested in the synthesis of anthracene derivatives that could mimic the herringbone-packing motif as shown in

Figure 1-4**.** In this approach, chemical substitution can enable us to simultaneously tune the molecular packing and control the intermolecular interactions that dominate exciton formation and dynamics. The ability to “engineer” exciton states by modifying the chromophore packing geometry could lead to new solid-state materials with interesting optical properties.

In order to follow through with this idea, we needed a system in which varying the chemical substituent does not change the optical properties of the core chromophore.

Our goal was therefore to identify a strategy for anthracene where we could systematically change chemical substituents and vary the crystal packing while leaving the optical properties of the isolated molecule unchanged. There exists a large body of work on chemically modified anthracenes and their crystal structures. [21-22] The 9,10 substituted anthracene family is the most widely studied, but the presence of chemical groups extending from the side of the anthracene moiety tends to encourage face-to-face packing in the crystal rather than the desired herringbone packing. We decided to look at a family of 2,6-substituted anthracenes, with the hope that by adding substituents to the ends of the anthracene, rather than the side, the herringbone packing motif could be maintained.

A series of 2,6-dialkoxyanthracenes were synthesized and their photophysical properties in liquid solution and solid state studied. Both spectral lineshapes and luminescence decay kinetics of these molecules in dilute solution and within a polymer matrix are identical. However, we found that varying the length of alkyl tails on the ends of the anthracene causes these molecules to adopt different packing arrangements in solid aggregates, which in turn should give rise to different excitonic behavior.

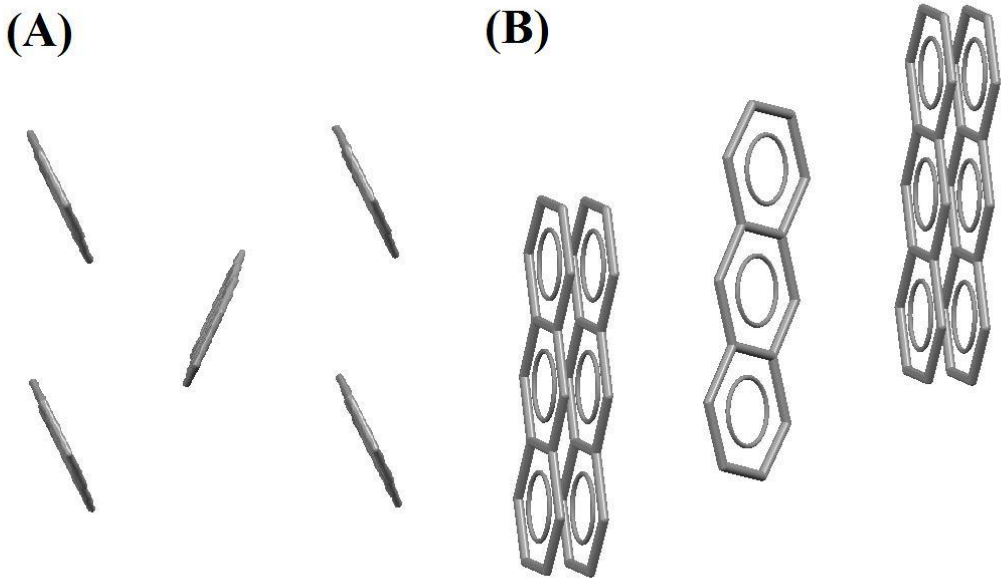

Figure 1-4 Herringbone-packing of anthracene molecules: (A) top view and (B) side view

1.2 Mechanochemistry of 9-tert-Butylanthracene (TBA)

Conventional tools to stimulate a chemical reaction include heat, electricity and light. During the past decade, the mechanical force, discovered as a new tool, has been utilized to convert one molecule to another. Theoretical studies have already proved that mechanical force can dramatically change the potential energy surface for a reaction[23-24]. The molecules that can undergo transformation under mechanical force are known as mechanophores. These mechanophores can be covalently tethered with long polymer chains[25] to develop new pressure-sensitive materials that signal by changing color or emitting light[26-27].

There are several ways to apply mechanical force to a molecule. A simple method entails ball-milling experiments that physically grind chemicals together[28-29].

Single-molecule spectroscopy offers an alternate approach[30-32] that is highly selective yet runs into difficulty when using traditional analytical methods to characterize the products. Ultrasound is another technique used to exert mechanical force onto polymers[25, 33] but it is accompanied with undesirable thermal effects[34]. In my project, a direct way for applying pressure without thermal effects was used[35] and is detailed in Chapter 5.

In this past, anthracene derivatives have been demonstrated to show reversible photomechanical properties[36-38]. The [4+4] photodimerization and the reverse reaction of anthracene, pictured in **Figure 1-5,** has potential applications for photochromic devices[39] as well as for energy and information storage[40-41]. Certain bis-anthracene photoisomers can undergo pressure-activated, covalent bond breaking, making them potential candidates as pressure sensors[42] (see **Figure 1-6**). The pressure-sensitive bond breaking depends on the reverse reaction of the anthracene [4+4] photoisomerization. In my project, we focused on the reversible photoisomerization reaction of 9-terbutylanthracene (TBA) shown in **Figure 1-7**. The fluorescence intensity of TBA was tracked to investigate the reaction rates. It was hypothesized that the reverse reaction was pressure-activated. As such, the reverse reaction rate should be enhanced when pressure is directly applied to the TBA doped polymer films. However, our results showed an opposite trend. More work needs to be done in this area to confirm our preliminary results and determine the exact pressure dependence of the reaction rates.

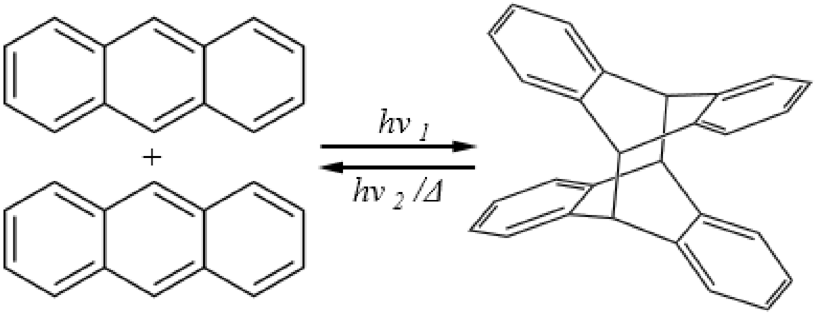

Figure 1-5 [4+4] photodimerization reaction of anthracene

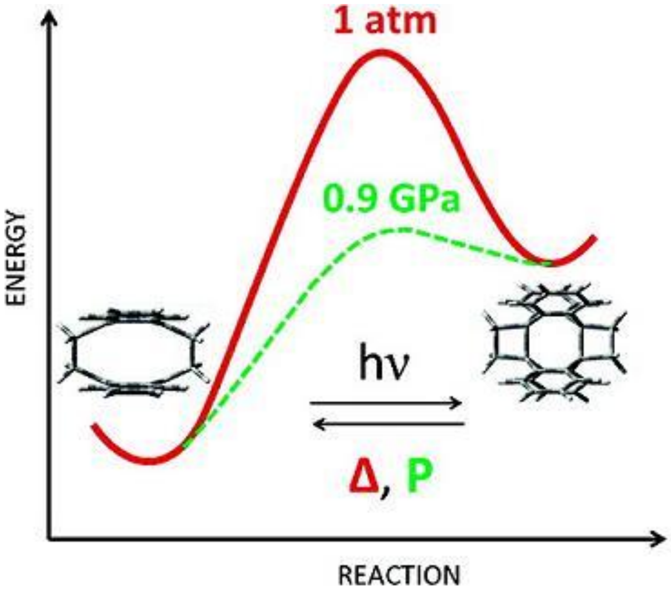

Figure 1-6 pressure-activated, covalent bond breaking for the photoisomer of bis-anthracene (Copyright © 2012 American Chemical Society)

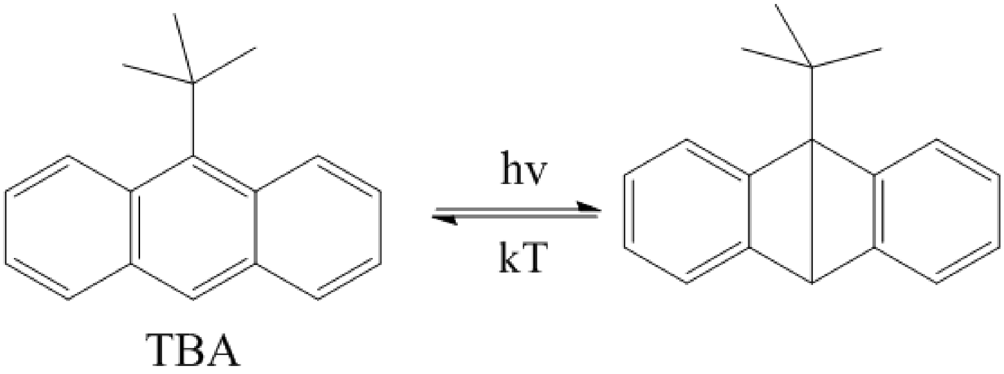

Figure 1-7 Photoisomerization of 9-tert-butylanthracene (TBA)

To summarize, there are two main areas of focus for the research described in this thesis. The first area is the photophysical properties of the derived anthracene-based materials. The associated synthesis, experimental techniques and theoretical basis are described in Chapter 2. The temperature-dependent photophysics of isolated 2,6 diakoxyanthracene molecules is described in Chapter 3. Excited state side-chain conformational relaxation is discussed in this chapter as well. In Chapter 4, both the crystal structures and the solid-state spectroscopy of 2,6 diakoxyanthracene aggregates are described. The second area of focus is discussed in Chapter 5 and is concerned with the pressure effects on the photoisomerization of 9-tert-butylanthracene (TBA) and its reversion. A conclusion and future directions for research are outlined in Chapter 6.

References:

1. Hains, A.W., et al., *Molecular Semiconductors in Organic Photovoltaic Cells.* Chemical Reviews, 2010. **110**(11): p. 6689-6735.
2. Tsumura, A., H. Koezuka, and T. Ando, *Macromolecular electronic device: field-effect transistor with a polythiophene thin film.* Appl. Phys. Lett., 1986. **49**(Copyright (C) 2012 American Chemical Society (ACS). All Rights Reserved.): p. 1210-12.
3. Tang, C.W. and S.A. VanSlyke, *Organic electroluminescent diodes.* Appl. Phys. Lett., 1987. **51**(Copyright (C) 2012 American Chemical Society (ACS). All Rights Reserved.): p. 913-15.
4. Burroughes, J.H., et al., *Light-emitting diodes based on conjugated polymers.* Nature, 1990. **347**(6293): p. 539-541.
5. Silinsh, E.A.C., V. , ed. *Organic Molecular Crystals: Interaction, Localization, and Transport Phenomena*. 1994, AIP Press: New York.
6. Mueller, H.P., P. Thoma, and G. Vaubel, *The phosphorescence of anthracene single crystals and its spectrum.* Phys. Status Solidi, 1967. **23**(Copyright (C) 2012 American Chemical Society (ACS). All Rights Reserved.): p. 253-62.
7. Van Zant, P., *Microchip Fabrication: A Practical Guide to Semiconductor Processing*, ed. McGraw-Hill. 1990.
8. Dou, L., et al., *Tandem polymer solar cells featuring a spectrally matched low-bandgap polymer.* Nat Photon, 2012. **6**(3): p. 180-185.
9. Kasha, M., *Energy Transfer Mechanisms and the Molecular Exciton Model for Molecular Aggregates.* Radiation Research, 1963. **20**(1): p. 55-70.
10. Spano, F.C., *The spectral signatures of Frenkel polarons in H- and J-aggregates.* Acc. Chem. Res., 2010. **43**: p. 429-439.
11. Kasha, M., H.R. Rawls, and M.A. El-Bayoumi, *The exciton model in molecular spectroscopy.* Pure Appl. Chem., 1965. **11**: p. 371-392.
12. Levinson, G.S., W.T. Simpson, and W. Curtis, *Electronic Spectra of Pyridocyanine Dyes with Assignments of Transitions1.* Journal of the American Chemical Society, 1957. **79**(16): p. 4314-4320.
13. Silinsh, E.A., *Organic Molecular Crystals: Their Electronic States*. 1 ed. 1980, Heidelberg: Springer-Verlag.
14. Rose, T.S., R. Righini, and M.D. Fayer, *Picosecond transient grating measurements of singlet exciton transport in anthracene single crystals.* Chemical Physics Letters, 1984. **106**(1–2): p. 13-19.
15. Dutta, A.K. and T.N. Misra, *Fluorescence study of 9, 10 diphenyl anthracene in mixed Langmuir-Blodgett films with stearic acid.* Optical Materials, 1994. **3**(1): p. 35-40.
16. Mukai, I., et al., *Dimer Formation of Anthracene in Langmuir-Blodgett Films as Revealed by Time-Resolved Fluorescence Spectra.* Chemistry Letters, 1997. **26**(3): p. 263-264.

17. Durfee, W.S., et al., *Davydov splitting in 7-(2-anthryl)-1-heptanoic acid Langmuir-Blodgett films.* Journal of the American Chemical Society, 1987. **109**(5): p. 1297-1301.
18. Biesmans, G., et al., *On the fluorescence of anthracene chromophores in langmuir-blodgett films.* Thin Solid Films, 1989. **169**(1): p. 127-142.
19. T. S. Ahn, A.M.M., R. O. Al-Kaysi, F. C. Spano, J. E. Norton, D. Belijonne, J-L. Bredas, C. J. Bardeen, *Experimental and theoretical study of temperature dependent exciton delocalization and relaxation in anthracene thin films.* J. Chem. Phys. , 2008. **128**: p. 054505.
20. Garnier, F., et al., *Molecular engineering of organic semiconductors: design of self-assembly properties in conjugated thiophene oligomers.* Journal of the American Chemical Society, 1993. **115**(19): p. 8716-8721.
21. Cohen, M.D., Z. Ludmer, and V. Yakhot, *The fluorescence properties of crystalline anthracenes and their dependence on the crystal structures.* physica status solidi (b), 1975. **67**(1): p. 51-61.
22. Zouev, I., et al., *Photodimerization of anthracene derivatives in their neat solid state and in solid molecular compounds.* CrystEngComm, 2011. **13**(Copyright (C) 2012 American Chemical Society (ACS). All Rights Reserved.): p. 4376-4381.
23. Ong, M.T., et al., *First Principles Dynamics and Minimum Energy Pathways for Mechanochemical Ring Opening of Cyclobutene.* J. Am. Chem. Soc., 2009. **131**(Copyright (C) 2012 American Chemical Society (ACS). All Rights Reserved.): p. 6377-6379.
24. Ribas-Arino, J., M. Shiga, and D. Marx, *Understanding Covalent Mechanochemistry.* Angew. Chem., Int. Ed., 2009. **48**(Copyright (C) 2012 American Chemical Society (ACS). All Rights Reserved.): p. 4190-4193, S4190/1-S4190/10.
25. Hickenboth, C.R., et al., *Biasing reaction pathways with mechanical force.* Nature (London, U. K.), 2007. **446**(Copyright (C) 2012 American Chemical Society (ACS). All Rights Reserved.): p. 423-427.
26. Davis, D.A., et al., *Force-induced activation of covalent bonds in mechanoresponsive polymeric materials.* Nature (London, U. K.), 2009. **459**(Copyright (C) 2012 American Chemical Society (ACS). All Rights Reserved.): p. 68-72.
27. Chen, Y., et al., *Mechanically induced chemiluminescence from polymers incorporating a 1,2-dioxetane unit in the main chain.* Nat. Chem., 2012. **4**(Copyright (C) 2012 American Chemical Society (ACS). All Rights Reserved.): p. 559-562.
28. Zhang, G., et al., *Polymorphism and Reversible Mechanochromic Luminescence for Solid-State Difluoroboron Avobenzone.* J. Am. Chem. Soc., 2010. **132**(Copyright (C) 2012 American Chemical Society (ACS). All Rights Reserved.): p. 2160-2162.
29. Sheth, A.R., et al., *Mechanochromism of piroxicam accompanied by intermolecular proton transfer probed by spectroscopic methods and solid-phase*

changes. J. Am. Chem. Soc., 2005. **127**(Copyright (C) 2012 American Chemical Society (ACS). All Rights Reserved.): p. 6641-6651.

30. Liang, J. and J.M. Fernandez, *Kinetic Measurements on Single-Molecule Disulfide Bond Cleavage.* J. Am. Chem. Soc., 2011. **133**(Copyright (C) 2012 American Chemical Society (ACS). All Rights Reserved.): p. 3528-3534.
31. Ainavarapu, S.R.K., et al., *Single-Molecule Force Spectroscopy Measurements of Bond Elongation during a Bimolecular Reaction.* J. Am. Chem. Soc., 2008. **130**(Copyright (C) 2012 American Chemical Society (ACS). All Rights Reserved.): p. 6479-6487.
32. Szoszkiewicz, R., et al., *Dwell time analysis of a single-molecule mechanochemical reaction.* Langmuir, 2008. **24**(Copyright (C) 2012 U.S. National Library of Medicine.): p. 1356-64.
33. Jakobs, R.T.M. and R.P. Sijbesma, *Mechanical Activation of a Latent Olefin Metathesis Catalyst and Persistence of its Active Species in ROMP.* Organometallics, 2012. **31**(Copyright (C) 2012 American Chemical Society (ACS). All Rights Reserved.): p. 2476-2481.
34. Groote, R., R.T.M. Jakobs, and R.P. Sijbesma, *Performance of Mechanochemically Activated Catalysts Is Enhanced by Suppression of the Thermal Effects of Ultrasound.* ACS Macro Lett., 2012. **1**(Copyright (C) 2012 American Chemical Society (ACS). All Rights Reserved.): p. 1012-1015.
35. Adams, D.M., S.J. Payne, and K. Martin, *Fluorescence of diamond and Raman spectroscopy at high pressures using a new design of diamond anvil cell.* Appl. Spectrosc., 1973. **27**(Copyright (C) 2012 American Chemical Society (ACS). All Rights Reserved.): p. 377-81.
36. Zhu, L., R.O. Al-Kaysi, and C.J. Bardeen, *Reversible Photoinduced Twisting of Molecular Crystal Microribbons.* Journal of the American Chemical Society, 2011. **133**(32): p. 12569-12575.
37. Zhu, L., et al., *Crystal Structures and Photophysical Properties of 9-Anthracene Carboxylic Acid Derivatives for Photomechanical Applications.* Crystal Growth & Design, 2011. **11**(11): p. 4975-4983.
38. Al-Kaysi, R.O., A.M. Müller, and C.J. Bardeen, *Photochemically Driven Shape Changes of Crystalline Organic Nanorods.* Journal of the American Chemical Society, 2006. **128**(50): p. 15938-15939.
39. Duerr, H. and H. Bouas-Laurent, *Photochromism: Molecules and Systems: Revised Edition*. 2003: Elsevier Science B.V. 1044 pp.
40. Irie, M., *Diarylethenes for Memories and Switches.* Chemical Reviews, 2000. **100**(5): p. 1685-1716.
41. Jones Ii, G., T.E. Reinhardt, and W.R. Bergmark, *Photon energy storage in organic materials— The case of linked anthracenes.* Solar Energy, 1978. **20**(3): p. 241-248.
42. Jezowski, S.R., et al., *Pressure Catalyzed Bond Dissociation in an Anthracene Cyclophane Photodimer.* Journal of the American Chemical Society, 2012. **134**(17): p. 7459-7466.

Chapter 2 Experimental Methods

2.1 Introduction

The experimental and sample preparation techniques used to study the photophysics of anthracene-based molecules, are described in this chapter. In order to prepare anthracene-based samples, three 2,6-dialkoxyanthracene molecules are synthesized, which is presented in section 2. Several methods to fabricate the anthracene solid-state samples are discussed in section 3. The substrates of the solid-state samples need to be treated before usage, and the techniques are described in section 4. The surface morphology of the solid-state samples is characterized using two analytical instruments, which is presented in section 5. Section 6 described the techniques for taking spectra, which includes the usage of a steady-state spectrometer, a steady-state fluorometer, and a time-resolved-based Ti-Sapphire laser set-up. The computational methods are presented in section 7. In addition, the calculation methods for the fluorescence lifetime and the oscillator strength are described in section 8.

2.2 Synthesis of 2,6-Dialkoxyanthracenes

Three 2,6-dialkoxyanthracene molecules were synthesized: 2,6-dimethoxy-anthracene (**C1**), 2,6-dipropoxy-anthracene (**C3**), and 2,6-dihexyloxy-anthracene (**C6**). The synthetic scheme is shown in **Figure 2-1**. The synthesis of **C1-C6** followed closely the procedure used by Brotin et al. [1] All starting materials were purchased from Sigma-Aldrich and used as received. The alkylation was achieved by adding the alkyl iodide dropwise to a mixture of potassium carbonate and 2,6-dihydroxyanthraquinone (~2 mmol, 0.48g, purity 90%) in 100 ml *N*,*N*-Dimethylmethanamide (DMF) with stirring. [2] The typical molar ratio between anthraquinone, potassium carbonate and alkyl iodide was 1:5:4.5. The reacting mixture was stirred continually for 24 hours at room temperature and then poured into ice water and extracted with CH_2Cl_2. $MgSO_4$ was added to remove the residue water from organic phase and then filtered out. After rotary evaporation, the resulting 2,6-dialkoxyl-anthraquinones turned to be flake-like solids with a bright yellow color. The synthesis started from **C6** and the compound structure was verified by ^1H NMR with the yield of ~80%.. The purity of 99% was confirmed by LC-MS tests. Then **C1**/**C3**-quinone was prepared in the same way.

C6-quinones- ^1H NMR: (400MHz, $CDCl_3$; δ), 8.22(d, J=8.6Hz, H_9&H_{10}), 7.70(d, J=2.8Hz, H_4&H_8), 7.22(dd, J=2.7Hz&11.3Hz, H_3&H_7), 4.15(t, J=6.6Hz, 4H,OCH_2), 1.85(m,4H,CH_2), 1.54(m,4H,CH_2), 1.50(m,8H,CH_2CH_2), 0.92(t, 6H,CH_3)

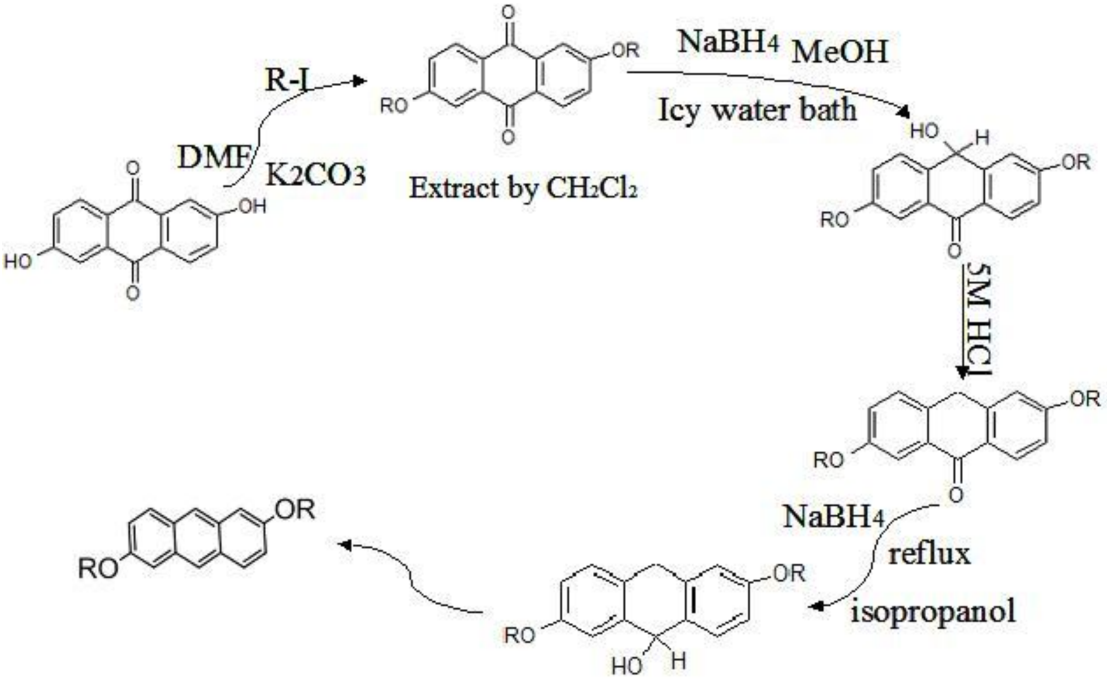

Figure 2-1 2,6-dialkoxyanthracene synthetic scheme

Two methods were used to reduce the 2,6-dialkoxyl-anthraquinones to the 2,6-dialkoxyl-anthracenes: zinc/acetic acid reduction and sodium borohydride reduction. According to one previous report[3], both quinone groups could be reduced simultaneously using a zinc/acetic acid procedure. The 2,6-dihexyloxy-anthraquinones were reduced following this method: the 2,6-dihexyloxy-anthraquinones (~1mmol) were mixed with glacial acetic acid (30ml) under stirring. 1.7g Zn dust (26mmol) was added to the suspension which was then refluxed for 24hours. The product was extracted, washed and dried closely following the previous work. The product obtained was verified by LC-MS tests (see **Figure 2.2**) to consist mainly of a cross-coupled dialkoxy-substituted bianthryl compound[4], rather than the desired product.

After the zinc/acetic acid reduction failed, Criswell's procedure[5] was applied to convert 2,6-dialkoxyl-anthraquinones to 2,6-dialkoxyl-anthracenes in two steps. ~1 mmol of the dialkoxy-anthraquinone was dissolved in 20 ml of methanol. Sodium borohydride ($NaBH_4$) was added to the suspension while stirring in an ice-water bath. The molar ratio between anthraquinone and $NaBH_4$ was 1:5. After 4-hours, the reaction mixture was poured into ice water and the solid was obtained by vacuum filtration and dried in air. This solid was added to 12 ml 5 N HCl and heated to ~90°C to drive off any remaining water. After ~6 hours of heating, the suspension turned from white to orange-yellow. The solid was isolated by vacuum filtration, washed multiple times with water, and dried in air. The resulting anthrone was placed in ~20 ml isopropanol, followed by the addition of $NaBH_4$ in a molar ratio of at least 5:1, and refluxed for 24 hours or longer. The resulting suspension was poured into ice water. 1 N HCl was added to neutralize the system and precipitate the final product. The solid was isolated by vacuum filtration, washed multiple times with water, and dried in air. Finally, the yellow solid was purified using silica gel chromatography with a mixture of dichoromethane/hexane (1:3) and recrystallized from chloroform to yield pale yellow crystals. The proton NMR and melting point were obtained for the three compounds.

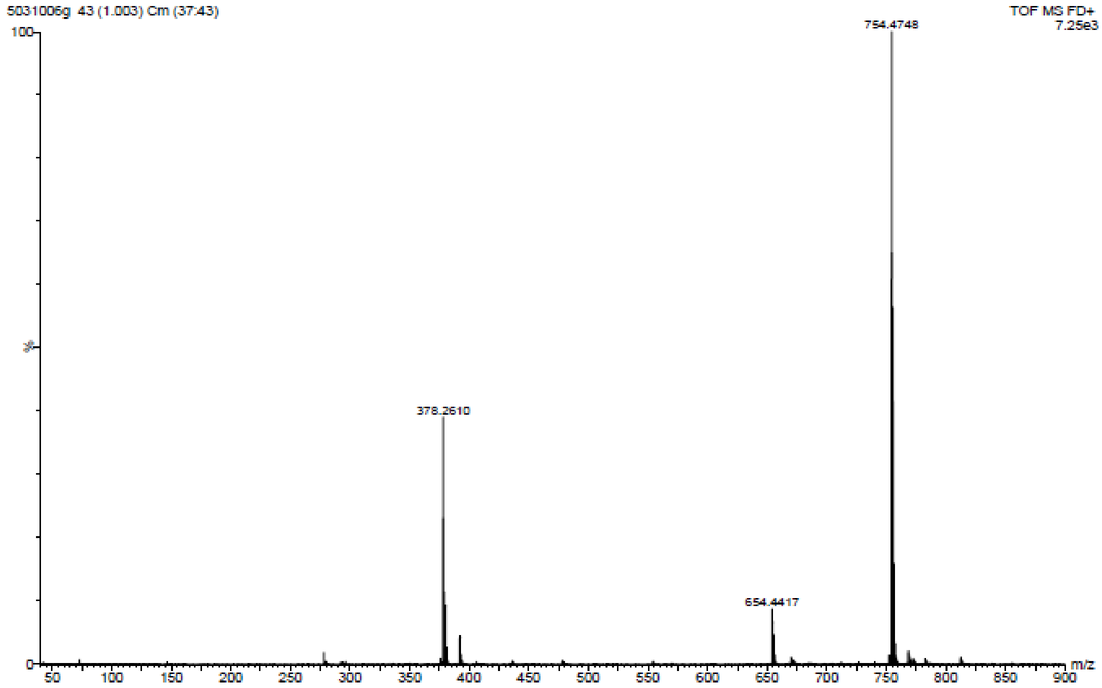

Figure 2.2 LC-MS of Zn-acid reduction product from C6-quinones

C1- ^{1}H NMR: (400MHz,$CDCl_3$; δ), 8.21(s, H_9&H_{10}), 7.85(d, J=9.0Hz, H_4&H_8), 7.19(d, J=2.5Hz, H_1&H_5), 7.13(dd, J=2.5&8.7Hz, H_3&H_7), 3.97(s,6H,OCH_3) mp 259-261°C

C3- ^{1}H NMR: (400MHz,$CDCl_3$; δ), 8.18(s, H_9&H_{10}), 7.84(d, J=9.1Hz, H_4&H_8), 7.17(s, H_1&H_5), 7.14(d, J=2.4Hz, H_3&H_7), 4.08(t, J=6.6Hz, 4H,OCH_2), 1.91(m,4H,CH_2), 1.11(t, J=7.4Hz, 6H,CH_3) mp 234-236°C

C6- ^{1}H NMR: (400MHz,$CDCl_3$; δ), 8.18(s, H_9&H_{10}), 7.84(d, J=9.0Hz, H_4&H_8), 7.17(s, J=2.2Hz, H_1&H_5), 7.14(d, J=2.4Hz, H_3&H_7), 4.11(t, J=6.6Hz, 4H,OCH_2), 1.88(m,4H,CH_2), 1.54(m,4H,CH_2), 1.40(m,8H,CH_2CH_2), 0.94(t, 6H,CH_3) mp 162-164°C

2.3 Solid-state Samples

2.3.1 Alkoxy-Anthracene Single crystals

Crystals of **C1-C6** were grown from chloroform solution for x-ray determination of single crystal structures and solid-state spectroscopy studies. The **C1-C6** single crystals were grown via a solvent diffusion method: the target compound was dissolved in chloroform to make a saturated solution. The small glass vial with the saturated solution was put into a larger glass container that contained pure methanol. The large vial was sealed while the smaller one inside was open to let solvents diffuse. Typically, growth of single crystals was completed within 5 days (see **Figure 2-3**). Single crystals with good quality were picked out under the microscope via a birefringence test. Anthracence and 2,6-dialkoxyanthracene have anisotropic crystal structures and they are optically birefringent. The birefringence properties can be used for picking out single crystals with good quality. The potential single crystals were put on the pre-cleaned glass substrate on the sample stage of a microscope. Two thin-film polarizers which were arranged in the same polarization direction were used: One was attached on the objective while the other was put on under the sample at 90° to the first polarizer. If the anthracene crystal is indeed a single crystal, its brightness will change integrally as it is rotated between the polarizers.

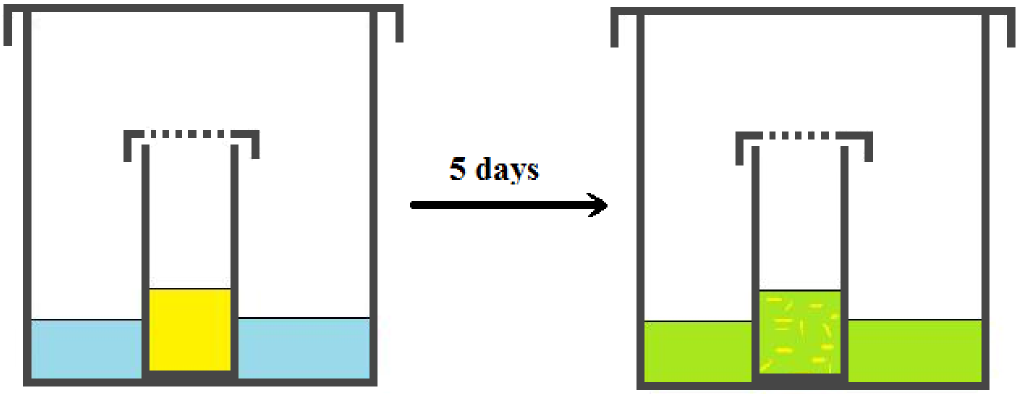

Figure 2.3 The procedure of solvent-diffusion method. Blue:methanol; Cn-chloroform solution / Cn crystals(yellow); methanol-chloroform mixture (green)

2.3.2 Anthracene Single Crystals Grown By Sublimation

Weigh about 10 mg finely ground zone-refined anthracene that was purchased from TCI and used as received. Put it into the sublimer (seen in **Figure 2.4**) and heat it to ~120°C with cooling water under active house-vacuum to remove the oxygen. Close the vacuum valve and continue heating until 150°C. Let the crystal grow for 24 hours. Pick crystals up with a clean needle, spray a pre-cleaned glass substrate with ethanol, and mount the crystal on the substrate. Single crystals with good quality were picked out using the same birefringence test described earlier.

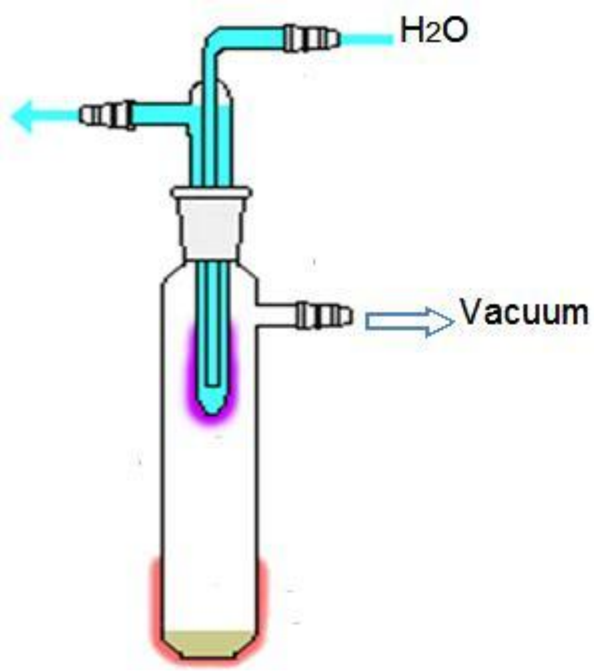

Figure 2.4 Sublimation method for crystal growth

2.3.3 Anthracene crystals grown from solution

In order to make ultrathin anthracene single crystals, a floating-drop method was applied, described in **Figure 2-5**. Xylenes were used to minimize the crystal thickness due to their low surface tension and ideal liquid density. Anthracene was dissolved in xylenes to make a solution of 10^{-3} M. According to previous research [3], anthracene single crystals with hundreds of nanometers in thickness can be obtained with this concentration. A Petri dish was filled with Milli-Q water and 1 ml anthracene solution was added dropwise onto the water surface. The petri dish was covered with a big glass cover with an Al foil to keep the system in darkness. The xylenes evaporate within 48 hours, leaving the anthracene crystals floating on the water's surface. The crystals were later picked out with a clean needle and carefully put on a pre-cleaned glass substrate.

Single crystals were chosen via the same birefringence test described earlier.

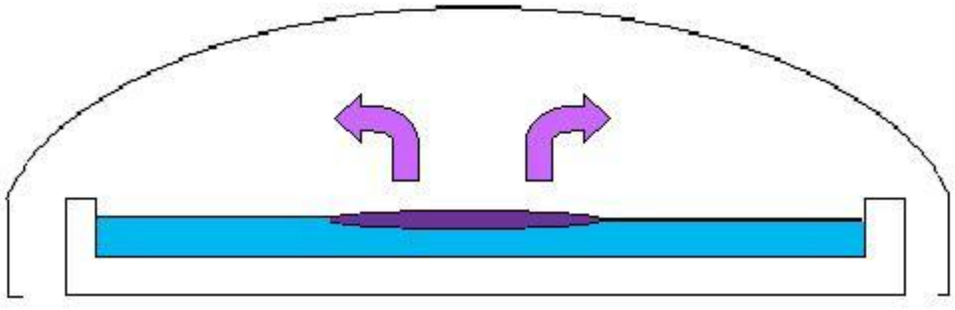

Figure 2.5 Floating-drop (FD) Method for single crystal growth: DI water (blue); anthracene in xylenes (purple)

2.3.3 Polycrystalline Thin Films Grown by Sublimation

The anthracene thin films were originally prepared with a vacuum evaporator (Ted Pella Inc., PAC-1) under a vacuum of 3×10^{-5} Torr as described in previous work [2]. The ultrathin films (abs~0.1) were obtained to avoid self-absorption. However, the evaporator was contaminated with tetracene and impossible to clean thoroughly. The steady-state absorption and fluorescence spectra of a contaminated anthracene film is shown in **Figure 2-6**. As a result, the homemade evaporator was used instead.

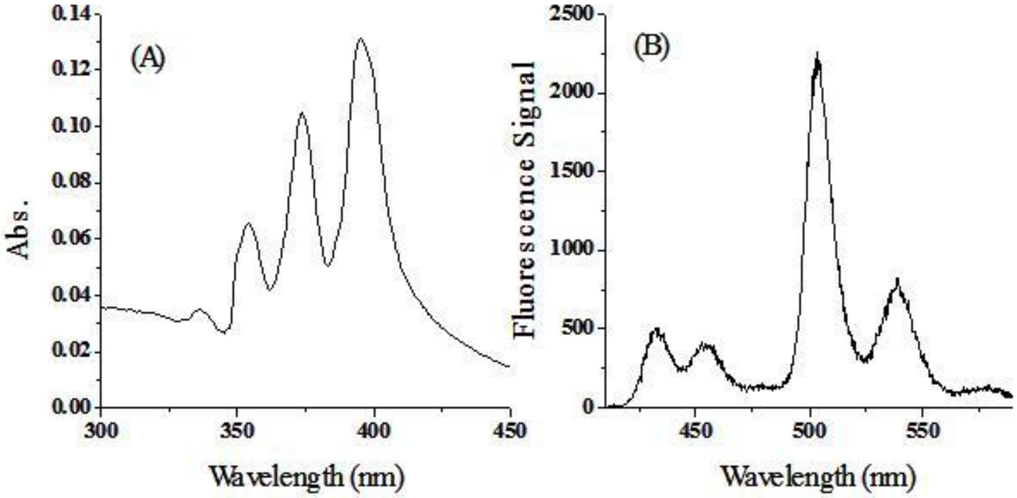

Figure 2.6 Steady-state absorption (A) and fluorescence (B) spectra of a tetracene-contaminated anthracene film

All the thin films used for my experiments were prepared in the same home-made evaporator. The thin films of anthracene and 2,6 dialkoxyanthracene thin films were deposited onto a pre-cleaned glass substrate by evaporating ~1 mg powder samples from the bottom of the home-made evaporator under a vacuum of 3.0~3.5x10^{-5} Torr (see **Figure 2-7**).

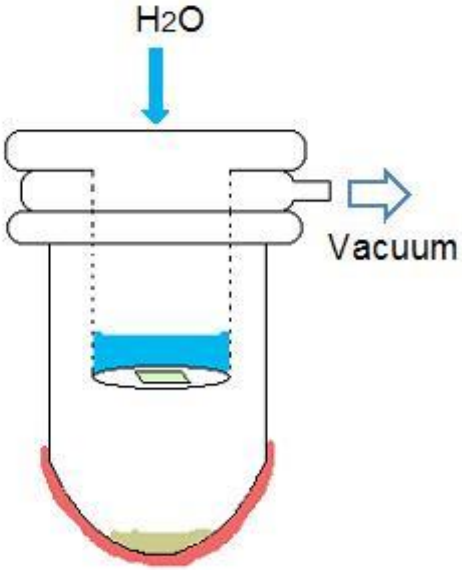

Figure 2.7 the home-made evaporator for film deposition

2.4 Substrate Surface Treatments

2.4.1 Pre-Cleaning

The microslides and cover glasses used as the substrates for single crystals and films were cleaned via the following steps. All glasses were submerged into a petri dish with Nano-strip for 1 hour, then in JTB-111 FEOL cleaner (from J.T. Baker) for another hour, and finally sonicated in DI water for 1hour to clean thoroughly. Nano-strip contains a stabilized formulation of sulfuric acid and hydrogen peroxide. The result is a strong acidic solution that removes positive and negative resists as well as other organic materials needed for general substrate cleaning. The JTB-111 FEOL cleaner is a basic solution containing alkylammonium hydroxide to neutralize the Nano-strip. This process makes the glass surface more hydrophilic in addition to thoroughly cleaning it.

2.4.2 Silanization

The purpose of silanization is to make the glass surface more adhesive for the organic samples. In this procedure, a covalent -Si-O- bond replaces the hydroxyl groups on the glass surface. The silanization solution is prepared by mixing 2 g octadecyltrichlorosilane (90+%, Aldrich) in 40 ml dichloromethane. The glass substrate is submerged into the solution and then sonicated for 5 min. The substrate surface is wiped with a Kimwipe to remove any white residue. The reaction governing this procedure is detailed in **Scheme 2-1**.

Scheme 2-1

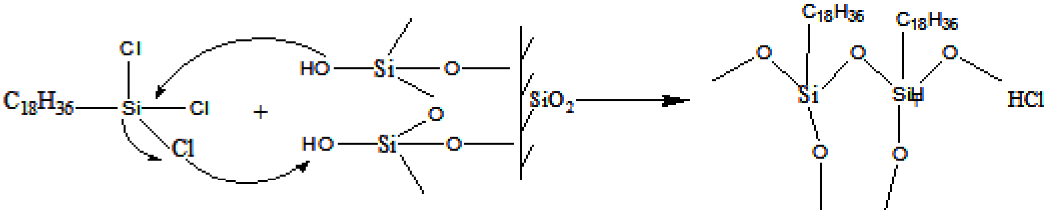

2.5 Morphology Characterization

2.5.1 Film Thickness Measured with Dek-Tak

A Veeco DekTak-8 surface profilometer was used to measure the thickness of the anthracene single crystals. The measurements were performed in the clean room at UCR's Center for Nanoscale Science and Engineering under the guidance of Dong Yan. The anthracene single crystal was measured directly on the cover glass substrate. The thinnest anthracene single crystal was prepared via floating-drop method with a thickness of ~400 nm, Figure 2.8.

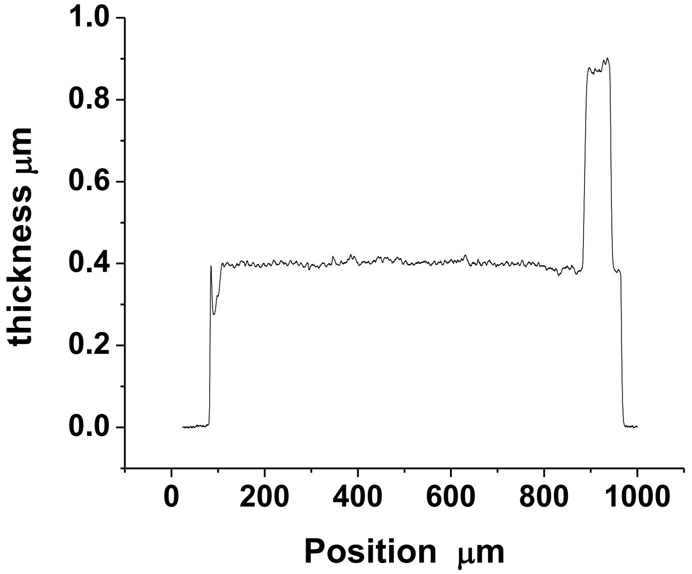

Figure 2.8 Thickness confirmed by DekTak-8:The thinnest single crystal grown via FD method

2.5.2 Film Morphology Measured Using AFM

To explore the topology of anthrance polycrystalline films, a Novascan ESPM ^{II} atomic force microscopy (AFM) was used. The AFM was calibrated in the x,y, and z directions before measurement. A tapping contact mode scan was performed with a scan rate of 1Hz, a resolution of 400 x 400, and scan size of 30 x 30 um. **Figure 2.9** displays the measurement executed on an evaporated anthracene film. The film was found to be uneven as previously reported [3], with many anthracene "islands" spread out on the glass substrate.

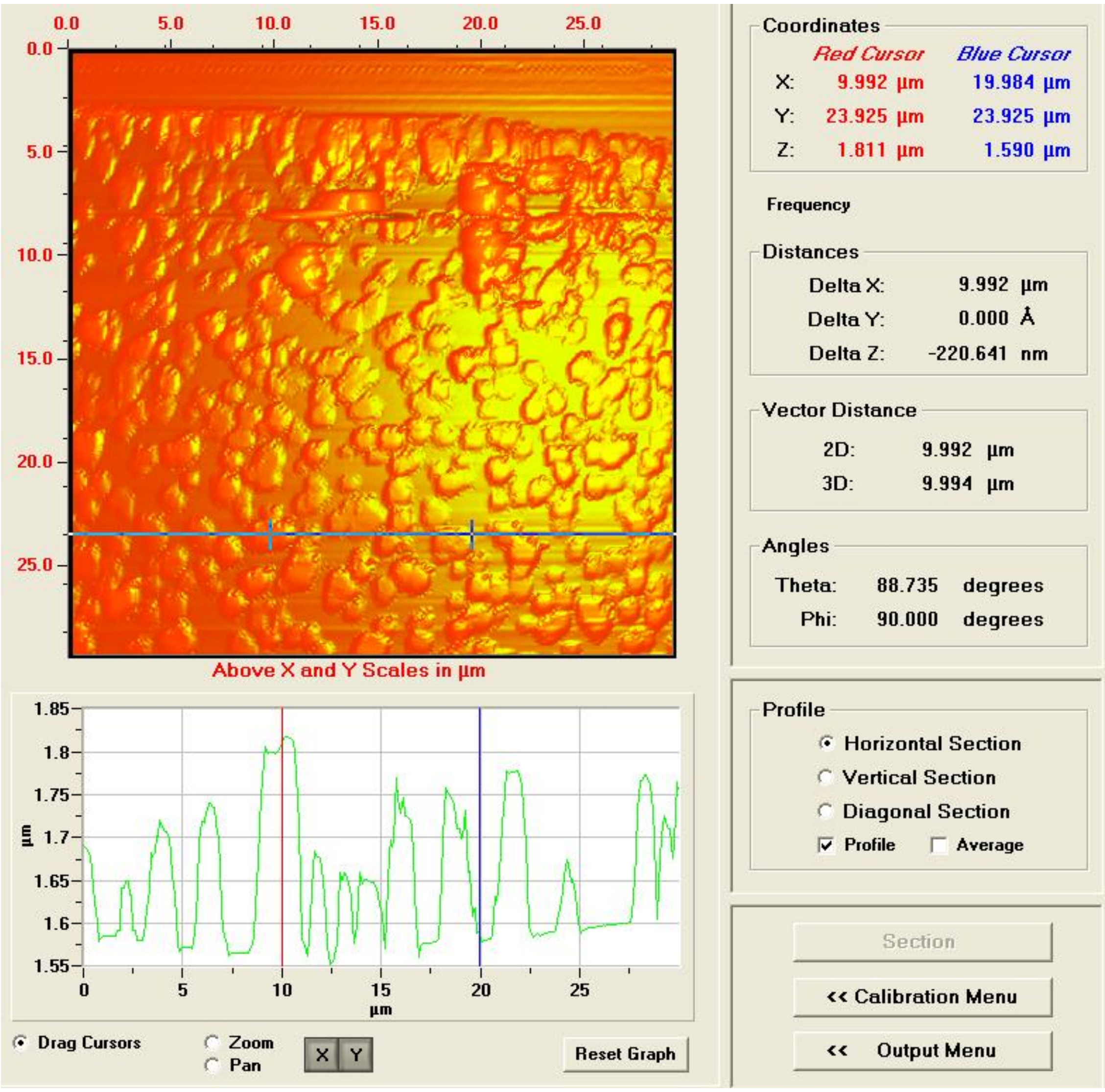

Coordinates

	Red Cursor	Blue Cursor
X:	9.992 µm	19.984 µm
Y:	23.925 µm	23.925 µm
Z:	1.811 µm	1.590 µm

Distances

Delta X:	9.992 µm
Delta Y:	0.000 Å
Delta Z:	-220.641 nm

Vector Distance

2D:	9.992 µm
3D:	9.994 µm

Angles

Theta:	88.735 degrees
Phi:	90.000 degrees

Profile

- ● Horizontal Section
- ○ Vertical Section
- ○ Diagonal Section
- ☑ Profile ☐ Average

Figure 2.9 Anthracene film surface topology tested by AFM

2.6 Spectroscopy

2.6.1 Steady-state Spectroscopy

Steady-state UV-visible absorption and fluorescence emission were measured with a Cary 50 Bio UV-Visible spectrometer and a Spex Fluorolog Tau-3 fluorescence spectrophotometer (excitation at 365nm). Fluorescence quantum yields (ϕ_{fl}) were determined using 9,10-diphenylanthracene in cyclohexane as a standard [6]. Since most of our measurements were performed in solutions that were not degassed, the obtained quantum yield for the reference was recalculated by scaling the literature value of 0.90 by the ratio of the fluorescence lifetime of diphenylanthracene in untreated cyclohexane (6.0 ns) to that in degassed cyclohexane (7.7 ns) (see **Figure 2.10**) to obtain a value of 0.70 for the fluorescence quantum yield in the non-degassed cyclohexane. This was used in reference for calculating the quantum yields of **C1-C6** in regular cyclohexane solution.

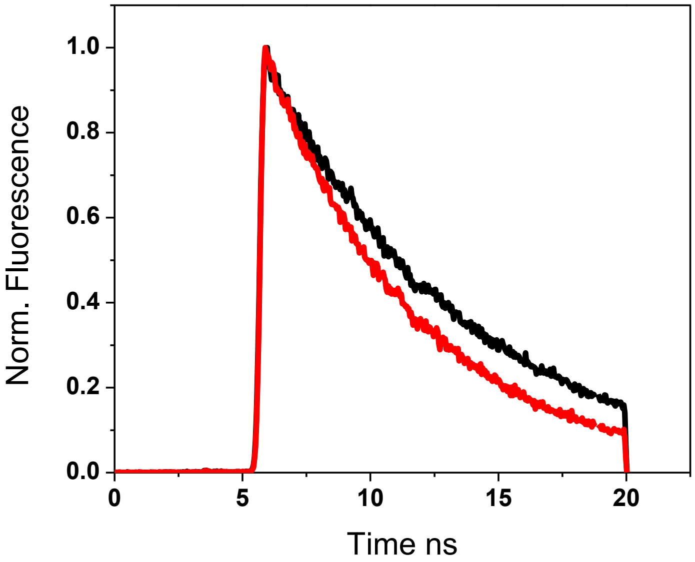

Figure 2.10 fluorescence decays of DPA in degassed(black) and non-degassed(red) cyclohexane solutions

2.6.2 Time-Resolved Spectroscopy

Fluorescence lifetime measurements were performed by exciting the samples using pulses centered at 266 nm derived from a 40 kHz regeneratively amplified Ti:sapphire laser system. The 800 nm pulses were first frequency doubled to produce 400 nm light, which was then mixed noncollinearly with the residual 800 nm light in a second BBO crystal to generate the 266 nm pulses. The 266 nm light was isolated using a spatial filter and a 266 nm interference filter. Front-face excitation and detection were used for all samples, with the excitation pulse incident on the sample at about 10° relative to the sample surface normal. To avoid time-dependent effects due to molecular reorientaion, a thin film polarizer was used to adjust the angle between the polarization of the collected fluorescence and that of the incident light to 54.7° (the magic angle). The fluorescence was directed into a monochromator attached to a picosecond streak camera (Hamamatsu C4334 Streakscope), which provides both time- and wavelength-resolved fluorescence data with a resolution of 15 ps and 2.5 nm. The solution samples were placed in a 1 cm path length quartz cuvette, while the solid samples were located inside a Janis ST-100 continuous flow liquid N_2 cryostat with an active vacuum of 10^{-4}-10^{-5} Torr. Scattered 266 nm light was absorbed by a clean microscope slide in front of the streak camera entrance slit.

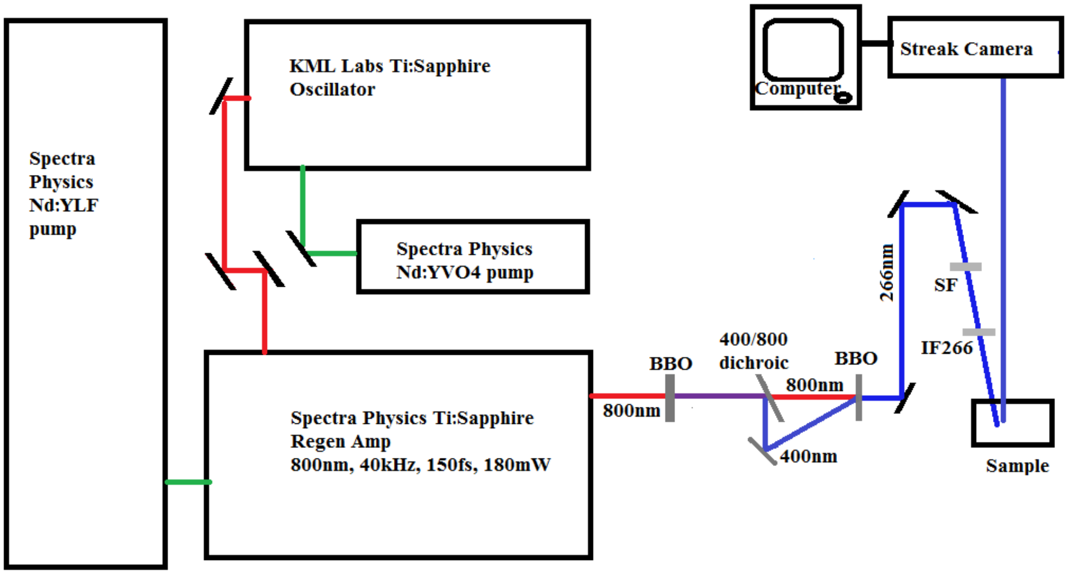

Figure 2.11 Laser set-up for time-resolved fluorescence measurement (excitation wavelength:266nm)

2.7 Computational Methods

All calculations were done with the Gaussian 09 quantum chemistry package [7]. The calculation method used for this work was TD-B3LYP using the SVP double zeta basis set[8-9]. Geometries converged with a force threshold of 0.00045 au and a displacement threshold of 0.001800 au. Ground state geometries were obtained using B3LYP/SVP with no symmetry restrictions and these geometries were subsequently used for calculating the vertical excitations of the two molecules. The energies of the S_1 state of each molecule were also obtained using the relaxed S_1 geometry. Minima were confirmed by ensuring the Hessian contained no imaginary values.

2.8 Calculation Methods

2.8.1 Calculation of Fluorescence Lifetime Using Strickler-Berg Method

The fluorescence lifetime of organic molecules in solution can be calculated using the absorption spectra via the Strickler-Berg method[10]. Following **Equation 2-2**, n is the refractive index of the medium, ε is the molar extinction coefficient, $\tilde{\nu}$ is the frequency of the transition in cm^{-1}, g_l and g_u are the degeneracies of the lower and upper states, and $<\tilde{\nu}_f^{-3}>_{Av}^{-1}$ can be further described by **Equation 2-3**. I(ν) is the absorption intensity and ν is the corresponding wavenumber in cm^{-1}.

$$1/\tau_0=2.880*10^{-9}\, n^2<\tilde{\nu}_f^{-3}>_{Av}^{-1}\frac{g_l}{g_u}\int \varepsilon d\ln\tilde{\nu} \qquad \textbf{Equation 2-2}$$

$$<\nu_f^{-3}>_{Av}^{-1}=\frac{\int I(\nu)d\nu}{\int \nu^{-3}I(\nu)d\nu} \qquad \textbf{Equation 2-3}$$

2.8.2 Calculation of Oscillator Strength

The oscillator strength of organic molecules in solution can be obtained from absorption spectra[11] using **Equation 2-4**, where m_e and e are the mass and charge of the electron, respectively, c is the vacuum velocity of light, ε is the molar absorption coefficient at wavenumber $\tilde{\nu}$, and N_A is the Avogadro's number.

$$f=(2303m_ec^2/N_A\pi e^2)\int\varepsilon d\tilde{\nu} \qquad \textbf{Equation 2-4}$$

References

1. Brotin, T., et al., *Photostationary fluorescence emission and time resolved spectroscopy of symmetrically disubstituted anthracenes on the meso and side rings: the unusual behavior of the 1,4 derivative.* Photochem. Photobio., 1992. **55**: p. 349-358.
2. Pozzo, J.L., et al., *Different synthetic routes towards efficient organogelators: 2,3-substituted anthracenes.* Tetrahedron, 1997. **53**: p. 6377-6390.
3. Lu, L., et al., *A new convenient synthesis of alkoxyanthracenes from alkoxy-9,10-anthraquinones.* Synthesis, 2003: p. 2464-2466.
4. Kyziot, J.B. and J. Zaleski, *9,9'-bianthracenyl.* Acta Cryst. E, 2007. **63**: p. 1235-1237.
5. Criswell, T.R. and B.H. Klanderman, *Studies related to the conversion of 9,10-anthraquinones to anthracenes.* J. Org. Chem., 1974. **39**: p. 770-774.
6. Hamai, S. and F. Hirayama, *Actinometric determinationof absolute fluorescence quantum yields.* J. Phys. Chem., 1983. **87**: p. 83-89.
7. Frisch, M.J., et al., *Gaussian 09, B.01.* 2009, Gaussian Inc.: Wallingford, CT.
8. Becke, A.D., *Density-functional thermochemistry. 3. The role of exact exchange.* J. Chem. Phys., 1993. **98**: p. 5648-5652.
9. Schaefer, A., H. Horn, and R. Ahlrichs, *Fully optimized contracted Gaussian basis sets for atoms Li to Kr.* J. Chem. Phys., 1992. **97**: p. 2571-2577.
10. Strickler, S.J. and R.A. Berg, *Relation between absorption intensity and fluorescence lifetime of molecules.* J. Chem. Phys., 1962. **37**(Copyright (C) 2012 American Chemical Society (ACS). All Rights Reserved.): p. 814-22.
11. Applequist, J., *Theory of solvent effects on the visible absorption spectrum of β-carotene by a lattice-filled cavity model.* J. Phys. Chem., 1991. **95**(Copyright (C) 2012 American Chemical Society (ACS). All Rights Reserved.): p. 3539-45.

Chapter 3 Spectroscopic Properties of Alkoxy-anthracenes in Solution

3.1 Introduction

The photophysical properties of unsubstituted anthracene molecules in different organic solvents have been widely studied[1-2]. In the current project, the initial step was to characterize the photophysics of 2,6 dialkoxyanthracene molecules in dilute solution in order to see how the presence of the alkoxy groups affects the properties of the anthracene core. Brotin et al. previously studied the steady-state properties of alkoxy-substituted anthracenes[3-4], and the current chapter extends that work with the goal of contrasting their electronic structure and dynamics to those of anthracene. Comparison of the electronic structure (energies and transition dipole moments) and the excited state dynamics to those of unsubstituted anthracene (**An**) reveals that the optical properties of the anthracene core are significantly altered by the presence of the alkoxy groups. In particular, in both liquid solution and in a solid matrix, the luminescence can originate from two different conformers whose interconversion rate depends on temperature, solvent, and the length of the alkyl chain. The complex excited state behavior of this class of anthracene derivatives will need to be taken into account in future experiments where temperature-dependent luminescence decays and spectral lineshapes are used to analyze exciton structure in solid-state samples. This paper illustrates the potential of our synthetic approach to engineer crystals with varying packing motifs, but also illustrates the complications that can arise from chemical modifications of the core chromophore.

3.2 Results and Discussion

Molecules **C1**, **C3** and **C6** were synthesized following an earlier procedure where the hydroxyl groups of 2,6 dihydroxy anthraquinone were first coupled to alkyl iodides in a standard S_N2 reaction. This reaction was followed by a two-step reduction of the quinone groups using $NaBH_4$. The molecular structures of the three derivatives are shown in **Figure 3-1**.

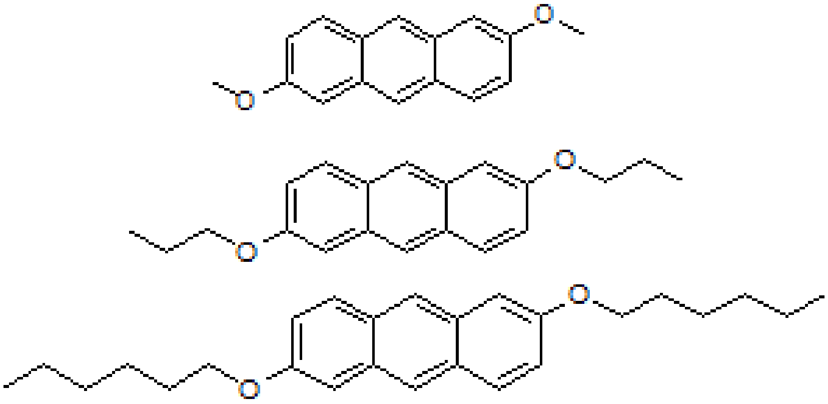

C1

C3

C6

Figure 3-1 molecular structures of C1, C3and C6

The next question concerns how the addition of the alkoxy groups affects the electronic properties of the central anthracene unit. Ideally, the electronic structure of the anthracene core would remain unaffected by the alkoxy substituents, but comparison of the steady-state absorption and fluorescence data of **An** and **C1-C6** in **Figure 3-2** shows that this is not the case. All our data for **C1-C6** are very similar to those obtained by Briton et al. for 2,6-didecyloxyanthracene, showing two distinct vibronic progressions in the absorption spectrum as opposed to the single one seen in **An**. Rather than a single progression starting at 375 nm for **An**, there are now two well-defined electronic transitions with origins at 403 nm and 339 nm, respectively. The peak absorption coefficients for both transitions are 4000-5000 $M^{-1}cm^{-1}$, about half the value for **An**. These low and high energy absorption features have been analyzed previously by Michl and coworkers [4-5]using linear dichroism experiments and have been assigned to the L_a and L_b states, respectively. These workers also hypothesized that addition of the alkoxy groups promoted mixing of the L_a and L_b states rather than the creation of new states. A comparison of the oscillator strengths of the two lowest transitions in **C1**-**C6** with that of **An**, given in **Table 3-1**, provides support for this idea. The total oscillator strength[58] integrated from 290-450 nm for all four molecules are within 20% of each other, as would be expected for systems where mixing of states serves to redistribute rather than create oscillator strength.

Table 3-1 Experimental results for energies of the first and second vertical excitations S1, S2 with their peak extinction coefficient ε and integrated oscillator strength f for anthracene and its derivatives

Molecule	Anthracene	**C1**	**C3**	**C6**
S_1 Transition Energy / cm^{-1}	26596	24876	24814	24752
Peak ε of S_1 Transition / $M^{-1} \cdot cm^{-1}$	8597	4200	4365	4591
S_2 Transition Energy / cm^{-1}	----	29499	29499	29499
Peak ε of S_2 Transition / $M^{-1} \cdot cm^{-1}$	----	3201	3778	3521
Integrated Oscillator Strength f /×	9.0	8.7	11.4	10.6

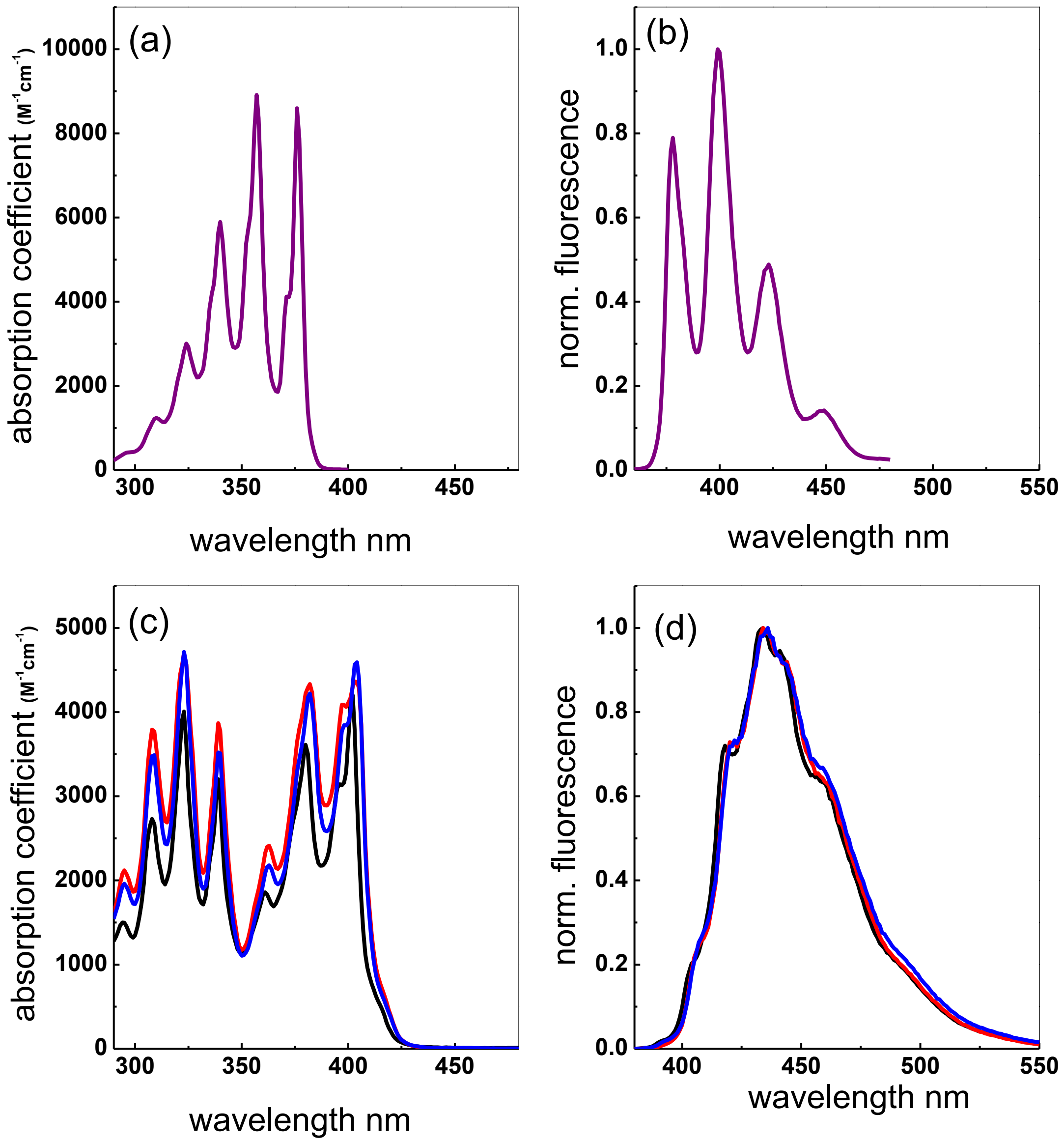

Figure 3-2 Steady-state absorption, b) normalized fluorescence emission spectra of anthracene in non-degassed ethanol (purple) and c) Steady-state absorption, d) normalized fluorescence emission spectra of C1(black) / C3(red) / C6(blue) in non-degassed cyclohexane

We can gain more insight into the nature of these two states by comparing excited state electronic structure calculations on **An** and **C1**. Using time-dependent density functional theory (TDDFT) we find that both molecules possess two low-lying excited states corresponding to the well-known L_a and L_b states in the linear polyacenes. In **An**, the transition dipole moments (TDM's) corresponding to these two states are orthogonal and the lower energy L_a state has a dipole moment strength (proportional to the square of the TDM and linearly proportional to the experimental oscillator strength) that is 43x larger than that of the L_b state. Thus in **An**, the higher energy L_b state is effectively dark and the UV-Vis spectroscopy can be understood in terms of a single bright electronic state, the L_a state whose TDM is oriented along the short axis of the molecule. For **C1**, the calculation predicts that the TDM's of the L_a and L_b states are no longer orthogonal and that the L_a dipole moment strength is now only ~8x larger than that of the L_b transition. The broken symmetry induced by the alkoxy groups can be seen in the transition density maps for **An** and **C1** in **Figures 3-3c and 3d.** The main effect of this biasing of the electron density is the rotation of both the L_a and L_b TDM's in the anthracene plane, with the L_a transition rotated ~30° relative to the molecular short axis. When going from **An** to **C1**, the calculation predicts a decrease in the $S_0 \rightarrow S_1$ energy of ~3000 cm^{-1}, as given in **Table 3-2**, which can be compared to the experimentally observed shift of ~2000 cm^{-1}. In addition, the experimental spectra in **Figure 3-2** suggest that the L_a and L_b transitions are close to equal in strength, whereas the calculation still has the L_a dipole moment strength almost a factor of 8 larger than that of the L_b state. It has been shown that B3LYP may have inherent problems describing the excited states of polyacenes.[4] Grimme and coworkers found that the B2-PLYP double-hybrid functional[5] gave better results for the excited state energies in this class of molecules. We repeated the calculations using this method and found that the energies of the states all shifted higher by about 3000 cm^{-1}, and the energy difference between the **An** and **C1** $S_0 \rightarrow S_1$ transition decreased slightly to ~2500 cm^{-1}, closer to the experimental value. But the ratio of dipole moment strengths for the L_a and L_b states in **C1** increased slightly from 7.6 to 10.4. Thus this method afforded slightly better agreement with the experimental energies, but still fell short of predicting the change in absorption intensities. In either case, theory does show the same qualitative trends as experiment, predicting both the increase in the L_b transition strength and the experimentally observed shift of the L_a state to lower energy.

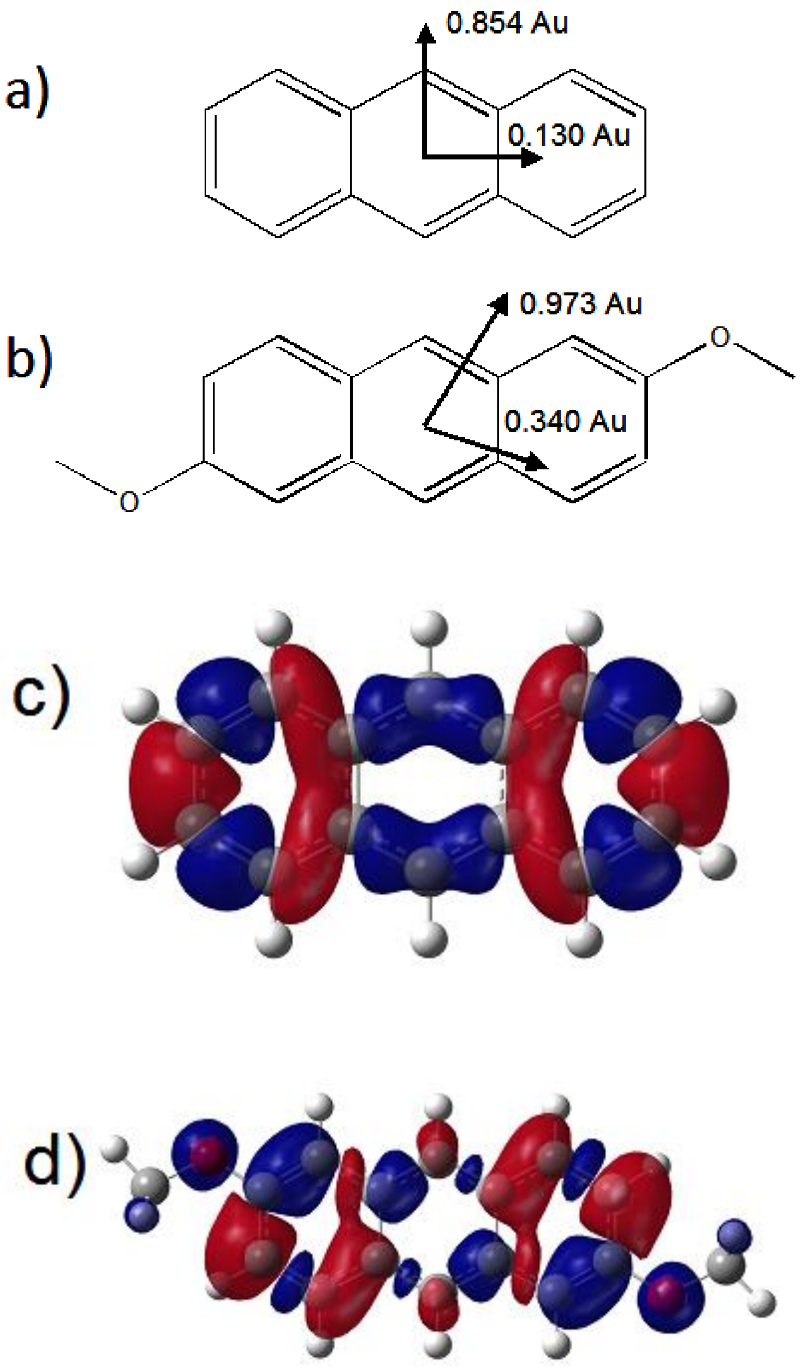

Figure 3-3 The transition electric dipole moment vectors of the S0->S1*(->) and S0->S2*(->>) transitions in a) anthracene and b) 2,6-dimethoxyanthracene. Also shown are the visualization of the difference of the densities of the excited state and the ground state

Table 3-2 Calculated energies of the first and second vertical excitations S1, S2 and for anthracene and its derivative

Molecule	anthracene	C1
S_1Transition Energy / cm^{-1}	26110	23102
S_2 Transition Energy / cm^{-1}	31182	30387
Transition Dipole Moment $\mu^2(S_0\text{-}S_1)$ / Au	0.854	0.973
Transition Dipole Moment $\mu^2(S_0\text{-}S_2)$ / Au	0.130	0.340

While the energies and oscillator strengths of the excited states of the 2,6-dialkoxyanthracenes are significantly changed relative to those of **An**, their absorption lineshapes retain the well-resolved vibronic features and relative peak heights seen in the **An** absorption spectrum, with a Huang-Rhys factor on the order of 1 for the C-C double bond stretching modes located at 1200-1400 cm^{-1} typically observed in the polyacenes. [5,7] This similarity in lineshapes does not extend to the fluorescence, however. The fluorescence dynamics of the dialkoxy anthracenes are very different from those of unsubstituted **An**, whose fluorescence decay is a single exponential with a constant spectrum that is close to a mirror image of the absorption. The fluorescence spectra of **C1**-**C6** are identical: they lack the well-defined vibronic peak progression seen in **An**'s fluorescence, and the fluorescence quantum yields in **Table 3-2(b)** are also significantly larger than those of **An**. The origin of these differences in the steady-state spectra becomes clear once time-resolved fluorescence measurements are performed. During the fluorescence decay, the spectrum shifts to lower energy and changes shape, indicating that there is an excited state relaxation process involving different emitting states. The change in fluorescence lineshape is shown in **Figure 3-4(a)** for early (0-1 ns) and late (4-5 ns) times for **C3** in cyclohexane. The shoulder on the high energy side disappears while the red emission located from 470-500 nm becomes more pronounced. This can also be seen in the wavelength-resolved fluorescence traces shown in **Figure 3-4(b)**. The emission in the 405-415 nm range undergoes a biexponential decay, where the short-lived component τ_1=0.8 ns is exactly mirrored by an increase in signal in the range 470-480 nm that occurs with the same time constant. After the first 3 ns, in all solvents the spectrum is stable and undergoes a monoexponential decay with a ~15 ns time constant. The fact that an initial rapid decay in the blue is mirrored by a rise in the red suggests that we are seeing a population transfer to a lower energy state. Biexponential fits using the time constants in **Table 3-3(b)** did a good job of reproducing the data, as expected for a two-state process. The rate of the initial relaxation process depends both on the molecular structure and on the solvent. As shown in **Table 3-3**, the fast relaxation time, τ_1, increases as the length of the alkyl tail increases, from 0.8 ns for **C1** to 1.3 ns for **C6**. τ_1 also depends on solvent – the relaxation is slightly more rapid in cyclohexane (0.7-1.0 ns) than in CH_2Cl_2 (0.8-1.3 ns).

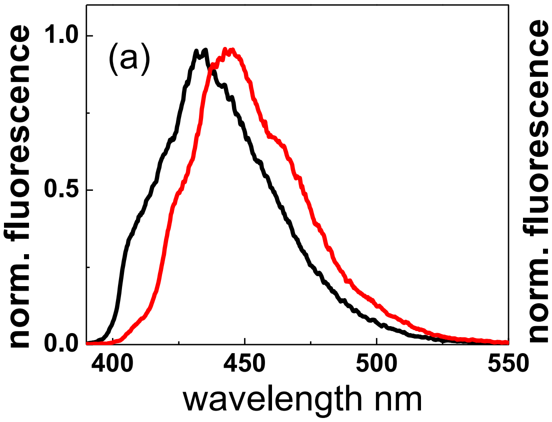

Figure 3-4a) Time-resolved fluorescence emission spectra (black: integrated from 0-1ns; red: integrated from 4-5ns) and b) wavelength-resolved fluorescence decays (black: integrated from 405-415nm; red: integrated from 470-480nm) of 2,6-dipropanyloxy anthracene (C3) in cyclohexane. Also shown are the biexponential fits to the time traces using the time constants in Table 3-3(b)

Table 3-3 (a) Room-temperature fluorescence lifetime of short-lived component τ_1* / long-lived component τ_2* in non-degassed methylene chloride. Also (b) Fluorescence lifetime of short-lived component τ_1 / long-lived component τ_2 and quantum yields Φf in non-dega degassed cyclohexane at room temperature.(c) Temperature-dependent fluorescence lifetime of short-lived component τ of C3 in zeonex matrix

(a)

Molecule	C1	C3	C6
τ_1^* / ns	0.77±0.07	0.92±0.08	1.30±0.07
τ_2^* / ns	15.5	15.7	16.6

(b)

Molecule	C1	C3	C6
τ1 / ns	0.69±0.03	0.76±0.03	1.04±0.04
τ2 / ns	11.2±0.2	11.7±0.03	11.8±0.3
Φ_f	0.43	0.42	0.42
τ τ_{rad} / ns	26	27	27
S_1 Transition / cm^{-1}	24630/ 23041(max)	24570/ 23041(max)	24570/22936(max)
S_1*Transition / cm^{-1}	24876	24814	24752
SB method τ0 /ns	9.4	7.3	7.8

(c)

Temperature /K	325K	298K	265K	235K	205K
τ / ns	1.4±0.3	1.8±0.2	3.0±0.3	5.5±0.2	7.8±0.3

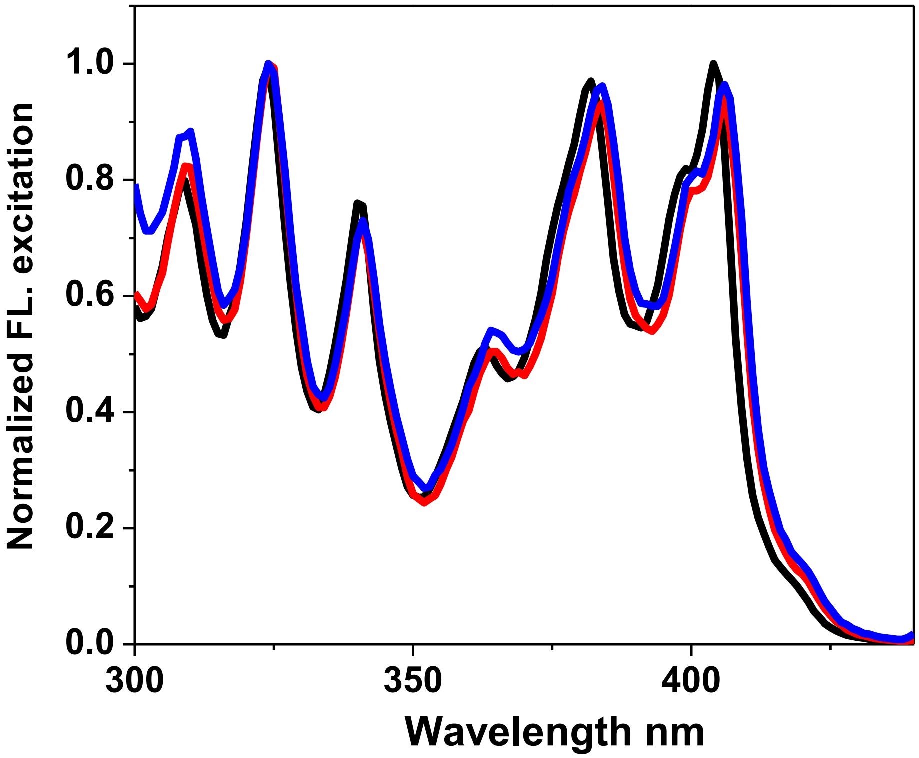

Figure 3-5 Normalized fluorescence excitation of C1(black) / C3(red) / C6(black) in Zeonex at room temperature

The existence of two distinct emitting species in **C1-C6** was confirmed by variable temperature measurements. **C3** was dissolved into an inert polymer, Zeonex, where at room temperature the excitation and fluorescence spectra are identical to those in cyclohexane, except for a 2 nm redshift (see **Figure 3-5)**. As the temperature is lowered from 298 K to 77 K, the steady-state fluorescence spectrum undergoes a dramatic change in shape, as shown in **Figure 3-6**. The blue edge grows rapidly as the temperature decreases, until the fluorescence spectrum recovers the general shape and vibronic structure of the absorption spectrum, as seen in **An**. Similar phenomena were also discovered in the temperature-dependent fluorescence spectra of **C1** and **C6** in the Zeonex matrix, as shown in **Figure 3-8**. The change in the steady-state emission is accompanied by changes in the fluorescence decay dynamics. **Table 3-3(c)** summarizes the biexponential fit parameters for the normalized fluorescence decays in both the blue (405-415 nm) and red (460-470 nm) spectral regions for **C3** in Zeonex extracted from data curves similar to those shown in **Figure 3-6**. The long-time component τ_2 remains roughly constant at all temperatures, 22-23 ns, which is close to the calculated radiative lifetime given in **Table 3-3(b)**. The short-time component τ_1 increases systematically as the temperature decreases until it cannot be reliably distinguished from the long-time decay in a biexponential fit. If we take $k_1=1/\tau_1$ to be the rate of going from the initial excited state conformation to the lower energy conformation, we can make an Arrhenius plot of $\ln(k_1)$ versus inverse temperature. This plot is shown in **Figure 3-6** for the temperature range 325 K to 200 K. The data yield a straight line, and a linear least-squares fit to the data results in an activation energy $E_{act}=8\pm 1$ (670 ± 80 cm^{-1}). The physical picture that emerges from the data is given in **Figure 3-9**, where the initial excitation event carries the ground state to an anthracene-like excited state, with a small Stokes shift and a "normal" vibronic progression where the 0-0/0-1 vibronic peak ratio is close to that of the absorption spectrum. But in the 2,6 dialkoxyanthracenes, there exists a second emissive state *B* that is reached via an activated process with a barrier of ~8 kJ/mol. At higher temperatures, this low energy conformer dominates the emission, while at low temperatures the molecule becomes trapped in conformer *A*, leading to a more anthracene-like emission spectrum.

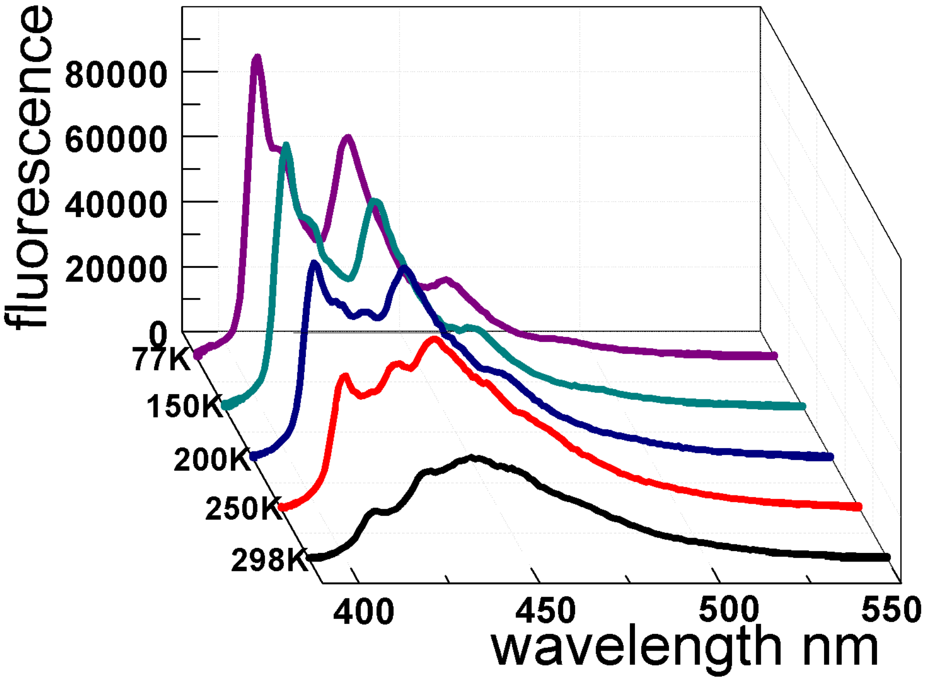

Figure 3-6 Steady-state fluorescence spectra of 2,6-dipropanyloxy anthracene (C3) in Zeonex at different temperatures

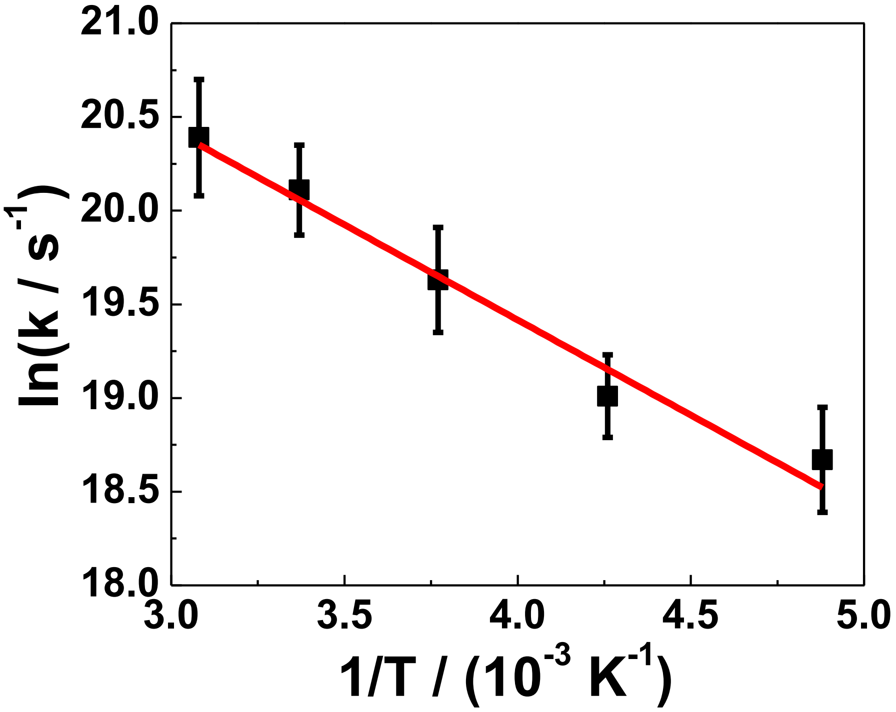

Figure 3-7 Temperature dependence of transfer rate k_1 between S_1^A and S_1^B states for C3 in a Zeonex matrix. A linear fit to the data yields an activation energy E_{act}=8 ± 1 kJ/mol.

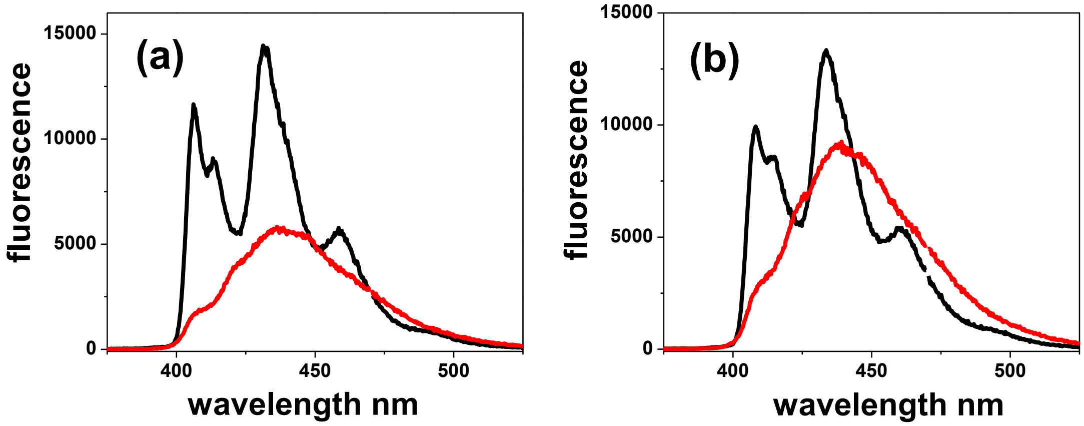

Figure 3-8 Steady-state fluorescence spectra of (a) C1 and (b)C6 in Zeonex at 298K (red) and 77K (black)

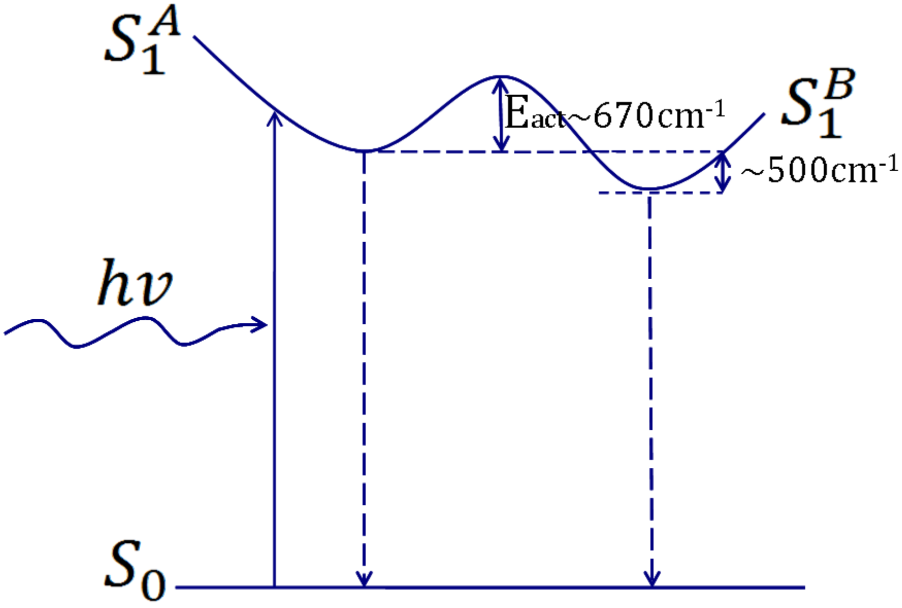

Figure 3-9 Energy level model for 2,6-dialkoxy anthracenes: the barrier height is obtained from the data in Figure 3-7, and the energy difference between the minima is ~500cm^{-1} as deduced the from the spectral shifts in Figure 3-4(a).

3.3 Discussion

The nature of the lower energy state *B* is not entirely clear. The fact that its spectral shape is different from that of *A* is an argument against simple energy shifting due to solvent rearrangement. The lack of a strong solvatochromic effect on either the absorption or fluorescence spectra provides further evidence that polar solvation dynamics are probably not responsible for the observed spectral evolution of the fluorescence. The dependence of the fluorescence relaxation rate on solvent and on alkyl chain length suggests that this process involves some sort of intramolecular motion, possibly a conformation change in the alkoxy sidegroups. CH_2Cl_2 is roughly half as viscous as cyclohexane, so a simple argument based on viscous drag predicts the opposite trend to what is observed. The rotational motion of a polar solute occurs more rapidly in nonpolar solvents[8-9], and this may provide a better explanation for the faster relaxation in cyclohexane. If the conversion between one conformer and the second involves motion of a polar group, that motion would be more rapid in a nonpolar solvent, where the dielectric friction would not be as large a factor. From the spectra in **Figure 3-6**, the energy difference between the two conformers appears to be ~500 cm^{-1}. This value is close to the energy difference observed for conformers of jet-cooled phenoxy compounds[10-11] and benzo-crown ethers.[12-13] In those experiments, the different energy conformers correspond to different rotations of the ether carbon-oxygen group out of the plane of the aromatic ring. Using our B3LYP calculations, other possible minima of the relaxed S_1 geometry of 2,6-dimethoxyanthracene were searched for by changing the torsion angle of the methoxyl group manually before the geometry optimization. The planar geometry found originally was shown to be the lowest energy conformation, and we were unable to resolve additional minima using this method.

The presence of a low energy conformer in **C1**-**C6** has several implications for the photophysics of these molecules. First, it may help explain the anomalously high fluorescence quantum yield of these compounds, which is close to unity in the absence of oxygen. As pointed out by earlier workers, most alkoxy-anthracenes whose fluorescence spectra resemble that of **An** have fluorescence quantum yields below 50% due to efficient intersystem crossing from the S_1 state [3]. If the S_1 state of **C1**-**C6** can adopt a different electronic structure less amenable to intersystem crossing, this would lead to the higher fluorescence quantum efficiency that is observed. The results of our spectroscopic characterization of the dialkoxyanthracenes in dilute solution also have implications for their study in the solid-state. First, the addition of the alkoxy groups at the 2 and 6 positions profoundly alters the electronic properties of the core anthracene moiety. While in **An** the oscillator strength is concentrated almost completely in the lowest energy $S_0 \rightarrow L_a$ transition, in **C1**-**C6** the oscillator strength is shared almost equally between the $S_0 \rightarrow L_a$ and $S_0 \rightarrow L_b$ transitions. This leaves the lowest energy transition with a smaller TDM and weaker dipole-dipole interactions with neighboring molecules. These weaker interactions would presumably lead to less pronounced excitonic effects in the solid state. The different orientation of the TDM in the molecular frame will also lead to different intermolecular interaction terms in the crystals as compared to **An**, even if the packing arrangements are similar. Finally, the presence of a thermally activated conformational change in the excited state results in a temperature-dependent fluorescence lineshape for the monomer itself. One of the key tools we have used previously to measure intermolecular excitonic effects in polyacenes involves analyzing how the vibronic structure of the emission lineshape changes with temperature, in particular the 0-0/0-1 vibronic peak ratio [7, 14-15]. The data in **Figure 3-6** show how a simple steady-state measurement of the fluorescence of an isolated molecule can also exhibit a dramatic change in the apparent 0-0/0-1 peak ratio. Of course, this change originates from the contributions of two molecular conformers, as opposed to the single thermalized exciton population seen in crystalline anthracene and tetracene. Nevertheless, this work shows that caution must be used when attempting to distinguish between intra- and intermolecular effects on the temperature-dependent luminescence spectrum. Clearly, experiments that characterize the photophysics of the isolated molecule in dilute solution are a necessary first step before proceeding to the spectroscopy of the same molecule in a neat solid.

3.4 Conclusion

In this Chapter, we describe the characterization of a series of 2,6 dialkoxyanthracenes. When compared to unsubstituted anthracene, the spectroscopic properties of compounds **C1-C6** are quite different: the oscillator strength appears to be evenly distributed between the L_a and L_b states, rather than concentrated in the low-energy L_a state, and the orientation of the transition dipole moment in the molecular frame is rotated by ~30°. More importantly, all three molecules appear to undergo an intramolecular conformational change in the excited state that gives rise to a time-dependent reshaping of the fluorescence spectrum. The kinetics of this change depend on both the alkoxy chain length and the solvent. This process is thermally activated, and by ~150 K the fluorescence spectrum reflects only the high energy conformer, whose emission lineshape is similar to that of unsubstituted anthracene. The unexpectedly complex excited state behavior in this family of anthracene derivatives makes comparing their solid-state spectroscopy to that of crystalline anthracene more challenging than we first anticipated. Nevertheless, in next chapter the luminescence properties of single crystals of **C1-C6** are going to be discussed. We will attempt to correlate the trends in optical spectroscopic properties with trends in molecular packing and interactions.

References

1. McDowell, L.S., *The Fluorescence and Absorption of Anthracene.* Phys. Rev., 1908. **26**(Copyright (C) 2012 American Chemical Society (ACS). All Rights Reserved.): p. 155-69.
2. Sinha, S.P., *Optically catalytic action of anthracene and phenanthrene in giving Raman shifts of some organic compounds.* Indian J. Phys., 1944. **18**(Copyright (C) 2012 American Chemical Society (ACS). All Rights Reserved.): p. 38-46.
3. Brotin, T., et al., *Photostationary fluorescence emission and time resolved spectroscopy of symmetrically disubstituted anthracenes on the meso and side rings: the unusual behavior of the 1,4 derivative.* Photochem. Photobio., 1992. **55**: p. 349-358.
4. Brotin, T., et al., *Electronic absorption properties of symmetrical dialkoxyanthracenes. Linear dichroism and magnetic circular dichroism.* Photochem. Photobio., 1992. **55**: p. 335-347.
5. Birks, J.B., *Photophysics of aromatic molecules*. 1970, New York: Wiley. 704.
6. Applequist, J., *Theory of solvent effects on the visible absorption spectrum of b-carotene by a lattice-filled cavity model.* J. Phys. Chem., 1991. **95**: p. 3539-3545.
7. Ahn, T.S., et al., *Experimental and theoretical study of temperature dependent exciton delocalization and relaxation in anthracene thin films.* J. Chem. Phys., 2008. **128**: p. 054505/1-054505/11.

8. Madden, P. and D. Kivelson, *Dielectric friction and molecular reorientation.* J. Phys. Chem., 1982. **86**: p. 4244-4256.
9. Horng, M.-L., J.A. Gardecki, and M. Maroncelli, *Rotational dynamics of Coumarin 153: time-dependent friction, dielectric friction, and other nonhydrodynamic factors.* J. Phys. Chem. A, 1997. **101**: p. 1030-1047.
10. Zehnacker, A., et al., *Laser induced fluorescence of jet-cooled non-conjugated bischromophores: bis-phenoxymethane and bis-2,6-dimethylphenoxymethane.* Chem. Phys., 1996. **208**: p. 243-257.
11. Shubert, V.A., et al., *Entropy-driven population distributions in a prototypical molecule with two flexible side chains: o-(2-acetamidoethyl)-N-acetyltyramine.* J. Chem. Phys., 2007. **127**: p. 234315/1-234315/21.
12. Kusaka, R., Y. Inokuchi, and T. Ebata, *Laser spectroscopic study on the conformations and the hydrated structures of benzo-18-crown-6-ether and dibenzo-18-crown-6-ether in supersonic jets.* Phys. Chem. Chem. Phys., 2007. **9**: p. 4452-4459.
13. Shubert, V.A., W.H. James, and T.S. Zwier, *Jet-cooled electronic and vibrational spectroscopy of crown ethers: benzo-15-crown-5 ether and 4'-amino-benzo-15-crown-5 ether.* J. Phys. Chem. A, 2009. **113**: p. 8055-8066.
14. Lim, S.H., et al., *Exciton delocalization and superradiance in tetracene thin films and nanoaggregates.* Phys. Rev. Lett., 2004. **92**: p. 107402/1-107402/4.
15. Spano, F.C., *The spectral signatures of Frenkel polarons in H- and J-aggregates.* Acc. Chem. Res., 2010. **43**: p. 429-439.

Chapter 4 Solid-state Properties of Alkoxy-Anthracenes

4.1 Introduction

The ultimate goal of this project is to elucidate the mechanism of Frenkel exciton transfer in anthracene molecular crystals[1]. The synthesis and photophysical properties of 2,6 dialkoxyanthracene isolated molecules were reported in Chapter 2 and Chapter 3. The next step entails the study of their photophysical properties in solid state. Dialkoxyanthracene crystal structures were analyzed and compared with each other. The influence of different alkoxy groups on molecular geometry and crystal packing is discussed. To clarify the intermolecular excitonic interactions in 2,6 dialkoxyanthracenes, the most efficient way is to compare their solid-state optical spectroscopic properties to that of crystalline anthracene (**An**). Anthracene solid-state samples, such as anthracene polycrystalline films and single crystals, have been widely studied during the past 50 years[2-7]. Our research presented here builds on this in that the photophysical properties of **C1-C6** evaporated films are compared with their unsubstituted counterparts while the **C1-C6** single crystals are discussed in comparison to their anthracene single crystal counterpart. Unlike anthracene, whose solid-state aggregate only has one type of crystal packing (the herringbone structure[8]), 2,6 dialkoxyanthracene aggregates can possess different packing patterns, depending on how they were prepared.

The Frenkel exciton in anthracene solid samples is a J-type aggregate[9]. Excitons in J-aggregates tend to condense into the lowest excitation state, leading to the superradiant emission from this state with decreasing temperature. Additionally, J-aggregates are characterized by an enhancement of the 0-0 vibronic peak at low temperature due to the enhancement of the exciton coherence volume. In contrast, H-aggregates, which are not so popular in terms of exciton transfer, demonstrate the opposite spectroscopic signatures.

4.2 Crystal Structures of C1-C6 Single Crystals

We conducted the X-ray crystallographic analysis of **C1-C6** in order to investigate the influence of varying the length of the alkoxy chain on molecular packing in single crystals. The crystal structures of the three derivatives are shown in **Figure 4-1**, with their relevant structural parameters listed in **Appendix A, B** and **C** at the end of this dissertation. As hoped, lengthening the alkyl tail had a strong effect on the crystal packing. **C1** adopts a herringbone packing motif, similar to **An**. **C3** shares the herringbone packing motif, but the molecules are more offset vertically from each other, leading to a tilted plane. In **C6**, the longer alkyl chains force the anthracene moieties to pack into a two-dimensional sheet, but now in a face-to-face orientation rather than a herringbone motif. The qualitative changes in crystal structure initiated by the presence of the substituents at the 2 and 6-positions can be expected to lead to substantial differences in the optical and electronic properties of the solids. From the crystal structures in **Figure 4-1**, it is clear that our strategy of varying the alkyl chain can induce different crystal packing geometries in this series of dialkoxyanthracenes.

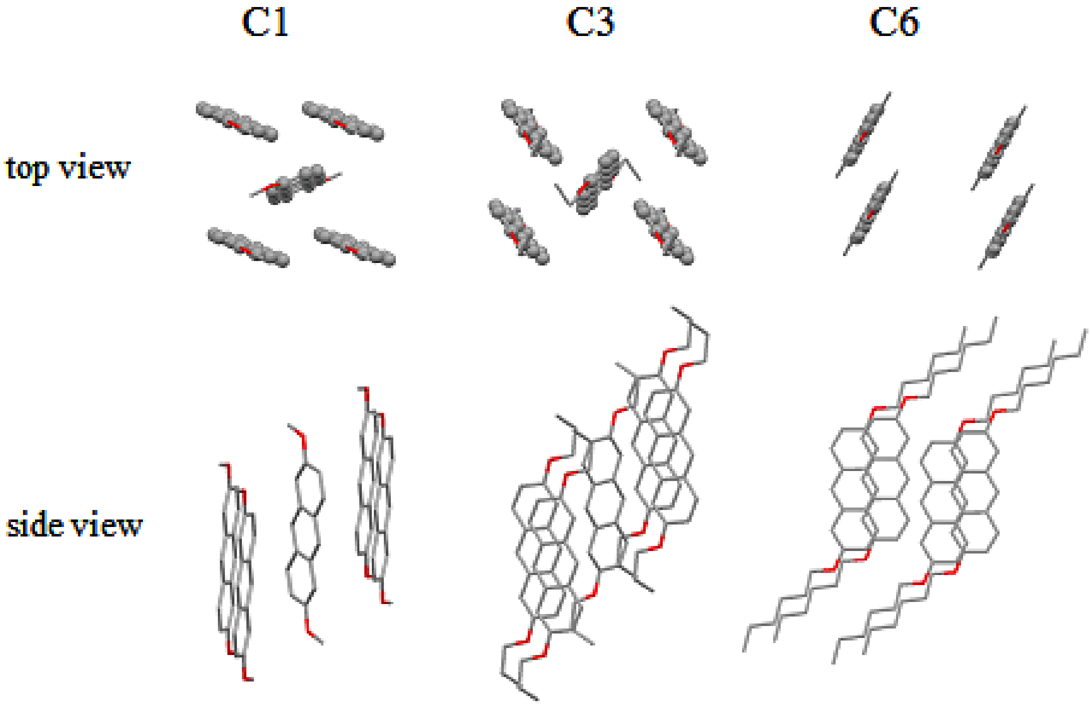

Figure 4-1 Packing patterns of C1-C6 single crystals

Though the anthracene units in all **C1**-**C6** are strictly planar, their crystal packing patterns do not adopt π-π stacking that leads to the face-to-face overlap of anthracene moieties. The Van der Waals forces between carbon chains were supposed to induce more rigid molecular packing with lengthening alkyl chain[10]. Both **C1** and **C3** appear to be packed in the herringbone structure, which is the typical 2-D arrangement in unsubstituted anthracene. The inter-planar tilted angles between anthracene moieties in two adjacent molecules are 46.6° for C1 and 70.6° for **C3**. In contrast, **C6** adopt a slipped-parallel packing with one-dimensional arrangements. The stacking diagrams are shown in **Figure 4-2**.

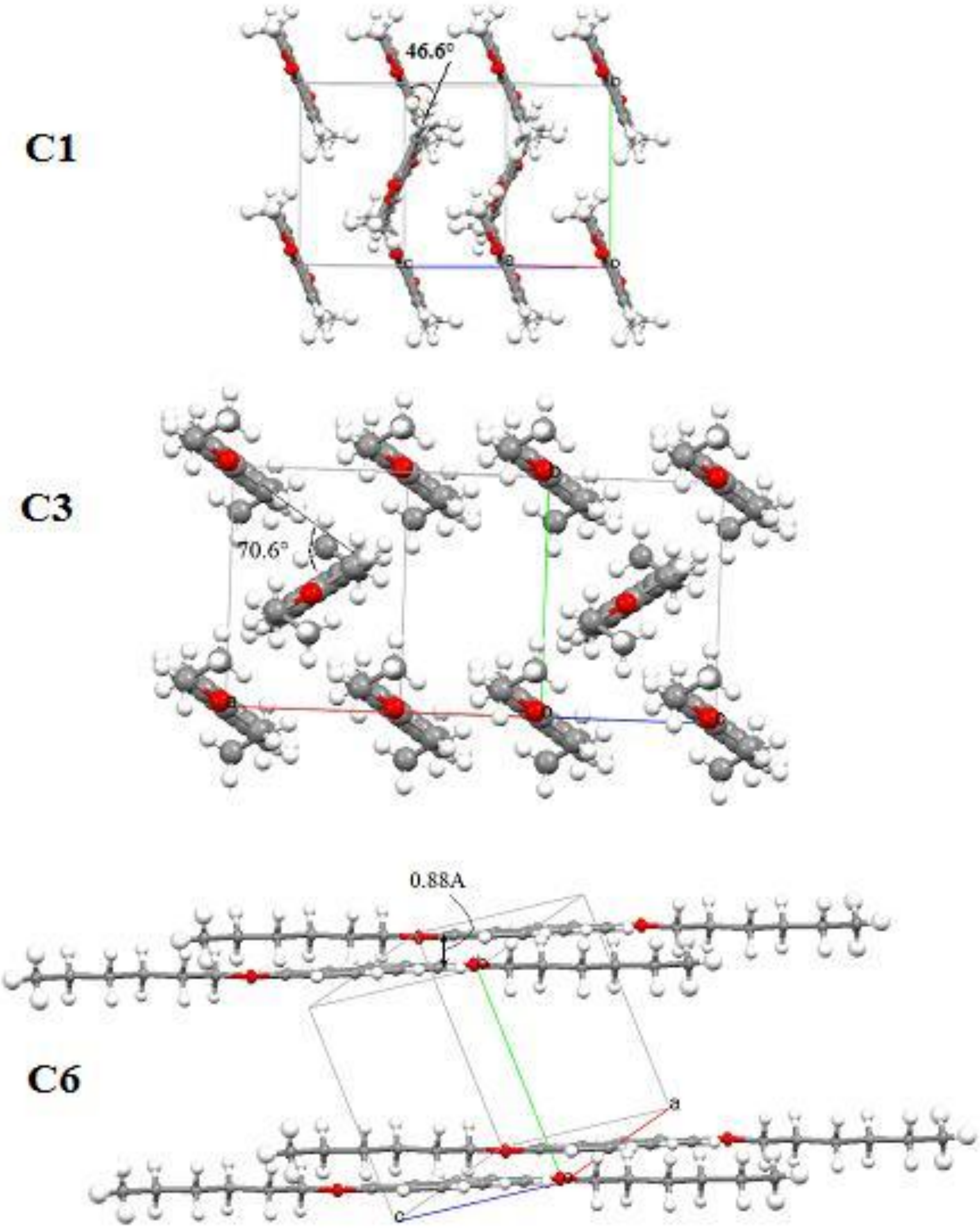

Figure 4-2 Parameters of packing patterns of C1, C3 and C6.

There is a center of symmetry in all **C1-C6** molecules. The **C1** and **C3** crystal systems were the monoclinic $P2_1/c$ and **C6** crystal system was triclinic P-1. The slip distance between adjacent **C6** anthracene unit planes is 0.88A. The carbon side chains are planar with anthracene ring in **C1** and **C6** crystals while **C3** side groups show a trans conformation with the anthracene ring. The two $-CH_3$ groups in 2 and 6 positions of **C3** molecules extend upward and downward out of the anthracene plane, making **C3** a chair-form molecule. The alkoxy groups in **C1-C6** show all-trans conformation like other hydrocarbon chains always found in X-ray analysis.

The distances between adjacent molecules are 8.18Å, 8.16Å and 7.97Å for **C1, C3** and **C6** respectively (see **Figure 4-3**). With elongation of side chains, the distances between adjacent molecules become shorter.

According to our observation, both the molecular geometry and the crystal packing were closely related to the length of the alkoxy side chains. **C1-C6** molecular structures were viewed from three directions that are perpendicular to each other, as shown in **Figure** 4-4. Two types of interactions exert strong influence on molecular packing: the π-π stacking between aromatic units and the interaction between alkoxy chains. The two forces compete with each other, determining the molecular packing in single crystals. None of the **C1-C6** crystals exhibit strong π-π stacking between aromatic rings. With extension of the alkoxy group, interaction between carbon chains becomes a decisive factor to promote the lamellar structure in **C6** single crystal. Our assumption that we can change the crystal packing via tuning the side chain length seems promising since the crystal structures of **C1-C6** aggregates have already evolved from herringbone to lamellar.

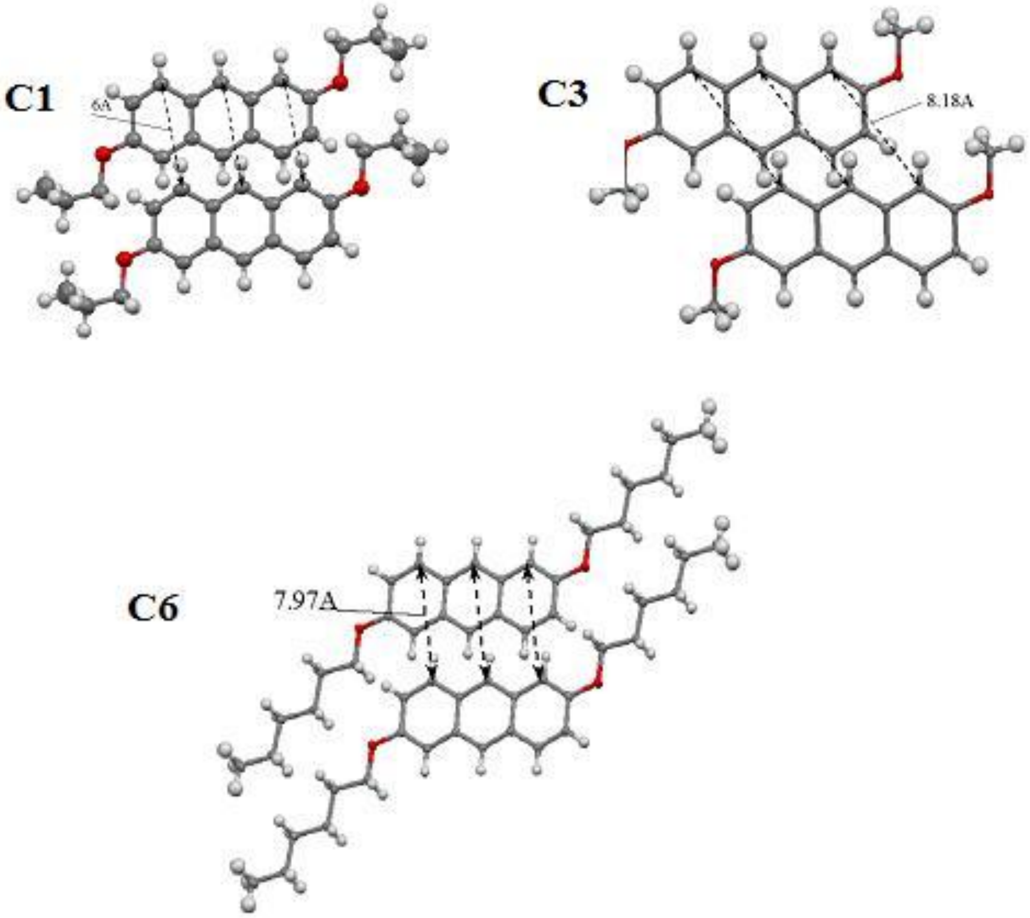

Figure 4-3 Stacking structures of C1, C3 and C6 adjacent molecules

.

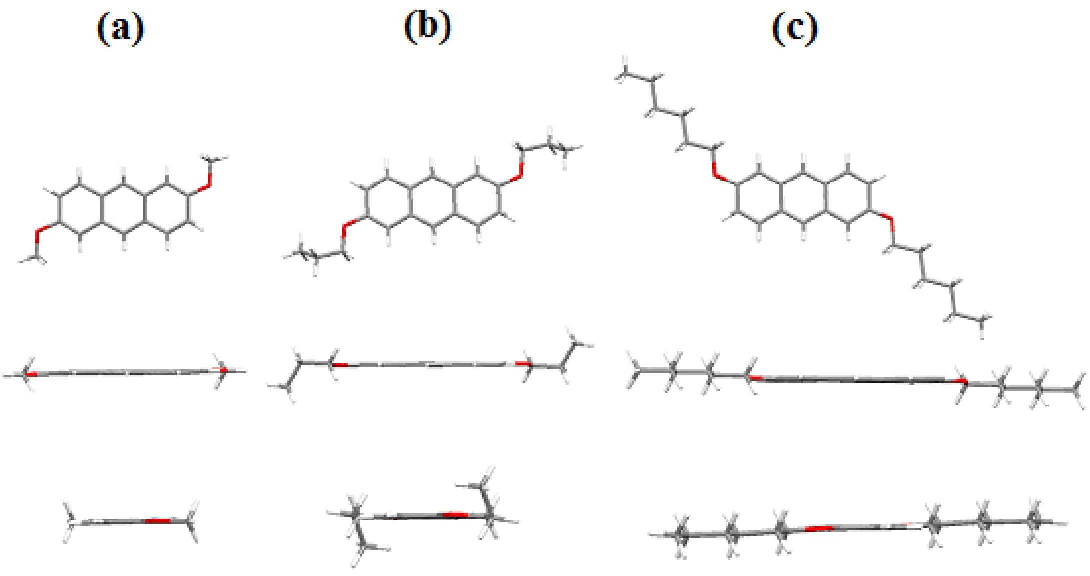

Figure 4-4 Molecular structures of C1(a), C3(b) and C6(c).

4.3 Powder X-Ray Diffraction (PXRD) Analysis

Before further discussing the exciton structure modification of **C1-C6** solid-state samples, the variability of crystal packing of the 2,6 dialkoxyanthracenes in different solid samples should be clarified. Unsubstituted anthracene only has one type of aggregation in the solid state, which is known as the herringbone packing[11]. no matter if it is grown from vapor or solutions. In our previous assumption, the 2,6-dialkoxyanthracenes should also obtain the same packing motif independent of the preparation method. However, the powder X-ray diffraction (PXRD) results of those evaporated films overthrew our initial assumption. The 2,6 dialkoxyanthracenes tend to aggregate in more than one way when prepared via different methods.

The samples for PXRD were prepared via the following method: the solution-grown crystals were grounded into powder in a mortar with a pestle and then put on a pre-cleaned glass substrate. The sublimation crystals for the PXRD studies were grown in the same way as the growth of anthracene single crystals as detailed in Chapter 2. Crystals were then ground fine and loaded onto the substrate, similar in fashion to the solution-grown samples. The calculated PXRD patterns were based on the X-ray analysis of the **C1-C6** solution-grown single crystals. Comparison of the experimental PXRD results with the calculation indicates that all sublimation films seem to obtain different crystal structures from their solution-grown single crystal counterparts. The **C1** and **C6** films may be only partially crystallized (see Figure 4-5), and therefore difficult to compare with the calculated PXRD patterns. The most highly crystallized film is the **C3** film. The PXRD peaks of the sublimed **C3** crystals do not match up with our calculation. Those corresponding to the ground **C3** solution-grown crystals however correspond rather well with our calculations as seen in Figure 4-6. The relative peak intensities, however, are not exactly the same as our calculation. One possible reason is that the crystals may not be ground fine enough so certain Miller planes were hidden in the un-cracked crystal planes.

The conclusion of these comparisons of the PXRD data is that there is some evidence that different growth conditions lead to different crystal polymorphs of **C1-C6**, in contrast to **An**.

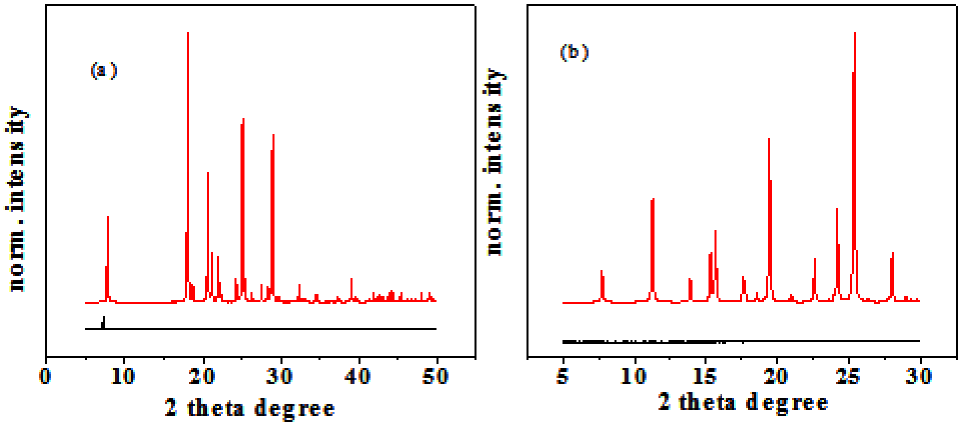

Figure 4-5 Calculated(red) and experimental(black) powder X-ray diffraction (PXRD) of C1(a) and C6(b)

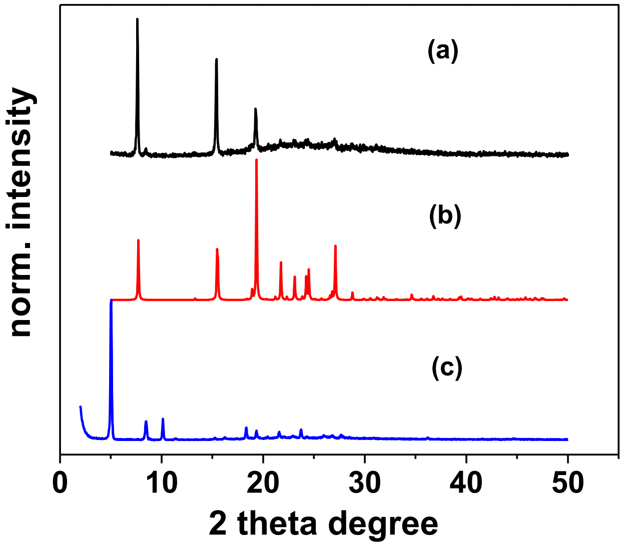

Figure 4-6 C3 powder X-ray diffraction (PXRD) from (a) ground solution-grown crystals (b) calculation of single crystal analysis (c) ground crystals grown from sublimation

4.4 Spectroscopy of An and C1-C6 Evaporated Films

C1-C6 and **An** evaporated films were prepared in the home-made evaporator as described in Chapter 2. Time-resolved fluorescence experiment was conducted on **An/C1-C6** films and single crystals using the 266 nm laser pulses and the experimental set-up described in Chapter 2. The excitation wavelength is monitored at 266 nm because it can minimize the penetration depth of the exciting light within the solid-state samples to cut down on self-absorption. The extinction coefficient at 266 nm is roughly ~12 times of that at 400 nm. The steady-state absorption and fluorescence spectra of **C1-C6** evaporated films are shown in **Figure 4-7.** All three films seem to possess a similar steady-state absorption band and fluorescence emission progression at room temperature.

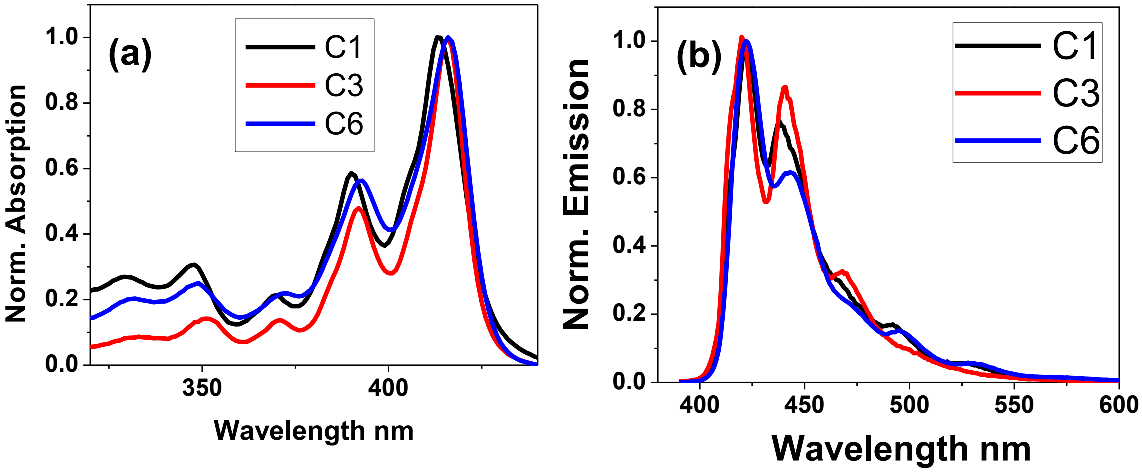

Figure 4-7 Steady-state absorption(a) and fluorescence emission (b) of C1, C3and C6 evaporated films

The absorption and emission bands tend to be more symmetric and overlap more in the evaporated films than in the solutions. The fluorescence emission outlines are also more pronounced in the films. Compared with the steady-state absorption spectra for the **C1-C6** solutions, the peak absorption in the evaporated films has undergone a red-shift of ~ 10 nm (see **Figure 4-8),** implying that the transition dipole moments (TDMs) have redistributed between the lower energy L_a state and the higher energy L_b state. The L_a state is significantly more favored and tends to obtain higher exciton density in the evaporated films than in the solutions. Therefore, the excitons in the **C1-C6** evaporated films should condense in the lowest energy state, the same phenomena that gives rise to the superradiance observed in polycrystalline anthracene films[7]. However, the temperature-dependent steady-state emission from the **C1-C6** evaporated films change significantly once the evaporated films are cooled down as shown in **Figure 4-9**. Though their fluorescence emission intensities are all greatly enhanced as the temperature is decreased, **C1** shows an opposite trend to **C3** and **C6. C1** emission sharpens with the decrease in temperature while the short-wavelength peaks (~ 420 nm) become greatly enhanced, just like pure **An**. **C3** and **C6** spectral outlines did not narrow with the change in peak ratios at lower temperatures. Judged only from the steady-state fluorescence spectra, the temperature-dependent emission behavior of **C1** is quite similar to pure **An**, while **C3** and **C6** are not.

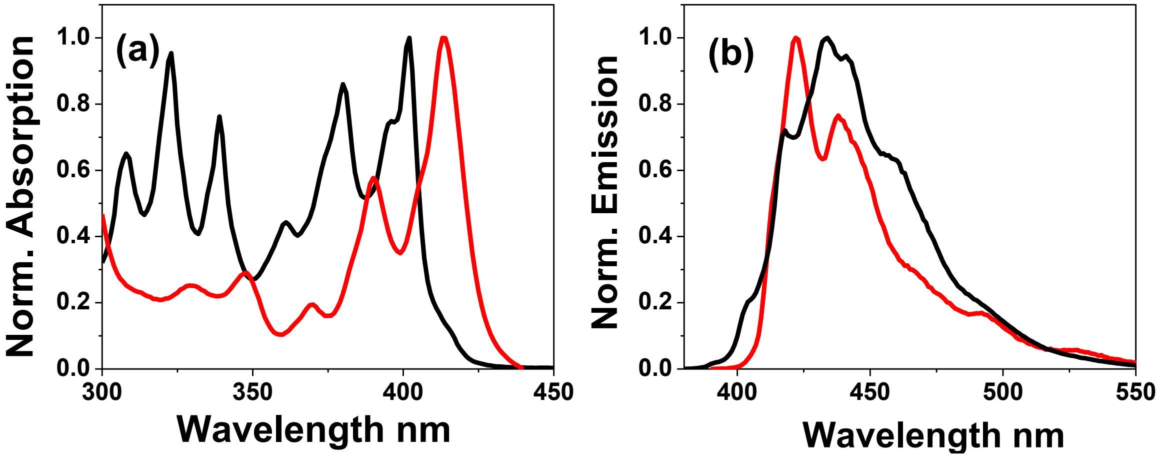

Figure 4-8 Steady-state absorption(a) and fluorescence emission(b) of C1 in cyclohexane solution (black) and C1 evaporated films (red)

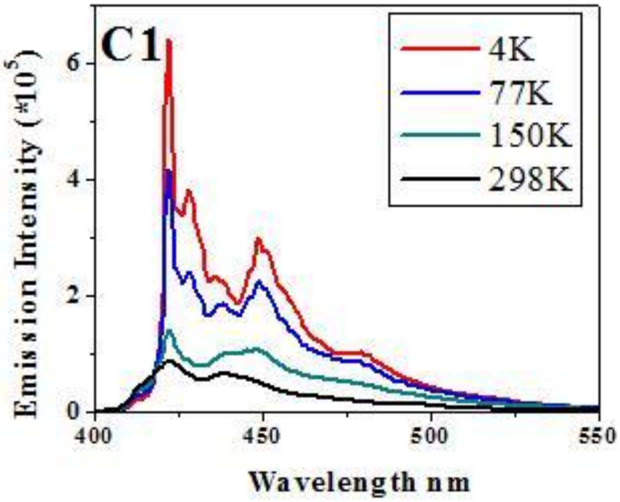

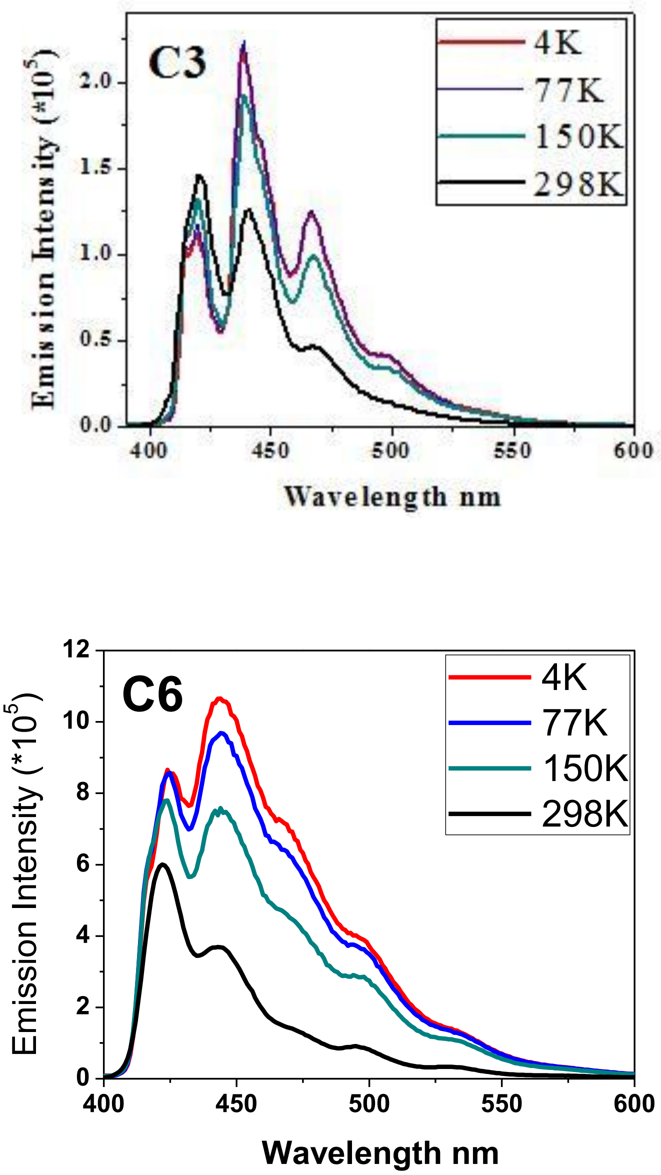

Figure 4-9 Steady-state fluorescence emission of C1/ C3/C6 evaporated films at different temperatures.

The spectral shapes of the time-resolved fluorescence emission for the **C1-C6** films (see **Figure 4-10, Figure 4-11** and

Figure 4-12) are poorly resolved for the spectra corresponding to the first 1 ns taken from longer time windows. Despite this, red shifts can be discerned to some degree with time no matter what the temperature. The red shifts become more pronounced for all three films at lower temperatures. At room temperature, only the **C1** spectra shifts significantly within the first few nanoseconds. Concerning the fluorescence emission during the first 200 ps, which most likely corresponds to the intrinsic exciton emission state, the blue edge (~ 420 nm) of the **C1** film emission is clearly enhanced at 77 K. The corresponding initial emission spectra of the **C3** and **C6** films on the otherhand, almost overlap at when comparing their individual 77 K and room spectra to each other. According to the theoretic calculation[7], the 0-0 to 0-1 peak intensity ratio is a simple way to measure of the exciton coherence length. The enhancement of blue edge emission corresponding to the 0-0 peak is a notable sign of increasing exciton coherence length. When comparing the fluorescence decays of **C1-C6** films (see **Figure 4-13**) at room temperature with those at 77 K, all their emissions decay faster at room temperature. The fluorescence kinetics of the **C1-C6** films indicate that they all contain more than 2 emitting species, which may be attributed to various structural defects.

The different fluorescence behaviors of these 2,6-dialkoxyanthracene evaporated films provide some evidence that adjusting the alkoxy chain length can vary the Frenkel excitons within these aggregates. None of the **C1-C6** evaporated films have demonstrated typical characteristics of J-type aggregates, like **An**. The lack of the crystal packing information of the **C1-C6** evaporated films makes quantitative analysis of the spectroscopy more challenging.

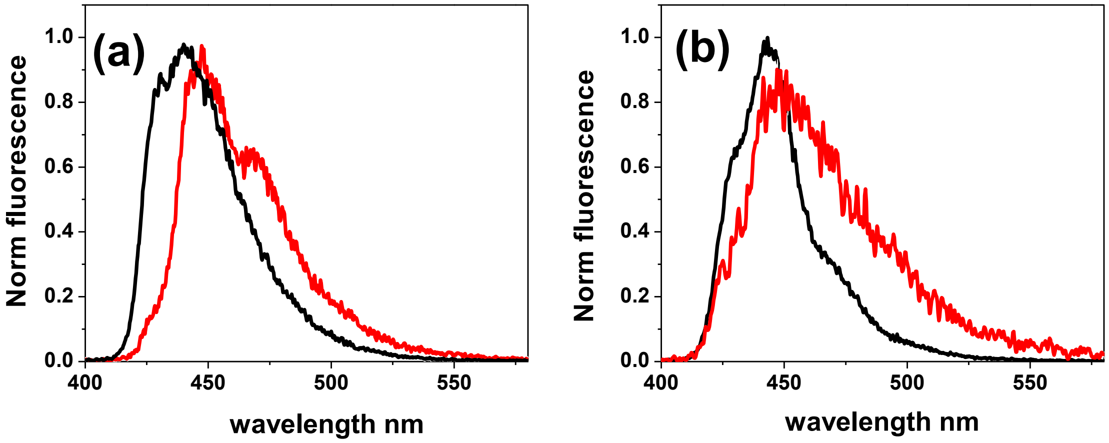

Figure 4-10 Time-resolved fluorescence emission spectra of C1 evaporated film(black: integrated from first 200 ps; red: integrated from 4-5 ns) at (a)77 K (b)298 K

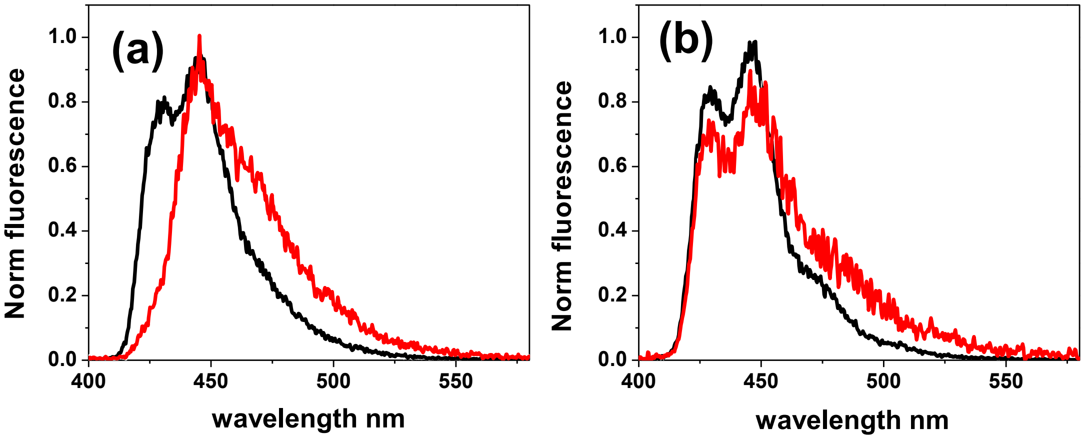

Figure 4-11 Time-resolved fluorescence emission spectra of C3 evaporated film(black: integrated from first 200 ps; red: integrated from 4-5 ns) at (a)77 K (b)298 K

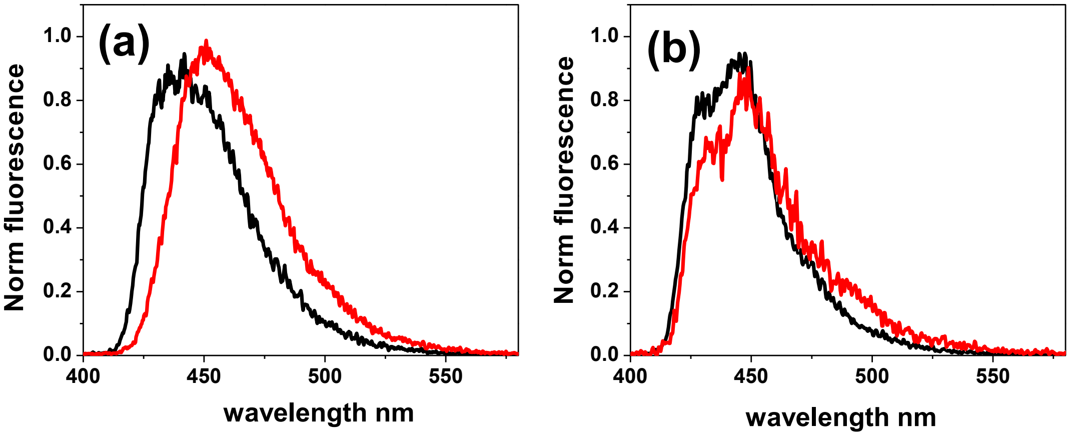

Figure 4-12 Time-resolved fluorescence emission spectra of C6 evaporated film(black: integrated from first 200 ps; red: integrated from 4-5 ns) at (a)77 K (b)298 K

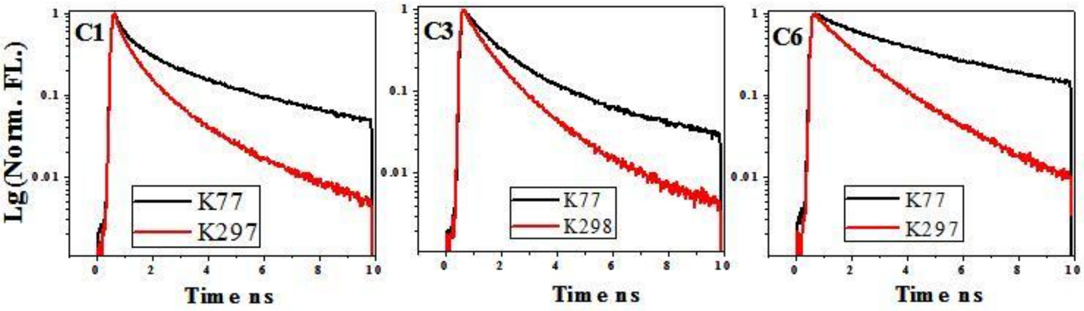

Figure 4-13 Time-resolved fluorescence decays of C1, C3 and C6 evaporated films in 10 ns window at 77 K (black) and room temperature (red)

4.5 Spectroscopy of An and C1-C6 Single Crystals

After examining polycrystalline thin films, we then concentrated on the solution-grown single crystals whose crystallography information was already been obtained. The **C1-C6** single crystals were grown as described in Chapter 2. **Figure 4-14** shows the steady-state fluorescence emission of 2,6-dialkoxyanthracene single crystals at different temperatures with an excitation wavelength of 365 nm. For **C1** and **C3** single crystals, the blue-wavelength peaks (around 425 nm) in the fluorescence emission spectra shrank with the decrease in temperature. For **C6**, this phenomenon was not observed. With the elongation of the alkoxy chain, the steady-state fluorescence displays less of a temperature dependence. The luminescence emission of the **C6** single crystal at 77 K overlaps with that of the room temperature spectra. Since the spectral shape may be distorted by self-absorption, luminescence emissions were collected at various excitation wavelengths (320 nm, 280 nm, and 365 nm) on the same **C1** single crystal and got similar temperature-dependent spectra with (see **Figure 4-15**). Thus the trends in the blue emission with temperature are not an artifact of self-absorption.

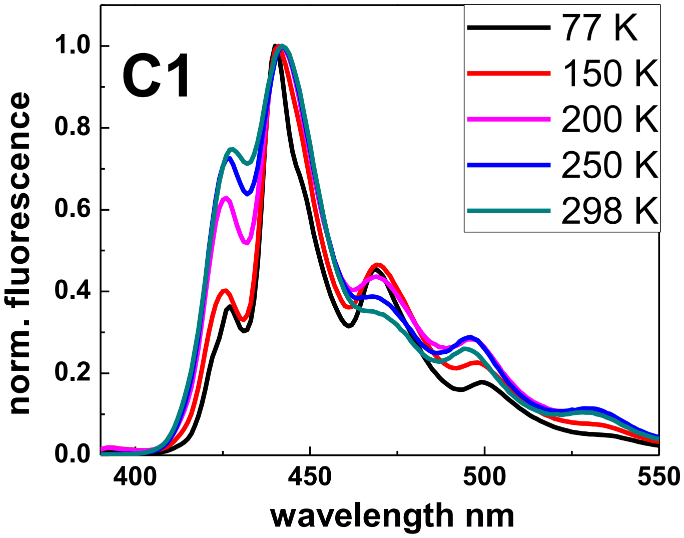
C1
norm. fluorescence
wavelength nm
0.0
0.2
0.4
0.6
0.8
1.0
400
450
500
550
77 K
150 K
200 K
250 K
298 K

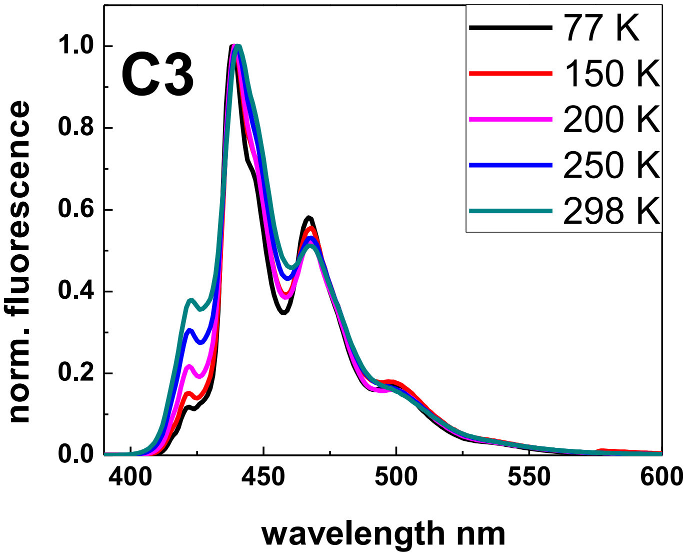
C3
norm. fluorescence
wavelength nm
0.0
0.2
0.4
0.6
0.8
1.0
400
450
500
550
600
77 K
150 K
200 K
250 K
298 K

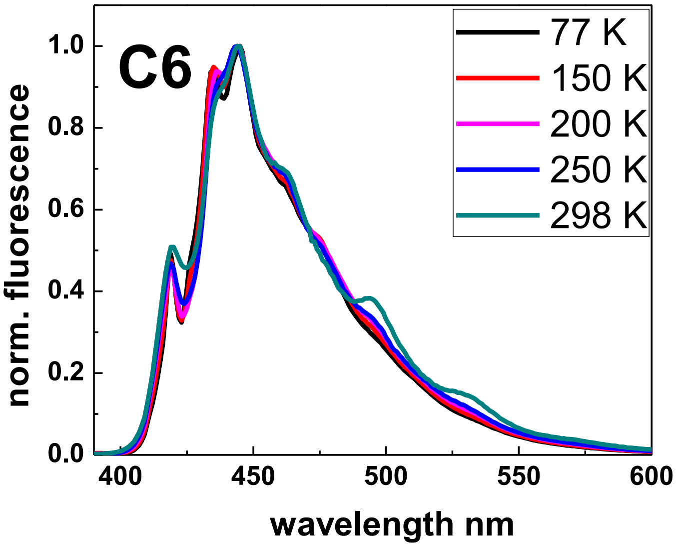

Figure 4-14 Steady-state fluorescence emission of C1, C3 and C6 single crystals at different temperatures

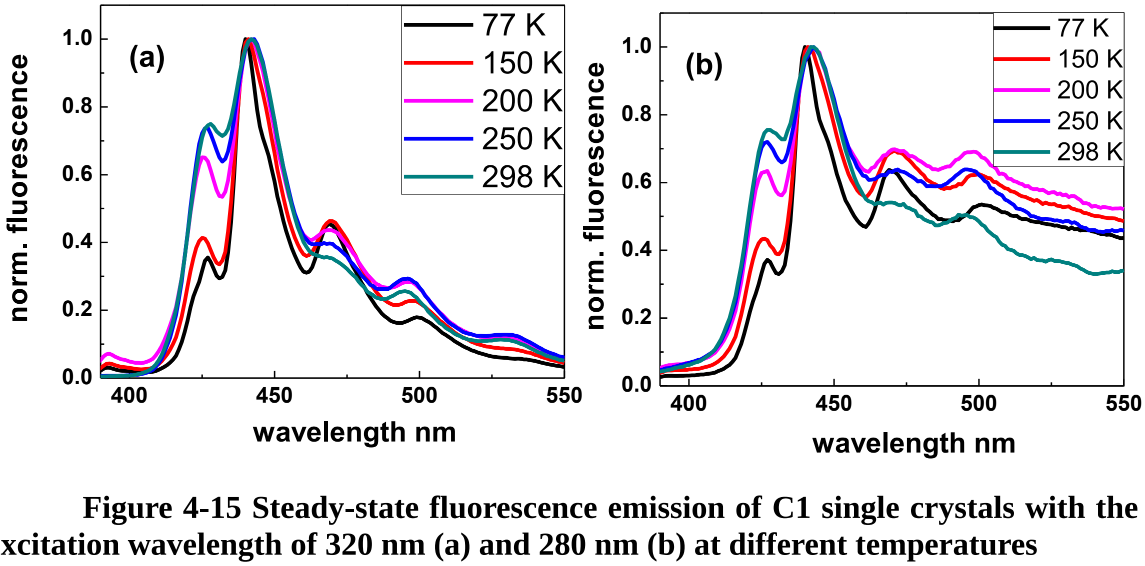

Figure 4-15 Steady-state fluorescence emission of C1 single crystals with the excitation wavelength of 320 nm (a) and 280 nm (b) at different temperatures

Time-resolved temperature-dependent fluorescence spectra of the 2,6-dialkoxyanthracene single crystals were compared with that of an unsubstituted anthracene single crystal. The temperature was lowered with a liquid helium/nitrogen cryostat. In **Figure 4-16**, the time-resolved fluorescence emission spectra of the target single crystals were taken at room temperature and at a low temperature as follows: pure anthracene, **C1** and **C3** were taken at ~ 6 K while **C6** was taken at ~ 80 K. The resolution of the streak camera was tuned to 150 g/mm for all 2,6-dialkoxyanthracene measurements and to 300 g/mm for the anthracene emission. This may explain the reason why we can only observe the sharp vibronic peaks for anthracene at low temperatures. Compared with the fluorescence emissions observed during initial 1 ns after excitation, the spectral emissions in the 7-9 ns time windows for anthracene and **C1** at ~ 6 K clearly exhibit red-shifts and undergo changes in their spectral shapes. The blue-edge peaks, centered at 398 nm in anthracene and 415 nm in **C1,** are enhanced when compared with the longer-wavelength regions. This enhancement of the 0-0 emission peak with decreasing temperature is a typical characteristic of J-type aggregates. The spectral shapes for **C3** and **C6** at low temperatures do not change much with their room temperature spectra. The **C3** blue-edge twin peaks at 417 nm and 423 nm shrank over time, while the red region peaks remained constant with time. **C6** luminescence undergoes a ~ 3 nm red shift between the 1 ns and 7-9 ns time windows, with spectral outlines remaining identical. With the extension of the side carbon chain, the fluorescence emission spectra seem to change less with time at low temperatures. However, the **C6** single crystal was only cooled down to ~ 80 K, which was not as low as the other three target molecules, which may also explain why the **C6** spectral outline shows little change. At low temperature, the luminescence behaviors of both anthracene and **C1** share common J-type aggregate optical properties. In contrast, the spectroscopic properties of **C3** and **C6** show little similarity to anthracene. At room temperature (see **Figure 4-17**), all time-resolved emission peaks are broadened and clearly red-shifted with time except for those of pure anthracene. There are only three observable broad peaks in the emission spectra of the anthracene single crystal at room temperature. Both the blue-edge (~ 406 nm) and red-edge (~ 458 nm) peak intensities decreased with time in the first few nanoseconds when compared to the middle peak at ~ 430 nm.

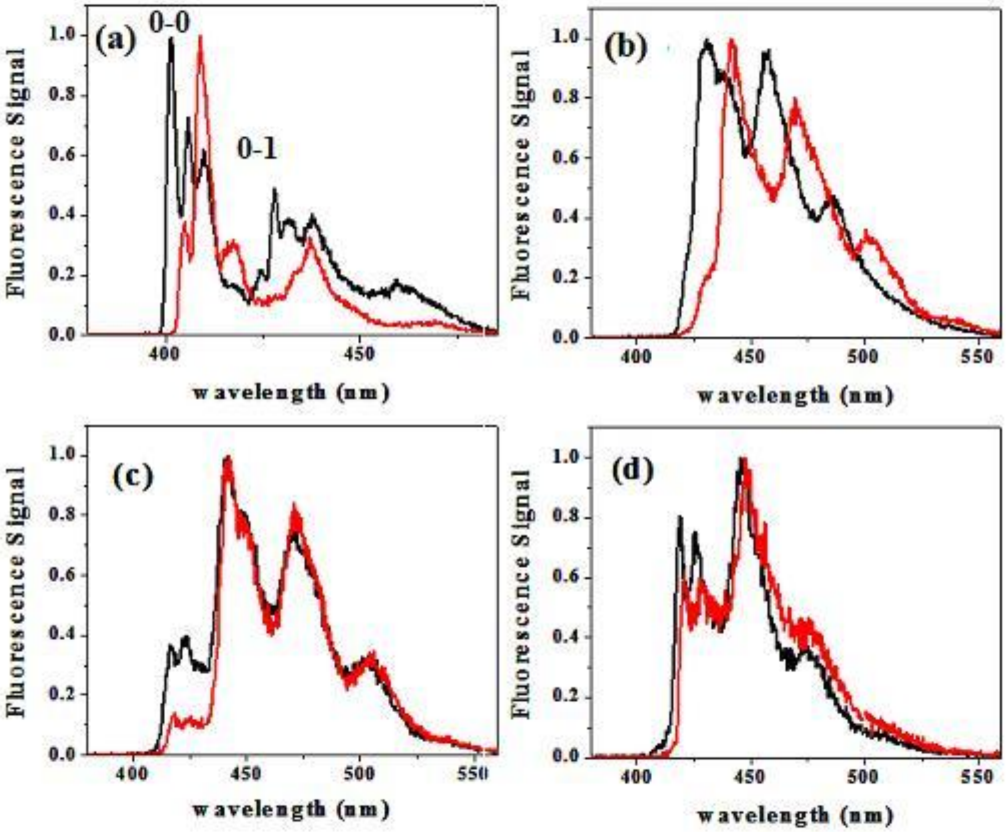

Figure 4-16 Normalized fluorescence spectra from single crystals of 1 ns after laser excitation (black) and 7-9 ns after laser excitation (red) at low temperatures: An at 6 K (a), C1 at 6 K (b), C3 at 6 K (c) and C6 at 80 K (d)

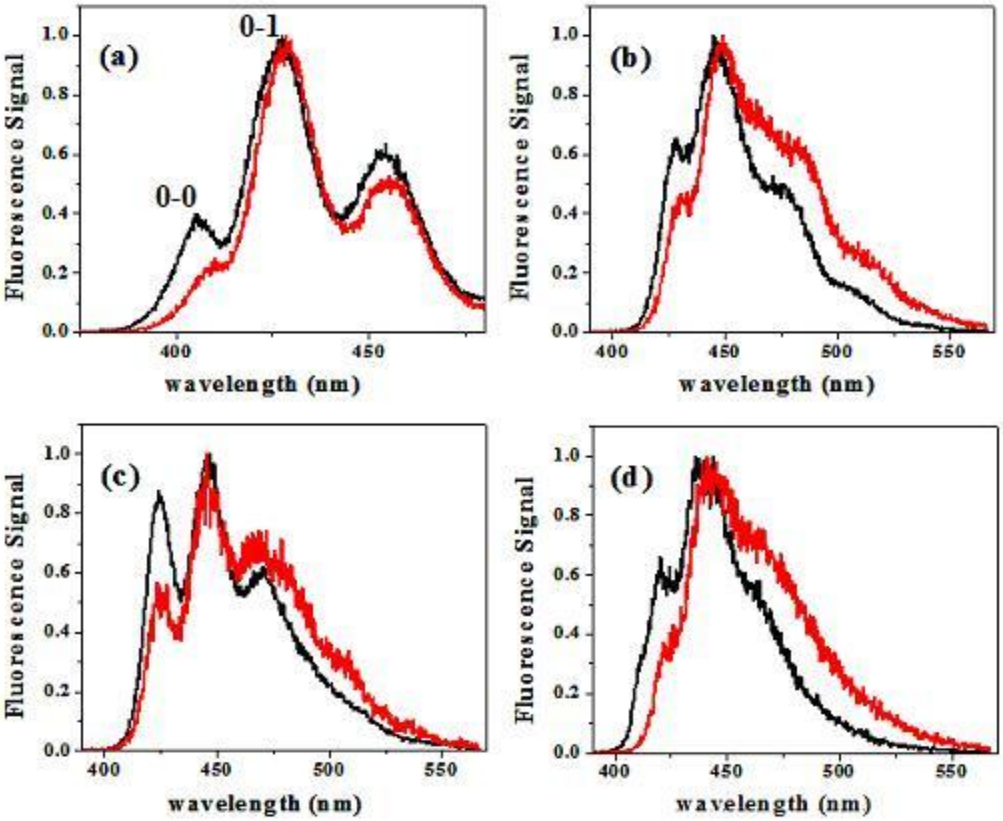

Figure 4-17 Normalized fluorescence spectra from single crystals of 1 ns after laser excitation (black) and 7-9 ns after laser excitation (red) at room temperature: An (a), C1 (b), C3 (c) and C6 (d)

In analyzing the wavelength-resolved fluorescence spectra, I chose a blue region and a red region to monitor with time. The center wavelength used in each region is detailed in **Figure 4-18**, **Figure 4-19** and **Figure 4-20**. There are clearly at least two luminescent species for **C3** at both room temperature and ~ 6 K; one decays and the other grows in. Two luminescent species with reverse kinetic trends were observed at ~ 6 K in anthracene and **C1** single crystal. The blue region (410 nm – 425 nm) decays faster at lower temperature while the red region (500 nm – 525 nm) decays faster at room temperature (see **Figure 4-21**). The former may correspond to the intrinsic exciton and the later probably reflects the defect states. With temperature dropping down, the intrinsic exciton population condenses into lowest excitation band and the radiative decay rate increases. This phenomenon was discussed in previous research[7] as superradiance - the other typical property of J-type aggregates. **C3** single crystals did not show supperadiance at low temperature. More quantitative evaluation together with theoretic work has to be done before making solid judgments.

When we further compare **An** and **C1** single crystals, the fluorescence decays from the blue-edge regions were plotted versus those integrated from the all-wavelength. For the **An** single crystal (see **Figure 4-22**), emission decays faster with decreasing temperature in both cases. For the **C1** single crystal, the blue-edge region emission decays faster at low temperatures, but the fluorescence decay over all wavelengths slightly slows down with decreasing temperature, as shown in **Figure 4-23.** It indicates that the defect states dominate the **C1** all-wavelength emission and there are more crystallographic defects in the **C1** single crystal than in the **An** one. As has been discussed in Chapter 2, **An** single crystals were prepared via sublimation while **C1** single crystals were grown from solution, which may explain the crystal quality difference between **An** and **C1**.

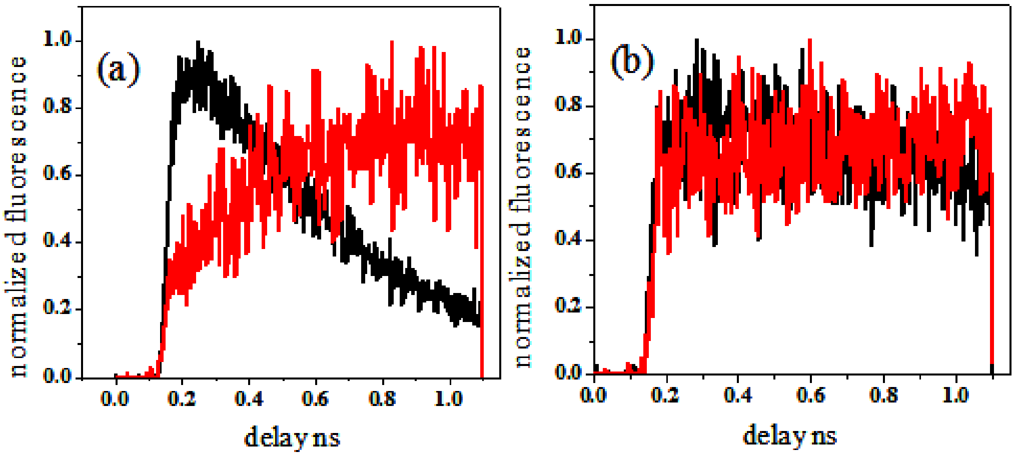

Figure 4-18 Luminescence decays of An single crystals in blue (400 nm, black) and red (470 nm, red) regions at 6 K(a) and room temperature (b)

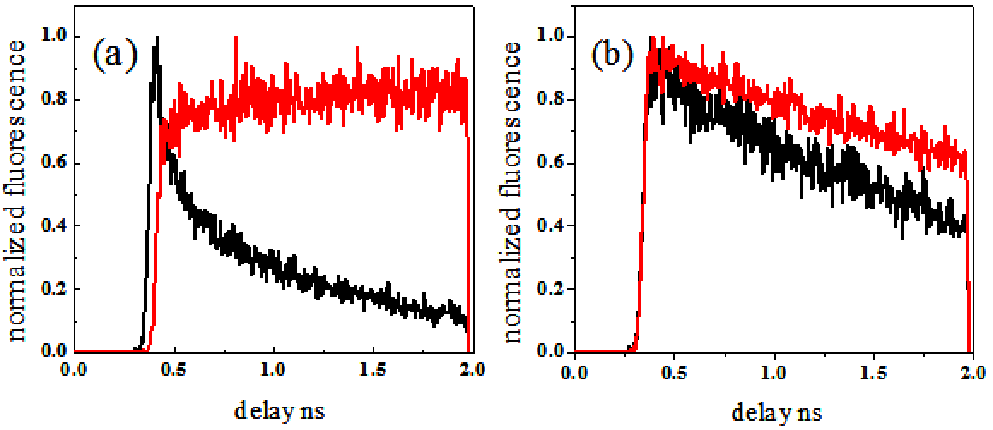

Figure 4-19 Luminescence decays of C1 single crystals in blue (410 nm,black) and red (510 nm, red) regions at 6 K(a) and room temperature (b)

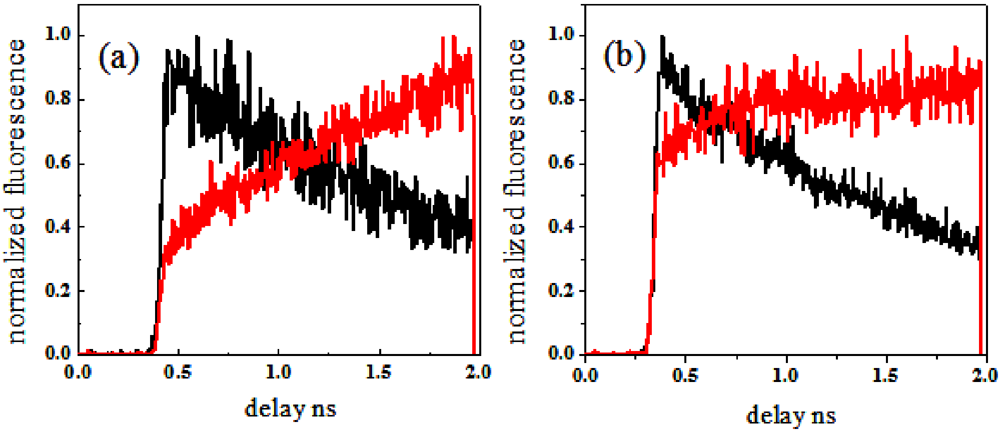

Figure 4-20 Luminescence decays of C3 single crystals in blue (410 nm,black) and red (510 nm, red) regions at 6 K(a) and room temperature (b)

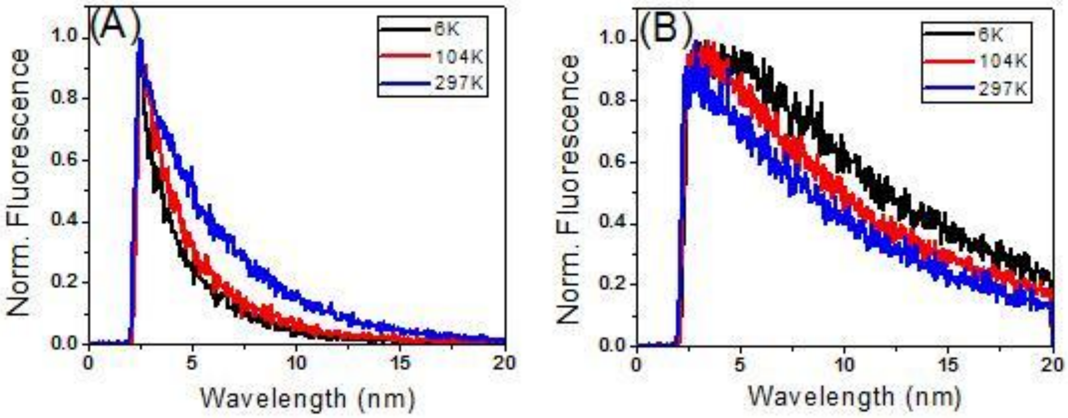

Figure 4-21 Luminescence decays of C1 single crystal in blue region (410 nm-425 nm) (A) and red region (500 nm-525 nm) (B) at different temperatures

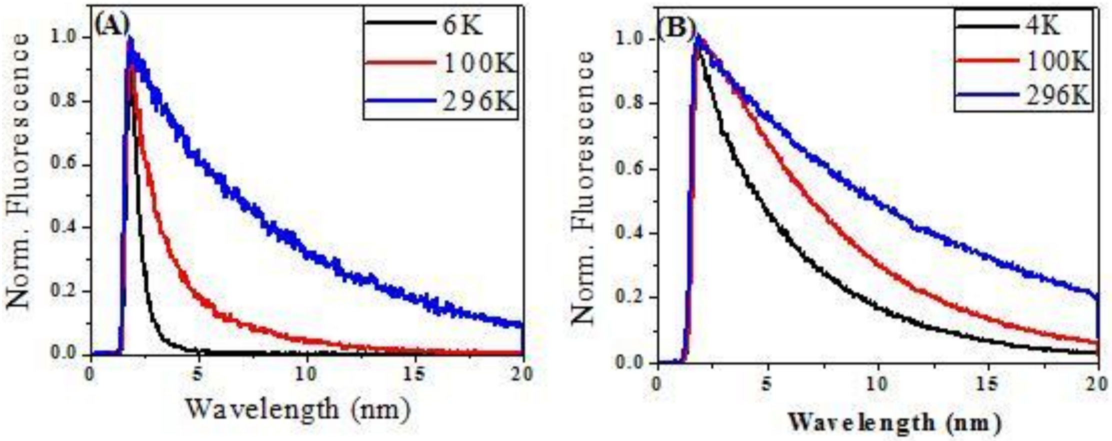

Figure 4-22 Luminescence decays of An single crystal in blue region (400 nm-410 nm) (A) and the all wavelength (B) at different temperatures

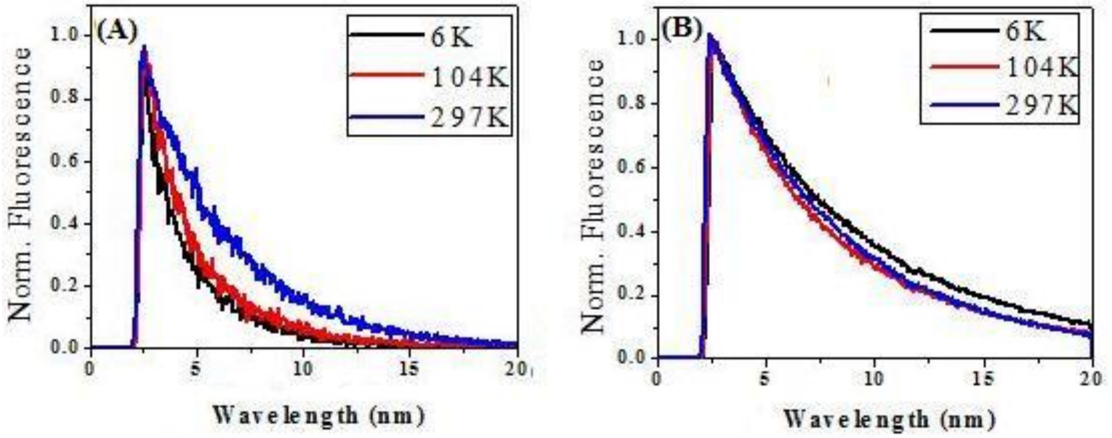

Figure 4-23 Luminescence decays of C1 single crystal in blue region (415 nm-425 nm) (A) and the all wavelength (B) at different temperatures

4.6 Conclusion

The solid-state spectroscopoic properties of 2,6 dialkoxyanthracenes (**C1-C6**) together with that of unsubstituted anthracene (**An**) were discussed in this chapter. Since none of the **C1-C6** evaporated films demonstrated J-type aggregate features, plus there is a lack of their crystal packing information, the research target was switched to their single crystal counterparts. For all three 2,6 dialkoxyanthracene molecules, only the **C1** single crystal shows spectroscopic properties similar to pure anthracene in terms of superradiance and the enhancement of the 0-0 emission peak intensity at low temperatures - two characteristics unique to J-type aggregates. However, with the elongation of the alkoxy side chains, both the molecular geometry and exciton structures were heavily affected by the interaction between the alkoxy side groups. Consequently**,** **C3** and **C6** single crystals did not display typical J-type aggregate features. Our results show that via adding the alkoxy groups of various lengths to an anthracene chromophore, the spectroscopic properties and exciton structures of anthracene-based derivatives can be changed. Additional theoretical calculations that take into account the complexity in the unforeseen coupling between the alkoxy side chains with both each other and the anthracene core would be one way to further analyze the change in the exciton structure with the elongation of the side chains within 2,6 dialkoxyanthracene single crystals.

References

1. Zhou, X., et al., The photophysics of the 2,6 dialkoxy anthracenes: Evidence for excited state side-chain conformational relaxation. Journal of Luminescence, 2012. 132(11): p. 2997-3003.
2. Lyons, L.E. and L.J. Warren, Anthracene fluorescence at low temperatures. I. Purified single crystals. Aust. J. Chem., 1972. 25(Copyright (C) 2012 American Chemical Society (ACS). All Rights Reserved.): p. 1411-25.
3. Lyons, L.E. and G.C. Morris, The intensity of ultraviolet light absorption by monocrystals. III. Absorption by anthracene at 295°K., 90°K., and 4°K. of plane-polarized light of wave lengths 1600-2750 A. J. Chem. Soc., 1959(Copyright (C) 2012 American Chemical Society (ACS). All Rights Reserved.): p. 1551-8.
4. Ferguson, J., Absorption, fluorescence, and stimulated fluorescence by polaritons in thin anthracene crystals. Reinterpretation of spectroscopic properties of anthracene. Chem. Phys. Lett., 1975. 36(Copyright (C) 2012 American Chemical Society (ACS). All Rights Reserved.): p. 316-21.
5. Katoh, R. and M. Kotani, Fluorescence from the second excited state of an anthracene crystal observed by two-step excitation. Chem. Phys. Lett., 1999. 300(Copyright (C) 2012 American Chemical Society (ACS). All Rights Reserved.): p. 734-738.
6. Hemmi, N., Z.A. Dreger, and Y.M. Gupta, Time-resolved electronic spectroscopy to examine shock-wave-induced changes in anthracene single crystals. J. Phys. Chem. C, 2008. 112(Copyright (C) 2012 American Chemical Society (ACS). All Rights Reserved.): p. 7761-7766.
7. Ahn, T.S., et al., Experimental and theoretical study of temperature dependent exciton delocalization and relaxation in anthracene thin films. J. Chem. Phys., 2008. 128: p. 054505/1-054505/11.
8. Oehzelt, M., et al., The crystal structure of anthracene up to 22 GPa: A X-ray diffraction study. Mater. Res. Soc. Symp. Proc., 2003. 771(Copyright (C) 2012 American Chemical Society (ACS). All Rights Reserved.): p. 219-224.
9. Spano, F.C., The spectral signatures of Frenkel polarons in H- and J-aggregates. Acc. Chem. Res., 2010. 43: p. 429-439.
10. Garnier, F., et al., Molecular engineering of organic semiconductors: design of self-assembly properties in conjugated thiophene oligomers. Journal of the American Chemical Society, 1993. 115(19): p. 8716-8721.
11. Julian, M.M. and F.D. Bloss, Optical measurements of anthracene. Acta Crystallogr., Sect. A, 1982. A38(Copyright (C) 2012 American Chemical Society (ACS). All Rights Reserved.): p. 167-9.

Chapter 5 Pressure Effects on the Photoisomerization of 9-tert-Butylanthracene

5.1 Introduction

Certain organic molecules undergo bond breaking and formation when subjected to mechanical force. This phenomenon has attracted large research interest in recent years. These molecules may strengthen under stress and strain or signal via light or color change as they are nearly failing. Some anthracene derivatives have shown interesting photomechanical properties[1-2]. Previous work shows that certain anthracene derivatives will undergo reversion of the anthracene [4+4] photoisomerization reaction via pressure-catalyzed bond breaking [3]. In contrast to the routine of using ultrasound to apply pressure, this research uses a more direct approach to apply force to avoid the thermal effects associated with ultrasound techniques[4] . The device used for applying pressure in this experiment is called a diamond anvil cell (DAC)[5], and is diagrammed in **Figure 5-1**. The absorption intensity change was tracked over to investigate the reversible conversion process of bi(anthracene-9,10-dimethylene) (BA) to its photodimer (PI). In my project, 9-tert-butylanthracene (TBA) was chosen as a target molecule as it has been shown to undergo thermally reversible photoisomerization UV irradiation (see **Figure 5-2)**. Whether the reverse reaction can be catalyzed by high pressure is an open question. In my project, a new method was applied: I was tracking the fluorescence intensity change to study the TBA →Dewar photoisomerization along with its reverse reaction. It is our earlier assumption that the reverse reaction is pressure-activated.

Therefore, the reverse reaction rate should be enhanced at increasingly higher pressures. Experimentally, we see the opposite of this.

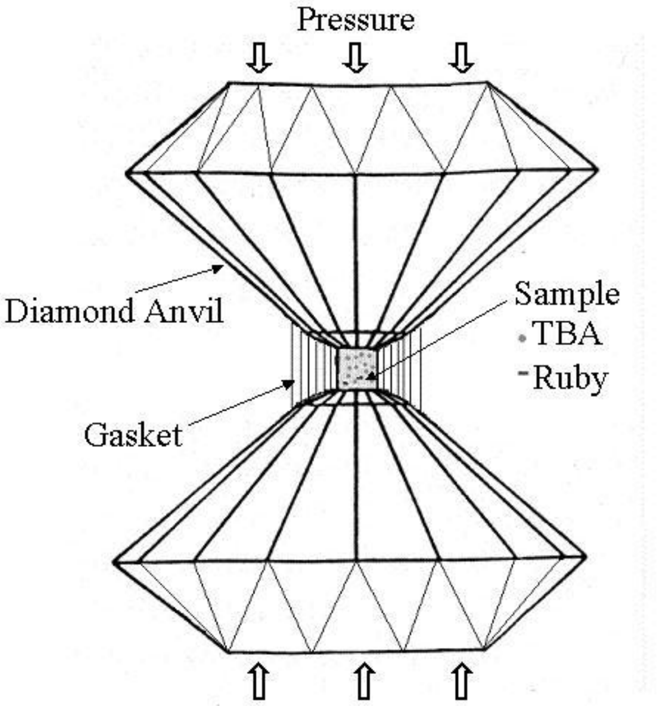

Figure 5-1 The principle of a diamond anvil cell (DAC)

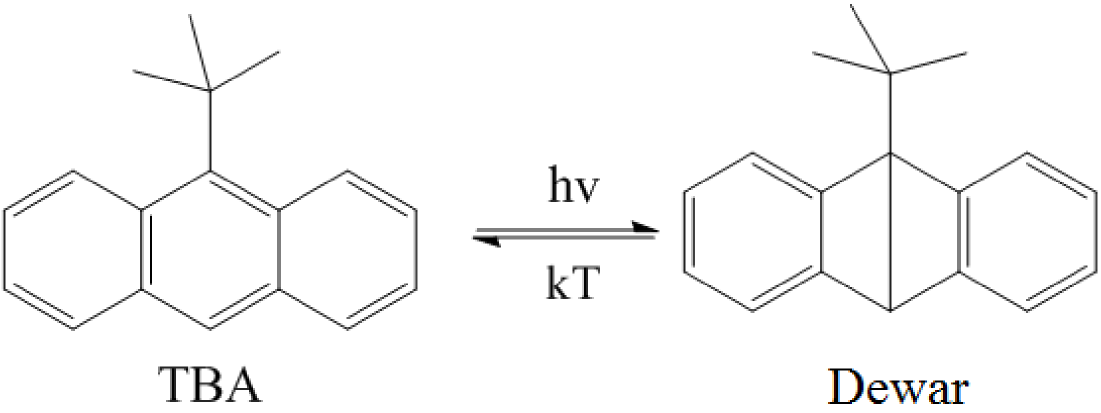

Figure 5-2 Photoisomerization of 9-tert-butylanthracene (TBA)

5.2 Experimental

The crystalline 9-tert-butylanthracene (TBA) was synthesized and purified by Dr. Rabih Al-Kaysi. Polystyrene (PS, average Mw~280,000 by GPC, Tg=100 °C, Sigma-Aldrich) and UV-transparent (>237 nm) and polycycloolefin resin (ZEONEX Z480, Tg=138 °C –140 °C, Zeon Chemical L.P.) were purchased commercially and used without further purification. The TBA solutions for fluorescence lifetime measurement were prepared via directly dissolving TBA into cyclohexane/toluene to create solutions possessing a concentration range of 10^{-4}~10^{-5} mol/L. The solutions were degassed for 2 min with argon just before taking measurements. Crystalline TBA was mixed with PS in Toluene and Zeonex in cyclohexane. The mixture was mechanically stirred for ~ 24 hours, drop-casted on a pre-cleaned glass slide and evaporated while sealed in the dark at room temperature. Transparent yellowish films of TBA doped polymer films were obtained (~0.2 mm thick, ~10^{-4} mol/L TBA by molarity for fluorescence measurements) and used in photo-bleaching and recovery investigations. The stock solutions were ultrasonicated in the dark for a half hour before reusing to make drop-cast films.

Steady-state luminescence excitation and emission were measured with a Spex Fluorolog Tau-3 fluorescence spectrophotometer with a excitation wavelength at 365 nm and a emission wavelength at 500 nm, respectively.

Fluorescence lifetime measurements were performed with the same excitation and detection set-up as described in Chapter 2, except the excitation pulses were centered at 400 nm. The 800 nm pulses derived from a 40 kHz regeneratively amplified Ti:sapphire laser system were frequency doubled to produce 400 nm light. The solution samples were placed in a 1 cm path length quartz cuvette, while the solid samples at ambient pressure were located inside a Janis ST-100 with an active vacuum to exclude oxygen. The samples at higher pressure were set in the gasket of a DAC together with some ruby dust that tells the pressure values by its luminescence emission[6].

UV-vis absorption spectra were obtained using a light source (Analytical Instrument Systems Model DT 100) and an Ocean Optics SD2000 detector system. A mercury lamp with output centered at 365 nm was used as a light source for triggering the TBA→Dewar photoisomerization.

The fluorescence signal detection system for photoconversion and reversion reactions includes a lock-in system together with a 405 nm blue/violet laser, as shown in **Figure 5-3**. The laser source was soldered to a power supply with a constant output of 3.00 volt. The laser beam was chopped after passing the first neutral density (ND) filter and then went through a tilted microslide that allows some light scattering into a photodiode detector (ThorLabs DET110, high speed Si photo detector, 20ns rise time). The photodiode detector was connected with Lock-in amplifier #1 (Model SR830 DSP, Stanford Research Systems) that also received the signals from the chopper as a reference. After that, the laser beam was reflected by a mirror and split via a 420 nm dichroic mirror. The incident light was focused onto the sample using a 10 cm focus lens that was placed in between the sample and detector at 10 cm from the sample and 10 cm from the detector. The fluorescence signal was collected by a photomultiplier tube (PMT) after passing a 450 nm bandpass filter (center wavelength = 450.0 ± 10 nm, bandwidth = 40.0 ± 8 nm, Andover Corp.) and a 450 nm longpass filter (LWP, 50% wavelength 450.0 ± 10 nm, Andover Corp.) to exclude any laser scattering left. The signals from the PMT were inputted into the Lock-in amplifier #2 (Model SR830 DSP, Stanford Research Systems) together with the chopper signal as a reference.

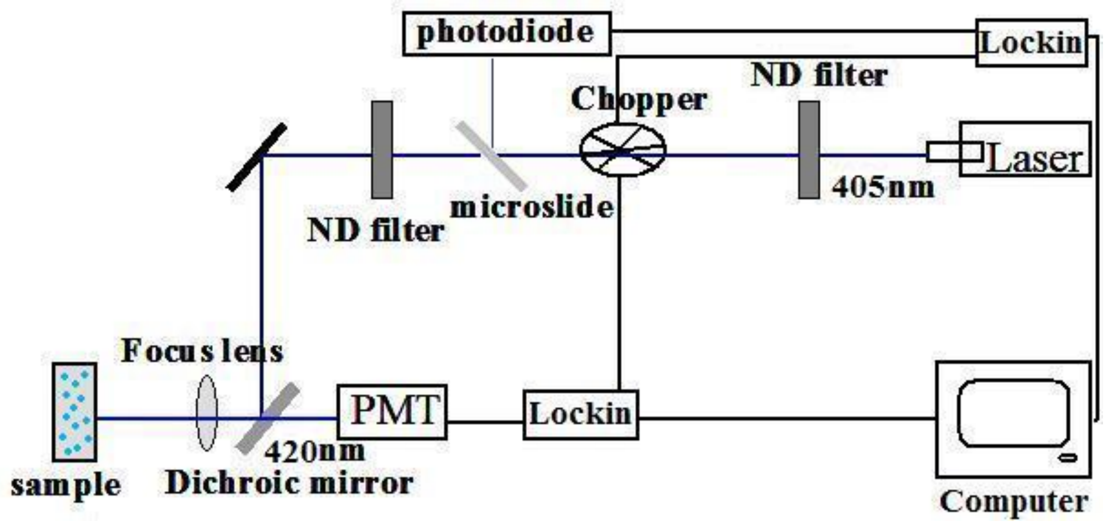

Figure 5-3 the lock-in laser set-up for TBA photo-bleaching and fluorescence recovery

5.3 Measurements of Fluorescence/Absorption Recovery

Figure 5-4 shows the normalized steady-state luminescence excitation and emission spectra of a TBA (~10^{-3} M) doped PS film, with results corresponding well with the previous research[7-9].

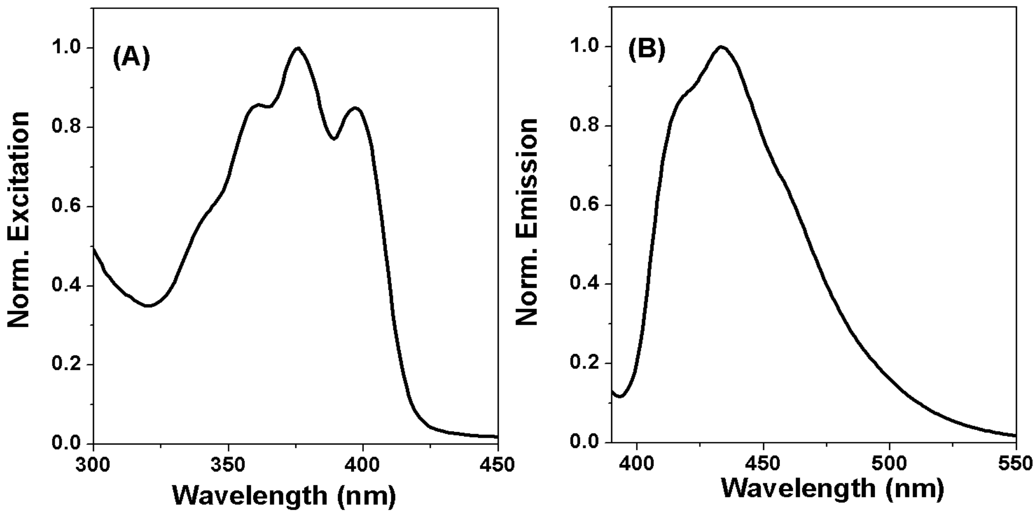

Figure 5-4 Steady-state luminescence excitation (A) and emission (B) spectra of TBA in PS

A direct way to investigate the TBA →Dewar photoisomerization and the reverse reaction is to measure the absorption change with time. The absorption band intensity should be directly proportional to the concentration of the unreacted TBA. Let us assume N_0 is the concentration of TBA before photoisomerization, N_i is the irreversibly photobleached TBA, and N_a and N_d are the time-resolved TBA and Dewar concentrations respectively. The number in the bracket is the time (in the unit of min) after irradiation (see **Equation 5-1**) .

$$N_0 = N_a(0) + N_d(0) + N_i$$ **Equation 5-1**

Both the photoisomerization of the TBA and the reverse reaction should be first-order reactions. The rate coefficient of the photoisomerization is K_{ad} and that of the reverse reaction is K_{da}. During TBA recovery process, Dewar concentration change can be expressed via **Equation 5-2** and **Equation 5-3**.

$$\frac{dN_d}{dt} = -K_{da}N_d$$ **Equation 5-2**

$$N_d(t) = N_d(0)e^{-K_{da}t}$$ **Equation 5-3**

The TBA concentration change can be described as **Equation 5-4** and **Equation 5-5,** where C is a constant.

$$\frac{dN_a}{dt} = K_{da}N_d = K_{da}N_d(0)e^{-K_{da}t}$$ **Equation 5-4**

$$N_a(t) = \frac{K_{da}N_d(0)}{-K_{da}}e^{-K_{da}t} + C = -N_d(0)\,e^{-K_{da}t} + C$$ **Equation 5-5**

When t = 0 min after irradiation, it is easy to use **Equation 5-1** and **Equation 5-5** to derive an expression for C.

$$N_a(0) = -N_d(0) + C = N_0 - N_d(0) - N_i$$ **Equation 5-6**

$$C = N_0 - N_i \qquad \textbf{Equation 5-7}$$

$$N_a(t) = - N_d(0)e^{-K_{da}t} + N_0 - N_i \qquad \textbf{Equation 5-8}$$

The absorption intensity A_0 is directly proportional to N_0 and A(t) is proportional to $N_a(t)$. If the lamp intensity is not so strong that it causes any irreversible photobleaching (N_i=0), the absorption peak intensity at ~377 nm originally is A_0 and A(t) is the absorption at 377 nm at t min after irradiation: A_0- A(t) should be proportional to N_0-$N_a(t)$

$$N_0 - N_a(t) = N_d(0)\ e^{-K_{da}t} \qquad \textbf{Equation 5-9}$$

A TBA doped PS film(~10^{-3} M) and a TBA doped Zeonex film (~10^{-3} M) were prepared for the experiment. Their absorption spectra were recorded before and after irradiation, as show in **Figure 5-5**. **Figure 5-6** shows the absorption recovery over time of the TBA doped PS film. The original peak absorption of TBA A(t) versus time (t, in the unit of min) was plotted in **Figure 5-6 (A)**. The TBA →Dewar reaction was proved to be first-order: when I plotted ln[A_0- A(t)] versus time (see **Figure 5-6(B)**), it gave me a good linear fit with a slope value equal to -2.58*10^{-3} min^{-1} that should correspond to the TBA recovery rate -K_{da}. The same data process method was performed for theTBA doped Zeonex film in **Figure 5-7**. The slope value of the linear fit for ln[A_0-A_t] with time is -3.36*10^{-3} min^{-1}.

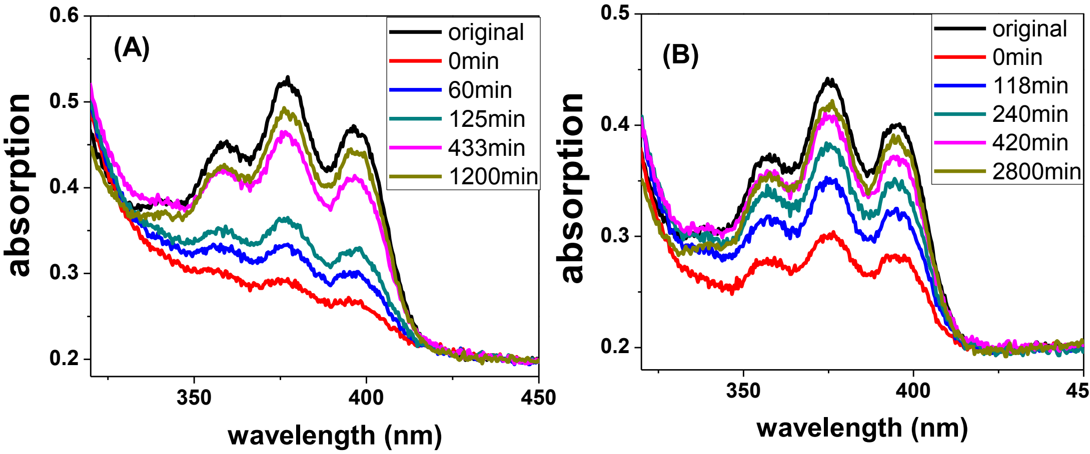

Figure 5-5 Absorption spectra of TBA in PS (A) and Zeonex (B) matrix before (original) and after photoisomerization (t min after irradiation)

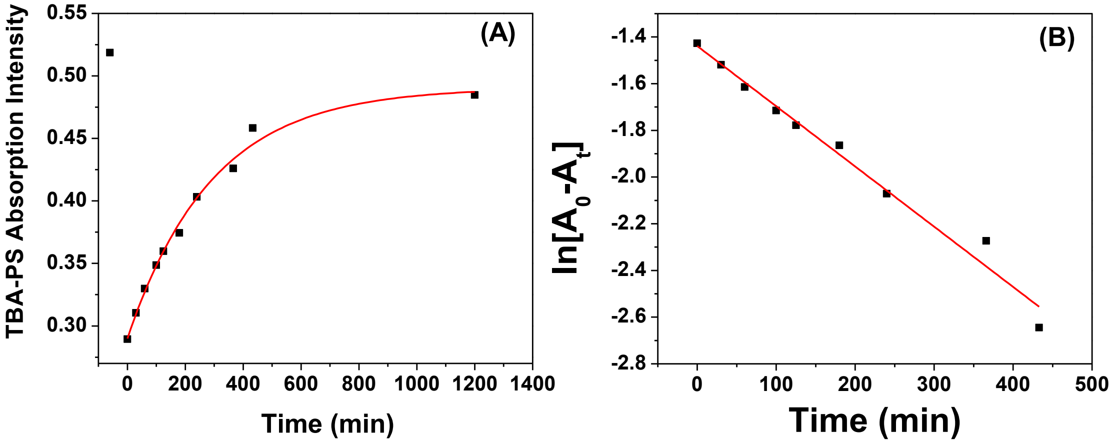

Figure 5-6 The absorption change of a TBA doped PS film during the photoreaction and recovery: (A) the absorption intensity at 377 nm over time (B) the plot of ln[A_0-A_t] over time

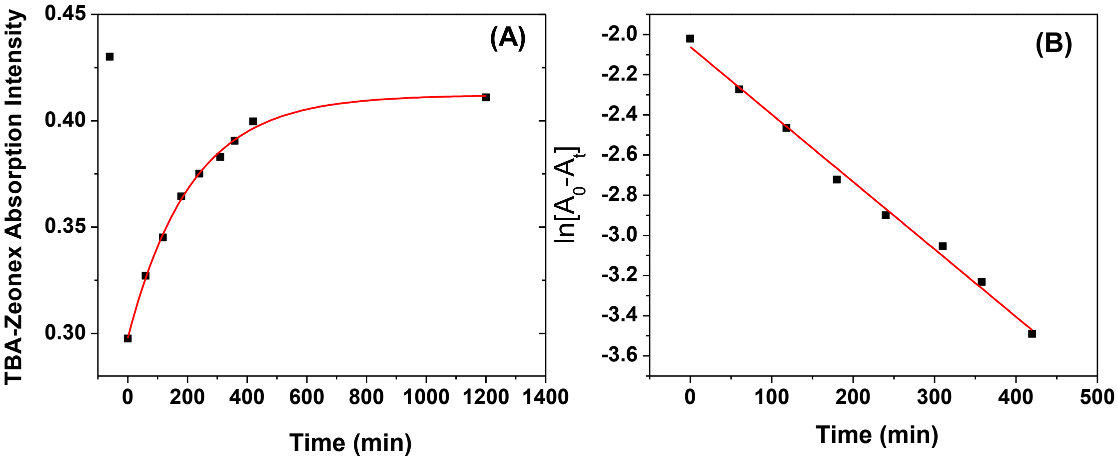

Figure 5-7 The absorption change of a TBA doped Zeonex film during the photoreaction and recovery: (A) the absorption intensity at 377 nm over time (B) the plot of ln[A_0-A_t] over time

The TBA photoisomerization and recovery was investigated by tracking its fluorescence intensity using the laser set-up in **Figure 5-3**. The laser intensities for initializing photoisomerization and detecting emission were 10 μW and 1.0 μW, respectively. The original fluorescence intensity before irradiation was designated as F_0; the fluorescence intensity immediately after irradiation is designated as F_{min}, with subsequent intensities for all other times after excitation designated as F_t. A plot of ln[(F_0- F_t)/F_{min}] versus time was used to assess photobleaching of the target molecules. The linear fits yield a slope value of –3.72 x 10^{-3} min^{-1} for a TBA doped PS film (see **Figure 5-8** (B)) and -3.34 x 10^{-3} min^{-1} for a TBA doped Zeonex film (see **Figure 5-9** (B)). Since the TBA doped PS experienced a faster fluorescence recovery after being photobleached, I chose this system for further research. Ideally, the fluorescence emission recovery rate should correspond to the absorption recovery rate. However, the absorption and fluorescence recovery rates of my TBA doped PS samples have a considerable error between the two values.

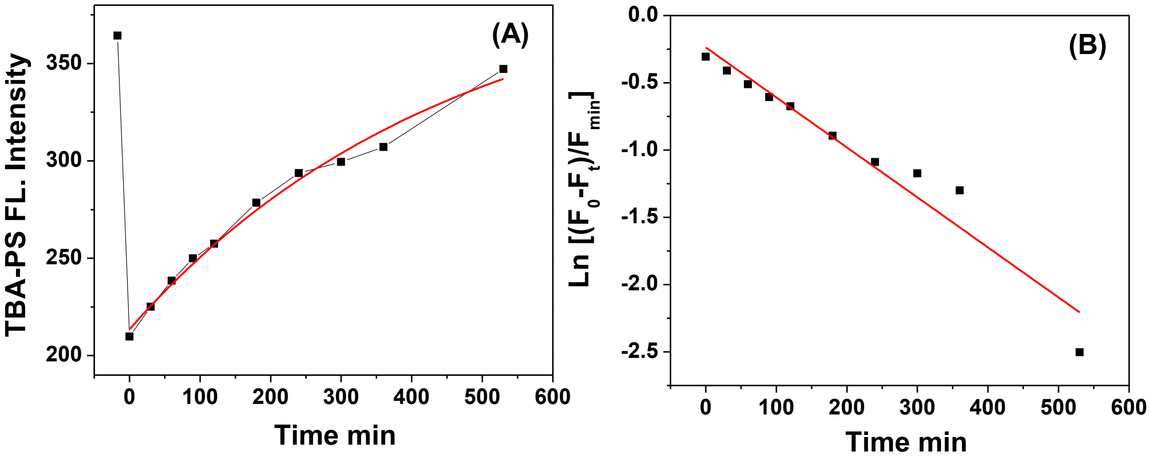

Figure 5-8 The fluorescence intensity change of a TBA doped PS film during the photoreaction and recovery: (A) the fluorescence intensity over time (B) the plot of ln[(F_0- F_t)/F_{min}] over time

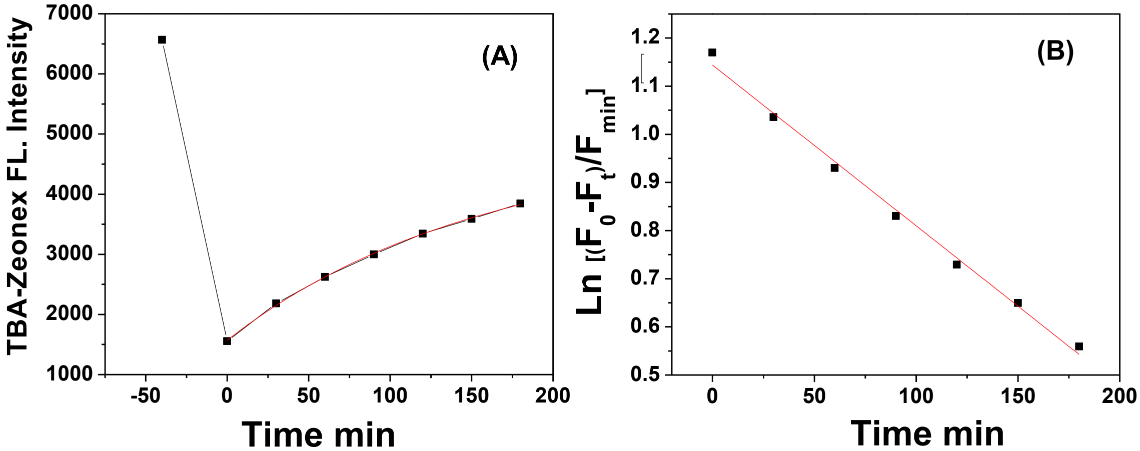

Figure 5-9 The fluorescence intensity change of a TBA doped Zeonex film during the photoreaction and recovery: (A) the fluorescence intensity over time (B) the plot of ln[(F_0- F_t)/F_{min}] over time

5.4 Pressure-dependent Fluorescence Lifetime

The fluorescence lifetimes of TBA in degassed cyclohexane and toluene are both ~ 0.27 ns. Double-exponential decay curves were obtained for TBA doped PS films. The lifetimes of the short-lived (τ_1) and long-lived (τ_2) components, along with the ratio of A_2 to A_1 for these films taken at different pressures are summarized in **Table 5-1**. In previous studies, the quantum yield of TBA in liquid solutions and a polymer matrix (PMMA) were reported to be ~0.01[7, 10] and ~0.4[11], respectively. Quantum yields related directly to the reaction rate coefficient K, as shown in **Equation 5-10,** in which I is the light intensity and σ is the absorption cross section. K is also inversely proportional to the fluorescence lifetime. Therefore, the fluorescence lifetimes (τ_2) in solution and the polymer matrix are reasonable. Though the fluorescence lifetimes do not show a clear trend with pressure, the ratio between the two components A_2 and A_1 has an apparent decreasing trend with increasing pressures. The previous research had several assumptions but did not give out a rational explanation for the origin of these two components[11]. When the weighted mean lifetime τ was calculated according to **Equation 5-11**, and plotted with pressure as shown in **Figure 5-11**. It seems that τ increases with pressure within 20 kbar, but then decreases at higher pressures.

$$K=\sigma * I * \varphi$$ **Equation 5-10**

$$<\tau> = \frac{A_1\tau_1+A_2\tau_2}{A_1+A_2}$$ **Equation 5-11**

Table 5-1 Summary of luminescence decay parameters for TBA doped PS films

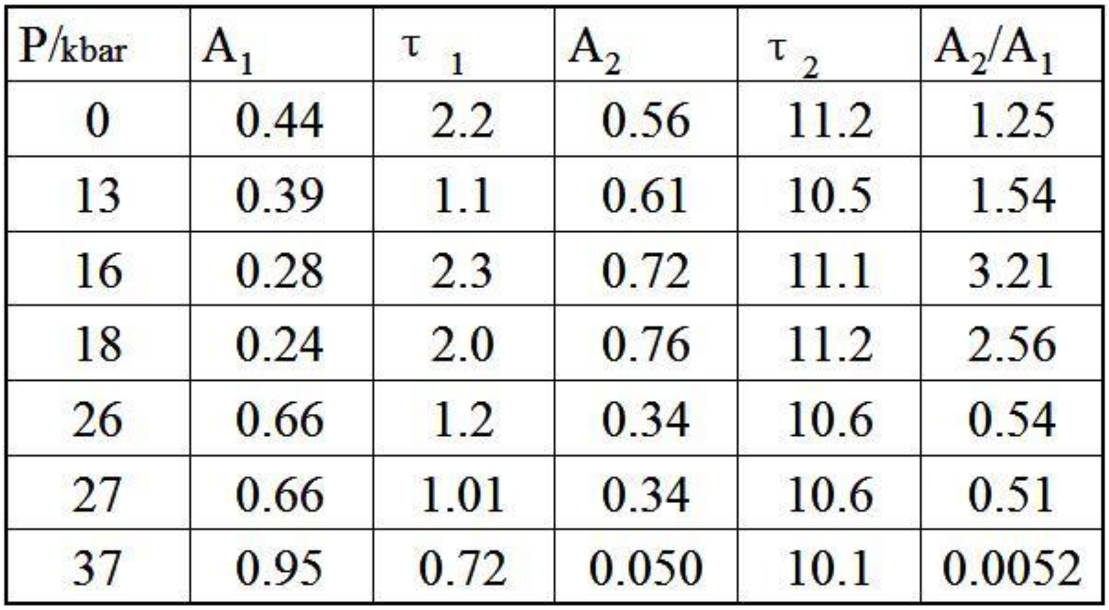

P/kbar	A_1	τ_1	A_2	τ_2	A_2/A_1
0	0.44	2.2	0.56	11.2	1.25
13	0.39	1.1	0.61	10.5	1.54
16	0.28	2.3	0.72	11.1	3.21
18	0.24	2.0	0.76	11.2	2.56
26	0.66	1.2	0.34	10.6	0.54
27	0.66	1.01	0.34	10.6	0.51
37	0.95	0.72	0.050	10.1	0.0052

When directly comparing their fluorescence decays within the 10 ns and 50 ns time windows, decay rates become faster when the pressure is higher than 25 kbar as shown in **Figure 5-10**.

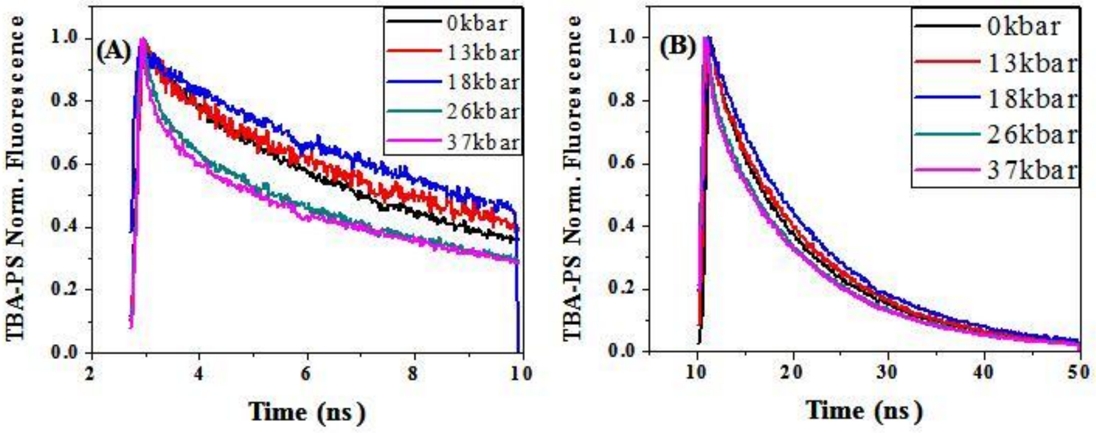

Figure 5-10 Fluorescence decays of TBA doped PS films under various pressure at 10 ns (A) and 50 ns (B) windows

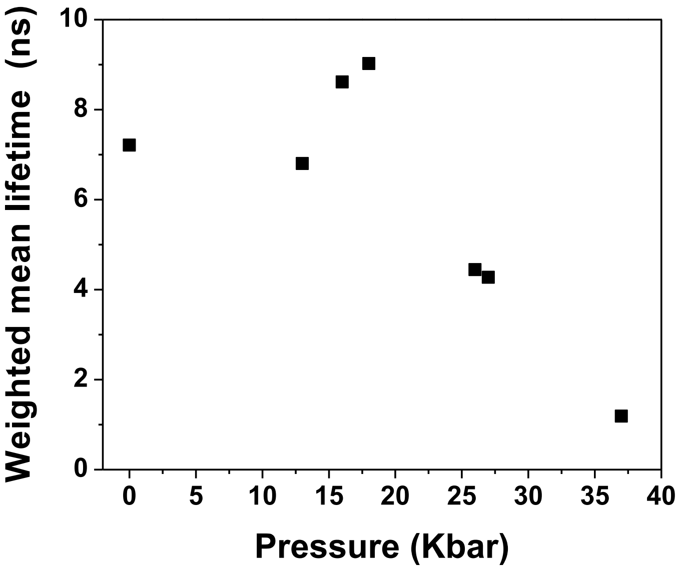

Figure 5-11 Weighted mean fluorescence lifetime of TBA doped PS films under different pressures

5.5 High Pressure Effects on TBA Photoisomerization and Reversion

When the photoisomerization of TBA →Dewar was investigated under different pressures through the use of time-resolved fluorescence using the laser set-up in **Figure 5-3** with excitation centered at 450 nm. TBA photoisomerization slowed down with increasing pressure, as shown in **Figure 5-12**. The TBA photoisomerization rate is faster in the cryostat than in the DAC at ambient pressures since the diamonds scatter some incident light, reducing the light intensity. However, compared to the previous research[12], the TBA photoisomerization rate is significantly faster, which may be due to the higher intensity of the irradiating light.

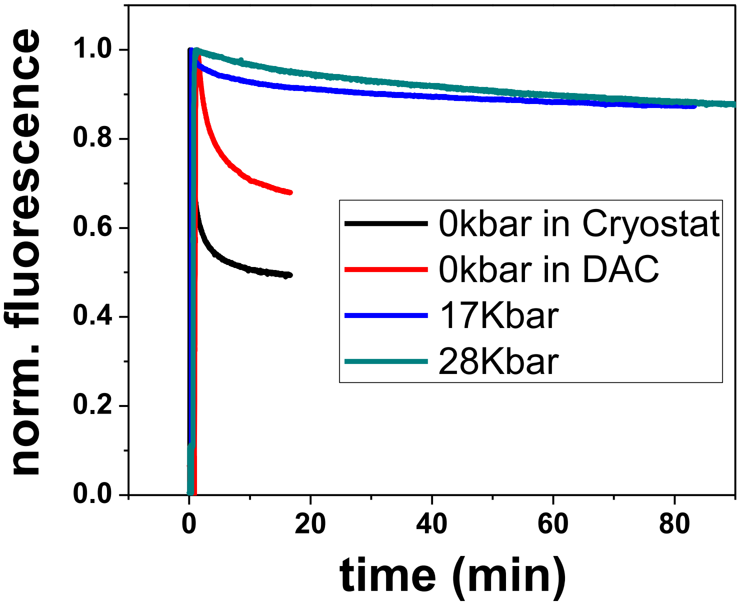

Figure 5-12 Photoisomerization kinetics of TBA doped PS in cryostat (black) and in DAC under different pressures: 0 kbar(red), 17 kbar (blue) and 28 kbar (dark cyan) on irradiation with 405 nm light

For the reverse reaction Dewar→TBA under high pressures, the data of fluorescence recovery was processed using the same method described early in this chapter so that they can be fairly compared with the data under ambient pressure (see **Figure 5-8**). When the linear fit was done for $\ln[(F_0 - F_t)/F_{min}]$ versus time, the slope values were determined to be -2.39×10^{-3} min^{-1} for the sample under 17 kbar (see **Figure 5-13**) and -4.11×10^{-4} min^{-1} for the sample under 28 kbar (see **Figure 5-14**). Compared to the slope of -3.72×10^{-3} min^{-1} measured at ambient pressure, it can be concluded that the relative Dewar→TBA reaction rates are as follows: ambient pressure > 17 kbar > 28 kbar as shown in **Figure 5-15(A)**. This order makes sense when the molecular structures of TBA and its Dewar were clarified. According to the previous X-ray crystallography study[13], both TBA and its Dewar molecules are not planar: the fold angle of the former is 166.2° and that of the later is 113°. Therefore, high pressure makes contortion of these two molecules more difficult. Both the photoisomerization and reverse reaction rates slow down with increasing pressure, which also suggests the molecular volume of the intermediate may be larger than that of both TBA and the Dewar. An estimation of the activation volume can be done with the plot in **Figure 5-15 (B).**

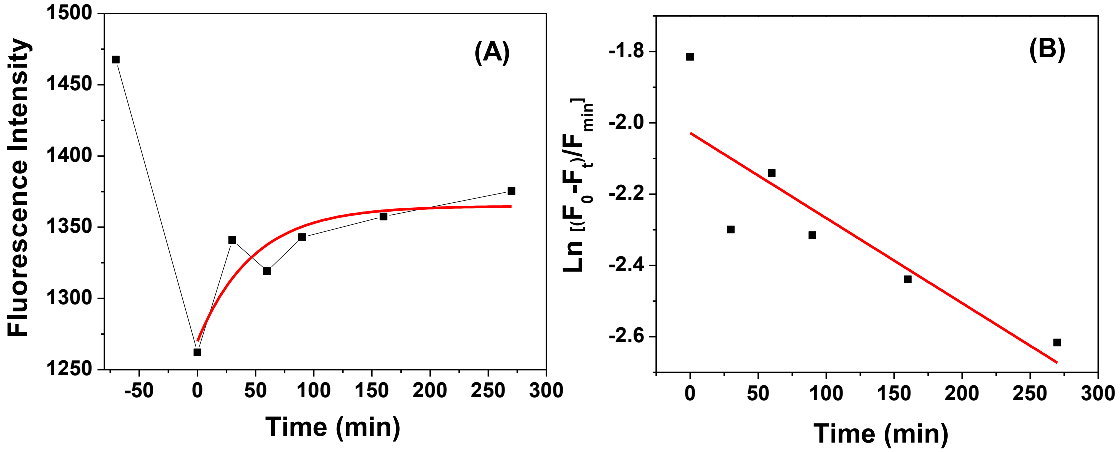

Figure 5-13 The fluorescence recovery kinetics of a TBA doped PS film in DAC under 17 kbar: (A) the fluorescence intensity over time (B) the plot of $\ln[(F_0-F_t)/F_{min}]$ over time

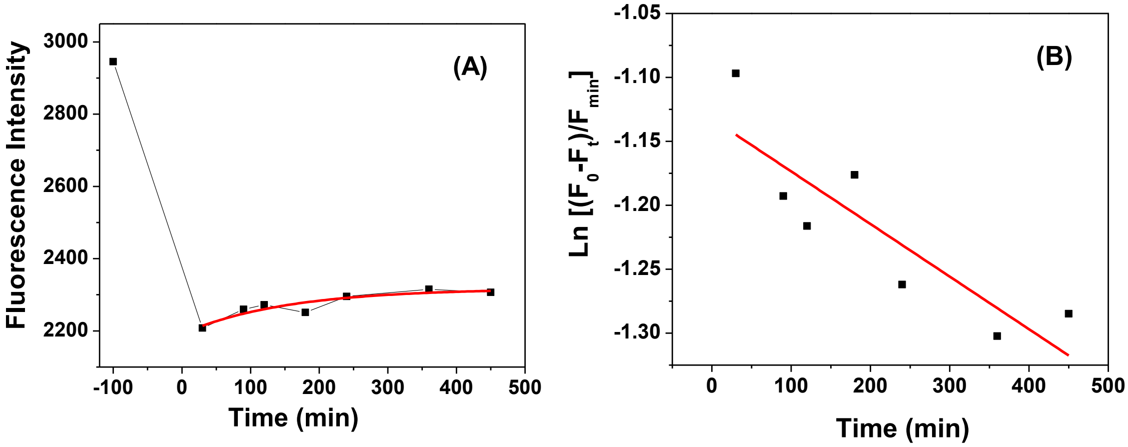

Figure 5-14 The fluorescence recovery kinetics of a TBA doped PS film in DAC under 28 kbar: (A) the fluorescence intensity over time (B) the plot of ln[(F_0-F_t)/F_{min}] over time

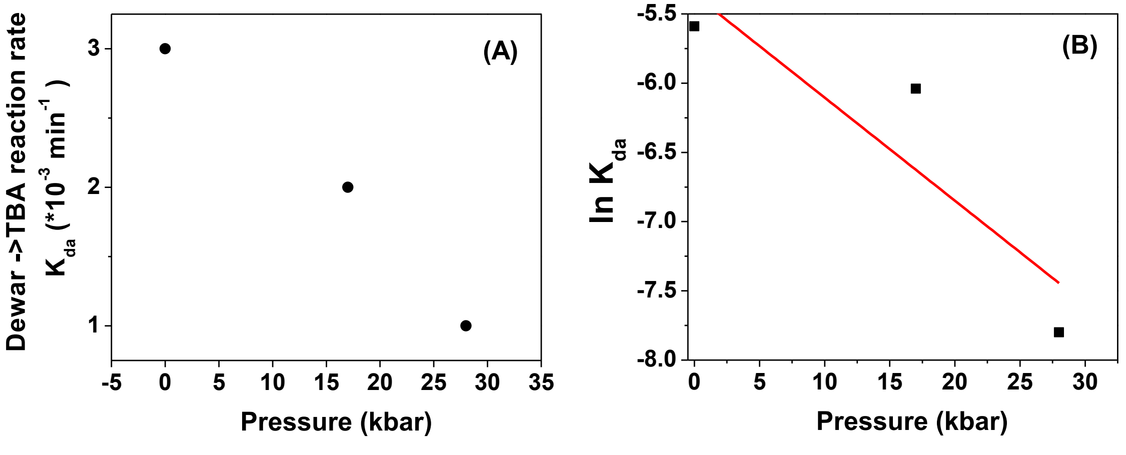

Figure 5-15 (A) Pressure-dependent reaction rate of Dewar ->TBA (B)Linear dependence of the log of the rate constant K_{da} vs pressure

5.6 Conclusion

My preliminary results indicate that TBA ←→Dewar photoisomerization and reverse reactions in polystyrene matrix are pressure sensitive. Both the forward and reverse reaction rates slow down with increasing pressure. High pressure impedes the generation of both TBA and its Dewar. The larger molecular volume of the intermediate may explain the result. Another main problem that need further clarification is that fluorescence lifetimes of TBA did not correspond well with the pressure change. More experiments and theoretic calculation have to be done to give a solid explanation.

Reference:

1. Zhu, L., R.O. Al-Kaysi, and C.J. Bardeen, *Reversible Photoinduced Twisting of Molecular Crystal Microribbons.* Journal of the American Chemical Society, 2011. **133**(32): p. 12569-12575.
2. Al-Kaysi, R.O. and C.J. Bardeen, *Reversible Photoinduced Shape Changes of Crystalline Organic Nanorods.* Advanced Materials, 2007. **19**(9): p. 1276-1280.
3. Jezowski, S.R., et al., *Pressure Catalyzed Bond Dissociation in an Anthracene Cyclophane Photodimer.* Journal of the American Chemical Society, 2012. **134**(17): p. 7459-7466.
4. Groote, R., R.T.M. Jakobs, and R.P. Sijbesma, *Performance of Mechanochemically Activated Catalysts Is Enhanced by Suppression of the Thermal Effects of Ultrasound.* ACS Macro Lett., 2012. **1**(Copyright (C) 2012 American Chemical Society (ACS). All Rights Reserved.): p. 1012-1015.
5. C. E. Weir, et al., *Infrared Studies in the 1- to 15-Micron Region to 30,000 Atmospheres.* J. Res. Natl. Bur. Stand., 1959. **63A**: p. 55-62.
6. Forman, R.A., et al., *Pressure measurement made by the utilization of ruby sharp-line luminescence.* Science, 1972. **176**(Copyright (C) 2012 U.S. National Library of Medicine.): p. 284-5.
7. Dreeskamp, H., B. Jahn, and J. Pabst, *Thermoreversible photo valence isomerization of 9-tert-butylanthracene to its 9,10-Dewar-Isomer.* Z. Naturforsch., A, 1981. **36A**(Copyright (C) 2012 American Chemical Society (ACS). All Rights Reserved.): p. 665-8.
8. Dutta, A.K. and T.N. Misra, *Fluorescence study of 9, 10 diphenyl anthracene in mixed Langmuir-Blodgett films with stearic acid.* Optical Materials, 1994. **3**(1): p. 35-40.

9. Meador, M.A. and H. Hart, *Substituent effects on the photoisomerization of anthracenes to their 9,10-Dewar isomers.* The Journal of Organic Chemistry, 1989. **54**(10): p. 2336-2341.
10. Schoof, S.G., H.; von Sonntag, C. , *Fluoreszenz und Fluoreszenzloeschung von meso-substituierten Anthracenderivaten in Loesung.* . Ber. Bunsenges. Phys. Chem. , 1978. **82**(10): p. 1068-73.
11. Hirayama, S. and Y. Shimono, *Temperature and viscosity effects on fluorescence in 9-t-butylanthracene.* Journal of the Chemical Society, Faraday Transactions 2: Molecular and Chemical Physics, 1984. **80**(8): p. 941-955.
12. Minaylov, V.V., V.S. Gurman, and A.K. Vorobiev, *Photoisomerization of 9-tert-butylanthracene in polystyrene films under photoselection conditions. Consideration of molecular thermal rotation.* J. Photochem. Photobiol., A, 1995. **87**(Copyright (C) 2012 American Chemical Society (ACS). All Rights Reserved.): p. 67-73.
13. Angermund, K., et al., *High-Resolution X-ray Crystallography—An Experimental Method for the Description of Chemical Bonds.* Angewandte Chemie International Edition in English, 1985. **24**(4): p. 237-247.

Chapter 6 Conclusions and Future Directions

We generated the idea of affixing alkoxy side groups to anthracene molecules, assuming that the crystal packing and exciton structures of these compounds in the solid state could be modified while the spectroscopic properties of the individual molecules themselves remain constant. However, both the experimental results and the theoretical calculations show that the photophysical properties of 2,6 dialkoxyanthracenes are quite different from unsubstituted anthracene. In the dialkoxyanthracenes, the oscillator strength appears to be redistributed between the La and Lb states, the orientation of the transition dipole moment is tilted by ~30°, and all 2,6 dialkoxyanthracene molecules demonstrated a time-dependent reshaping of the fluorescence spectrum due to the intramolecular conformational change in the excited state. The oxygen atoms within the alkoxy groups are the main source for the changes that occur between anthracene and 2,6 dialkoxyanthracenes. This project is thus complicated by the fact that electrons from the oxygen atom participate in the conjugated system of anthracene. Similar studies into 2,6 dialkylanthracenes therefore seem more promising as target molecules in future research. However, the organic synthesis and purification of such compounds will be more challenging.

Among the 2,6 dialkoxyanthracenes (**C1-C6**), only the **C1** single crystal demonstrated the two typical spectroscopic properties of J-type aggregates – a superradiant emission and an enhancement of the 0-0 vibronic peak intensity with decreasing temperature. It will be an interesting research to compare unsubstituted anthracene with **C1**. A combination of experimental spectroscopy, theoretical calculation, and detailed analysis can quantify the exciton properties of **C1** such as the coherence volume.

We also asked the question whether or not the application of pressures could accelerate the reverse reaction of 9-tert-butylanthracene (TBA) photoisomerization. According to our preliminary results, the answer is no. However, the idea of measuring the reaction kinetics via tracing luminescence intensities of the fluorescent mechanophores is promising and can be applied with our laser set-up to investigate other potential pressure-sensor molecules.

Appendix A: X-Ray Structure Determination of C1 Single Crystal

A light yellow prism fragment (0.42 x 0.37 x 0.17 mm^3) was used for the single crystal x-ray diffraction study of $C_{16}H_{14}O_2$. The crystal was coated with paratone oil and mounted on to a cryo-loop glass fiber. X-ray intensity data were collected at 100(2) K on a Bruker APEX2[31] platform-CCD x-ray diffractometer system (fine focus Mo-radiation, λ = 0.71073 Å, 50KV/30mA power). The CCD detector was placed at a distance of 4.9890 cm from the crystal.

A total of 2400 frames were collected for a hemisphere of reflections (with scan width of 0.3^o in ω, starting ω and 2θ angles at –30^o, and ϕ angles of 0^o, 90^o, 180^o, and 270^o for every 600 frames, 10 sec/frame exposure time). The frames were integrated using the Bruker SAINT software package[32] and using a narrow-frame integration algorithm. Based on a monoclinic crystal system, the integrated frames yielded a total of 8376 reflections at a maximum 2θ angle of 59.14^o (0.72 Å resolution), of which 1636 were independent reflections (R_{int} = 0.0190, R_{sig} = 0.0121, redundancy = 5.1, completeness = 99.9%) and 1521 (93.0%) reflections were greater than $2\sigma(I)$. The unit cell parameters were, **a** = 11.6342(5) Å, **b** = 6.2315(3) Å, **c** = 8.1837(3) Å, $\boldsymbol{\beta}$ = 102.2834(5)^o**,** V = 579.72(4) Å^3, Z = 2, calculated density D_c = 1.365 g/cm^3. Absorption corrections were applied (absorption coefficient μ = 0.089 mm^{-1}; max/min transmission = 0.9853/0.9634) to the raw intensity data using the SADABS program[33].

The Bruker SHELXTL software package[34] was used for phase determination and structure refinement. The distribution of intensities (E^2-1 = 1.059) and systematic absent reflections indicated one possible space group, P2(1)/c. The space group P2(1)/c (#14) was later determined to be correct. Direct methods of phase determination followed by two Fourier cycles of refinement led to an electron density map from which most of the non-hydrogen atoms were identified in the asymmetry unit of the unit cell. With subsequent isotropic refinement, all of the non-hydrogen atoms were identified. There was half a molecule of $C_{16}H_{14}O_2$ present in the asymmetry unit of the unit cell. The molecule was located on an inversion center.

Atomic coordinates, isotropic and anisotropic displacement parameters of all the non-hydrogen atoms were refined by means of a full matrix least-squares procedure on F^2. The H-atoms were included in the refinement in calculated positions riding on the atoms to which they were attached. The refinement converged at R1 = 0.0376, wR2 = 0.1146, with intensity $I>2\sigma(I)$. The largest peak/hole in the final difference map was 0.460/-0.216 e/Å^3.

Table 1 Crystal data and structure refinement for C1.

Empirical formula	C16 H14 O2
Formula weight	238.27
Temperature	100(2) K
Wavelength	0.71073 Å
Crystal system	Monoclinic
Space group	P2(1)/c (#14)

(to be continued)

Unit cell dimensions	a = 11.6342(5) Å	α= 90°.
	b = 6.2315(3) Å	β= 102.2834(5)°.
	c = 8.1837(3) Å	γ = 90°.
Volume	579.72(4) Å^3	
Z	2	
Density (calculated)	1.365 Mg/m^3	
Absorption coefficient	0.089 mm^{-1}	
F(000)	252	
Crystal size	0.42 x 0.37 x 0.17 mm^3	
Theta range for data collection	3.58 to 29.57°.	
Index ranges	-16<=h<=16, -8<=k<=8, -11<=l<=11	
Reflections collected	8376	
Independent reflections	1636 [R(int) = 0.0190]	
Completeness to theta = 29.57°	99.9 %	
Absorption correction	Semi-empirical from equivalents	
Max. and min. transmission	0.9853 and 0.9634	
Refinement method	Full-matrix least-squares on F^2	
Data / restraints / parameters	1636 / 0 / 84	
Goodness-of-fit on F^2	1.106	
Final R indices [I>2sigma(I)]	R1 = 0.0376, wR2 = 0.1146	
R indices (all data)	R1 = 0.0396, wR2 = 0.1174	
Extinction coefficient	0.024(8)	
Largest diff. peak and hole	0.460 and -0.216 e.Å^{-3}	

Table 2 Atomic coordinates (x 10^4) and equivalent isotropic displacement parameters (Å^{2}x 10^3) for C1. U(eq) is defined as one third of the trace of the orthogonalized U^{ij} tensor.

	x	y	z	U(eq)
O(1)	3952(1)	718(1)	8393(1)	18(1)
C(9A)	1112(1)	765(1)	9785(1)	12(1)
C(4A)	692(1)	-1323(1)	9204(1)	12(1)
C(1)	2234(1)	1488(1)	9552(1)	14(1)
C(9)	400(1)	2048(1)	10570(1)	12(1)
C(2)	2884(1)	204(1)	8732(1)	14(1)
C(4)	1414(1)	-2607(1)	8378(1)	14(1)
C(3)	2464(1)	-1864(1)	8132(1)	16(1)
C(11)	4433(1)	2748(2)	8986(1)	21(1)

Table 3 Bond lengths [Å] and angles [°] for C1

O(1)-C(2)	1.3676(9)
O(1)-C(11)	1.4262(10)
C(9A)-C(9)	1.4014(11)
C(9A)-C(1)	1.4314(11)
C(9A)-C(4A)	1.4346(11)
C(4A)-C(9)#1	1.3968(10)
C(4A)-C(4)	1.4302(10)
C(1)-C(2)	1.3706(11)
C(1)-H(1)	0.9500
C(9)-C(4A)#1	1.3968(10)
C(9)-H(9)	0.9500
C(2)-C(3)	1.4278(11)
C(4)-C(3)	1.3604(11)
C(4)-H(4)	0.9500
C(3)-H(3)	0.9500
C(11)-H(11A)	0.9800
C(11)-H(11B)	0.9800
C(11)-H(11C)	0.9800
C(2)-O(1)-C(11)	116.55(7)
C(9)-C(9A)-C(1)	121.73(7)
C(9)-C(9A)-C(4A)	118.45(7)
C(1)-C(9A)-C(4A)	119.81(7)
C(9)#1-C(4A)-C(4)	121.59(7)
C(9)#1-C(4A)-C(9A)	120.30(7)
C(4)-C(4A)-C(9A)	118.11(7)
C(2)-C(1)-C(9A)	119.69(7)
C(2)-C(1)-H(1)	120.2
C(9A)-C(1)-H(1)	120.2
C(4A)#1-C(9)-C(9A)	121.25(7)
C(4A)#1-C(9)-H(9)	119.4
C(9A)-C(9)-H(9)	119.4
O(1)-C(2)-C(1)	125.63(8)

O(1)-C(2)-C(3)	113.63(7)
C(1)-C(2)-C(3)	120.74(7)
C(3)-C(4)-C(4A)	121.04(7)
C(3)-C(4)-H(4)	119.5
C(4A)-C(4)-H(4)	119.5
C(4)-C(3)-C(2)	120.57(7)
C(4)-C(3)-H(3)	119.7
C(2)-C(3)-H(3)	119.7
O(1)-C(11)-H(11A)	109.5
O(1)-C(11)-H(11B)	109.5
H(11A)-C(11)-H(11B)	109.5
O(1)-C(11)-H(11C)	109.5
H(11A)-C(11)-H(11C)	109.5
H(11B)-C(11)-H(11C)	109.5

Symmetry transformations used to generate equivalent atoms: #1 -x,-y,-z+2

Table 4 Anisotropic displacement parameters ($Å^2$x 10^3) for C1. The anisotropic displacement factor exponent takes the form: $-2\pi^2$[h^2 $a^{*2}U^{11}$ + ... + 2 h k a* b* U^{12}]

	U^{11}	U^{22}	U^{33}	U^{23}	U^{13}	U^{12}
O(1)	14(1)	18(1)	24(1)	-2(1)	9(1)	-2(1)
C(9A)	13(1)	12(1)	11(1)	0(1)	2(1)	0(1)
C(4A)	13(1)	13(1)	11(1)	0(1)	2(1)	1(1)
C(1)	13(1)	13(1)	15(1)	-1(1)	3(1)	-1(1)
C(9)	14(1)	11(1)	12(1)	-1(1)	3(1)	0(1)
C(2)	12(1)	16(1)	15(1)	1(1)	4(1)	0(1)
C(4)	15(1)	13(1)	14(1)	-2(1)	3(1)	1(1)
C(3)	15(1)	16(1)	16(1)	-2(1)	5(1)	2(1)
C(11)	17(1)	19(1)	28(1)	-1(1)	8(1)	-4(1)

Table 5 Hydrogen coordinates (x 10^4) and isotropic displacement parameters ($Å^2$x 10^3) for C1

	x	y	z	U(eq)
H(1)	2526	2851	9964	16
H(9)	665	3437	10956	15
H(4)	1157	-4001	7995	17
H(3)	2921	-2728	7554	19
H(11A)	3905	3895	8462	31
H(11B)	5204	2928	8701	31
H(11C)	4522	2817	10203	31

Table 6 Torsion angles [°] for C1

C(9)-C(9A)-C(4A)-C(9)#1	-0.33(13)
C(1)-C(9A)-C(4A)-C(9)#1	179.79(7)
C(9)-C(9A)-C(4A)-C(4)	178.89(7)
C(1)-C(9A)-C(4A)-C(4)	-1.00(11)
C(9)-C(9A)-C(1)-C(2)	-178.00(7)
C(4A)-C(9A)-C(1)-C(2)	1.87(12)
C(1)-C(9A)-C(9)-C(4A)#1	-179.79(7)
C(4A)-C(9A)-C(9)-C(4A)#1	0.34(13)
C(11)-O(1)-C(2)-C(1)	1.62(12)
C(11)-O(1)-C(2)-C(3)	-178.90(7)
C(9A)-C(1)-C(2)-O(1)	178.40(7)
C(9A)-C(1)-C(2)-C(3)	-1.04(12)
C(9)#1-C(4A)-C(4)-C(3)	178.47(7)
C(9A)-C(4A)-C(4)-C(3)	-0.74(12)
C(4A)-C(4)-C(3)-C(2)	1.61(12)
O(1)-C(2)-C(3)-C(4)	179.79(7)
C(1)-C(2)-C(3)-C(4)	-0.71(12)

Symmetry transformations used to generate equivalent atoms: #1 -x,-y,-z+2

Appendix B: X-Ray Structure Determination of C3 Single Crystal

A colorless thin plate fragment (0.45 x 0.30 x 0.05 mm^3) was used for the single crystal x-ray diffraction study of $C_{20}H_{22}O_2$. The crystal was mounted on to a glass fiber with epoxy resin. X-ray intensity data were collected at 296(2) K on a Bruker APEX2[31] platform-CCD x-ray diffractometer system (fine focus Mo-radiation, λ = 0.71073 Å, 50KV/30mA power). The CCD detector was placed at a distance of 5.0400 cm from the crystal.

A total of 3600 frames were collected for a sphere of reflections (with scan width of 0.3^o in ω, starting ω and 2θ angles at –30^o, and ϕ angles of 0^o, 90^o, 120^o, 180^o, 240^o and 270^o for every 600 frames, 30 sec/frame exposure time). The frames were integrated using the Bruker SAINT software package[32] and using a narrow-frame integration algorithm. Based on a monoclinic crystal system, the integrated frames yielded a total of 17073 reflections at a maximum 2θ angle of 58.26^o (0.73 Å resolution), of which 2204 were independent reflections (R_{int} = 0.0245, R_{sig} = 0.0134, redundancy = 7.7, completeness = 100%) and 1606 (72.9%) reflections were greater than 2σ(I). The unit cell parameters were, **a** = 11.9734(11) Å, **b** = 8.1643(8) Å, **c** = 8.7532(8) Å, **β** = 106.9598(13)^o, V = 818.45(13) Å^3, Z = 2, calculated density D_c = 1.195 g/cm^3. Absorption corrections were applied (absorption coefficient μ = 0.075 mm^{-1}; max/min transmission = 0.9966/0.9667) to the raw intensity data using the SADABS program[33].

The Bruker SHELXTL software package[34] was used for phase determination and structure refinement. The distribution of intensities (E^2-1 = 1.034) and systematic absent reflections indicated one possible space group, P2(1)/c. The space group P2(1)/c (#14) was later determined to be correct. Direct methods of phase determination followed by two Fourier cycles of refinement led to an electron density map from which most of the non-hydrogen atoms were identified in the asymmetry unit of the unit cell. With subsequent isotropic refinement, all of the non-hydrogen atoms were identified. There was half a molecule of $C_{20}H_{22}O_2$ present in the asymmetry unit of the unit cell. The $C_{20}H_{22}O_2$ molecule was located at the inversion center.

Atomic coordinates, isotropic and anisotropic displacement parameters of all the non-hydrogen atoms were refined by means of a full matrix least-squares procedure on F^2. The H-atoms were included in the refinement in calculated positions riding on the atoms to which they were attached. The refinement converged at R1 = 0.0412, wR2 = 0.1036, with intensity $I>2\sigma$ (I). The largest peak/hole in the final difference map was 0.195/-0.174 e/Å^3.

Table 1 Crystal data and structure refinement for C3

Empirical formula	C20 H22 O2
Formula weight	294.38
Temperature	296(2) K
Wavelength	0.71073 Å
Crystal system	Monoclinic

(to be continued)

Space group	P2(1)/c (#14)

Unit cell dimensions	a = 11.9734(11) Å	α= 90°.
	b = 8.1643(8) Å	β= 106.9598(13)°.
	c = 8.7532(8) Å	γ = 90°.
Volume	818.45(13) Å^3	
Z	2	
Density (calculated)	1.195 Mg/m^3	
Absorption coefficient	0.075 mm^{-1}	
F(000)	316	
Crystal size	0.45 x 0.30 x 0.05 mm^3	
Theta range for data collection	1.78 to 29.13°.	
Index ranges	-16<=h<=16, -11<=k<=11, -11<=l<=11	
Reflections collected	17073	
Independent reflections	2204 [R(int) = 0.0245]	
Completeness to theta = 29.13°	100.0 %	
Absorption correction	Semi-empirical from equivalents	
Max. and min. transmission	0.9966 and 0.9667	
Refinement method	Full-matrix least-squares on F^2	
Data / restraints / parameters	2204 / 0 / 101	
Goodness-of-fit on F^2	1.019	
Final R indices [I>2sigma(I)]	R1 = 0.0412, wR2 = 0.1036	
R indices (all data)	R1 = 0.0613, wR2 = 0.1191	
Largest diff. peak and hole	0.195 and -0.174 e.Å^{-3}	

Table 2 Atomic coordinates (x 10^4) and equivalent isotropic displacement parameters (Å^{2}x 10^3) for C3. U(eq) is defined as one third of the trace of the orthogonalized U^{ij} tensor.

	x	y	z	U(eq)
C(1)	8870(1)	629(1)	6706(1)	44(1)
C(2)	7788(1)	-4(1)	6020(1)	43(1)
C(3)	7228(1)	-979(2)	6928(2)	47(1)
C(4)	7759(1)	-1306(2)	8480(2)	47(1)
C(4A)	8892(1)	-673(1)	9268(1)	41(1)
C(9)	10549(1)	972(1)	9126(1)	44(1)
C(9A)	9449(1)	323(1)	8353(1)	41(1)
O(2)	7130(1)	195(1)	4474(1)	52(1)
C(11)	7624(1)	1067(2)	3408(2)	54(1)
C(12)	6760(1)	989(2)	1782(2)	63(1)
C(13)	5629(2)	1840(3)	1673(2)	90(1)

Table 3 Bond lengths [Å] and angles [°] for C3

C(1)-C(2)	1.3612(17)
C(1)-C(9A)	1.4276(17)
C(1)-H(1)	0.9300
C(2)-O(2)	1.3623(14)
C(2)-C(3)	1.4234(16)
C(3)-C(4)	1.3481(17)
C(3)-H(3)	0.9300
C(4)-C(4A)	1.4276(16)
C(4)-H(4)	0.9300
C(4A)-C(9)#1	1.3911(17)
C(4A)-C(9A)	1.4348(15)
C(9)-C(4A)#1	1.3911(17)
C(9)-C(9A)	1.3975(16)
C(9)-H(9)	0.9300
O(2)-C(11)	1.4304(15)
C(11)-C(12)	1.4973(19)
C(11)-H(11A)	0.9700
C(11)-H(11B)	0.9700
C(12)-C(13)	1.500(2)
C(12)-H(12A)	0.9700
C(12)-H(12B)	0.9700
C(13)-H(13A)	0.9600
C(13)-H(13B)	0.9600
C(13)-H(13C)	0.9600
C(2)-C(1)-C(9A)	119.93(10)
C(2)-C(1)-H(1)	120.0
C(9A)-C(1)-H(1)	120.0
C(1)-C(2)-O(2)	126.36(11)
C(1)-C(2)-C(3)	120.54(11)
O(2)-C(2)-C(3)	113.10(10)
C(4)-C(3)-C(2)	120.90(11)
C(4)-C(3)-H(3)	119.5

C(2)-C(3)-H(3)	119.5
C(3)-C(4)-C(4A)	121.15(11)
C(3)-C(4)-H(4)	119.4
C(4A)-C(4)-H(4)	119.4
C(9)#1-C(4A)-C(4)	122.26(10)
C(9)#1-C(4A)-C(9A)	119.92(10)
C(4)-C(4A)-C(9A)	117.81(11)
C(4A)#1-C(9)-C(9A)	122.02(10)
C(4A)#1-C(9)-H(9)	119.0
C(9A)-C(9)-H(9)	119.0
C(9)-C(9A)-C(1)	122.28(10)
C(9)-C(9A)-C(4A)	118.05(11)
C(1)-C(9A)-C(4A)	119.67(11)
C(2)-O(2)-C(11)	118.57(10)
O(2)-C(11)-C(12)	107.28(11)
O(2)-C(11)-H(11A)	110.3
C(12)-C(11)-H(11A)	110.3
O(2)-C(11)-H(11B)	110.3
C(12)-C(11)-H(11B)	110.3
H(11A)-C(11)-H(11B)	108.5
C(11)-C(12)-C(13)	113.61(14)
C(11)-C(12)-H(12A)	108.8
C(13)-C(12)-H(12A)	108.8
C(11)-C(12)-H(12B)	108.8
C(13)-C(12)-H(12B)	108.8
H(12A)-C(12)-H(12B)	107.7
C(12)-C(13)-H(13A)	109.5
C(12)-C(13)-H(13B)	109.5
H(13A)-C(13)-H(13B)	109.5
C(12)-C(13)-H(13C)	109.5
H(13A)-C(13)-H(13C)	109.5
H(13B)-C(13)-H(13C)	109.5

Symmetry transformations used to generate equivalent atoms: zx#1 -x+2,-y,-z+2

Table 4 Anisotropic displacement parameters ($Å^2$x 10^3) for C3.The anisotropic displacement factor exponent takes the form: $-2\pi^2$[h^2 $a^{*2}U^{11}$ + ... + 2 h k a* b* U^{12}]

	U^{11}	U^{22}	U^{33}	U^{23}	U^{13}	U^{12}
C(1)	49(1)	42(1)	47(1)	2(1)	22(1)	-3(1)
C(2)	49(1)	39(1)	44(1)	-2(1)	18(1)	0(1)
C(3)	47(1)	44(1)	53(1)	-3(1)	18(1)	-8(1)
C(4)	49(1)	44(1)	53(1)	2(1)	22(1)	-9(1)
C(4A)	43(1)	37(1)	49(1)	0(1)	21(1)	-1(1)
C(9)	46(1)	43(1)	49(1)	4(1)	23(1)	-4(1)
C(9A)	44(1)	36(1)	46(1)	0(1)	21(1)	0(1)
O(2)	55(1)	55(1)	45(1)	1(1)	14(1)	-9(1)
C(11)	57(1)	60(1)	48(1)	0(1)	21(1)	-7(1)
C(12)	74(1)	66(1)	46(1)	1(1)	16(1)	-13(1)
C(13)	72(1)	99(1)	89(1)	20(1)	7(1)	1(1)

Table 5 Hydrogen coordinates (x 10^4) and isotropic displacement parameters (Å^{2}x 10 ^{3}) for C3

	x	y	z	U(eq)
H(1)	9231	1260	6103	53
H(3)	6486	-1397	6445	57
H(4)	7380	-1956	9048	56
H(9)	10919	1624	8548	53
H(11A)	8356	569	3395	64
H(11B)	7772	2197	3749	64
H(12A)	6600	-150	1485	75
H(12B)	7106	1482	1018	75
H(13A)	5250	1304	2363	136
H(13B)	5133	1797	592	136
H(13C)	5781	2962	1995	136

Table 6 Torsion angles [°] for C3

C(9A)-C(1)-C(2)-O(2)	179.47(10)
C(9A)-C(1)-C(2)-C(3)	-0.36(17)
C(1)-C(2)-C(3)-C(4)	-0.47(18)
O(2)-C(2)-C(3)-C(4)	179.67(11)
C(2)-C(3)-C(4)-C(4A)	0.66(19)
C(3)-C(4)-C(4A)-C(9)#1	179.02(12)
C(3)-C(4)-C(4A)-C(9A)	-0.04(17)
C(4A)#1-C(9)-C(9A)-C(1)	179.85(11)
C(4A)#1-C(9)-C(9A)-C(4A)	0.26(18)
C(2)-C(1)-C(9A)-C(9)	-178.60(11)
C(2)-C(1)-C(9A)-C(4A)	0.98(17)
C(9)#1-C(4A)-C(9A)-C(9)	-0.26(18)
C(4)-C(4A)-C(9A)-C(9)	178.82(10)
C(9)#1-C(4A)-C(9A)-C(1)	-179.86(10)
C(4)-C(4A)-C(9A)-C(1)	-0.78(16)
C(1)-C(2)-O(2)-C(11)	3.94(18)
C(3)-C(2)-O(2)-C(11)	-176.21(10)
C(2)-O(2)-C(11)-C(12)	175.67(11)
O(2)-C(11)-C(12)-C(13)	63.95(16)

Symmetry transformations used to generate equivalent atoms: #1 -x+2,-y,-z+2

Appendix C: X-Ray Structure Determination of C6 single crystal

A colorless prism fragment (0.25 x 0.19 x 0.12 mm^3) was used for the single crystal x-ray diffraction study of $C_{26}H_{34}O_2$. The crystal was coated with paratone oil and mounted on to a cryo-loop glass fiber. X-ray intensity data were collected at 100(2) K on a Bruker APEX2[31] platform-CCD x-ray diffractometer system (fine focus Mo-radiation, λ = 0.71073 Å, 50KV/30mA power). The CCD detector was placed at a distance of 5.0400 cm from the crystal.

A total of 3600 frames were collected for a sphere of reflections (with scan width of 0.3^o in ω, starting ω and 2θ angles at –30^o, and ϕ angles of 0^o, 90^o, 120^o, 180^o, 240^o and 270^o for every 600 frames, 20 sec/frame exposure time). The frames were integrated using the Bruker SAINT software package[32] and using a narrow-frame integration algorithm. Based on a triclinic crystal system, the integrated frames yielded a total of 11117 reflections at a maximum 2θ angle of 56.54^o (0.75 Å resolution), of which 2660 were independent reflections (R_{int} = 0.0229, R_{sig} = 0.0171, redundancy = 4.2, completeness = 99.9%) and 2144 (80.6%) reflections were greater than 2σ(I). The unit cell parameters were, **a** = 5.9876(3) Å, **b** = 7.9678(4) Å, **c** = 11.6800(6) Å, $\boldsymbol{\alpha}$ = 85.9917(7)^o, $\boldsymbol{\beta}$ = 77.5717(7)^o, $\boldsymbol{\gamma}$ = 80.6720(7)^o, V = 536.62(5) Å^3, Z = 1, calculated density D_c = 1.171 g/cm^3. Absorption corrections were applied (absorption coefficient μ = 0.072 mm^{-1}; max/min transmission = 0.9916/0.9824) to the raw intensity data using the SADABS program[33].

The Bruker SHELXTL software package[34] was used for phase determination and structure refinement. The distribution of intensities (E^2-1 = 1.165) and no systematic absent reflections indicated two possible space groups, P-1 and P1. The space group P-1 (#2) was later determined to be correct. Direct methods of phase determination followed by two Fourier cycles of refinement led to an electron density map from which most of the non-hydrogen atoms were identified in the asymmetry unit of the unit cell. With subsequent isotropic refinement, all of the non-hydrogen atoms were identified. There was half a molecule of $C_{26}H_{34}O_2$ present in the asymmetry unit of the unit cell. The $C_{26}H_{34}O_2$ molecule was located at the inversion center.

Atomic coordinates, isotropic and anisotropic displacement parameters of all the non-hydrogen atoms were refined by means of a full matrix least-squares procedure on F^2. The H-atoms were included in the refinement in calculated positions riding on the atoms to which they were attached. The refinement converged at R1 = 0.0408, wR2 = 0.1173, with intensity I>2σ(I). The largest peak/hole in the final difference map was 0.400/-0.206 e/Å^3

Table 1 Crystal data and structure refinement for C6.

Empirical formula	C26 H34 O2
Formula weight	378.53
Temperature	100(2) K
Wavelength	0.71073 Å
Crystal system	Triclinic
Space group	P-1 (#2)

Unit cell dimensions	a = 5.9876(3) Å	α= 85.9917(7)°.
	b = 7.9678(4) Å	β= 77.5717(7)°.
	c = 11.6800(6) Å	γ = 80.6720(7)°.
Volume	536.62(5) Å^3.	
Z	1	
Density (calculated)	1.171 Mg/m^3	
Absorption coefficient	0.072 mm^{-1}	
F(000)	206	
Crystal size	0.25 x 0.19 x 0.12 mm^3	
Theta range for data collection	1.79 to 28.27°.	
Index ranges	-7<=h<=7, -10<=k<=10, -15<=l<=15	
Reflections collected	11117	
Independent reflections	2660 [R(int) = 0.0229]	
Completeness to theta = 28.27°	99.9 %	
Absorption correction	Semi-empirical from equivalents	
Max. and min. transmission	0.9916 and 0.9824	
Refinement method	Full-matrix least-squares on F^2	
Data / restraints / parameters	2660 / 0 / 128	
Goodness-of-fit on F^2	1.075	
Final R indices [I>2sigma(I)]	R1 = 0.0408, wR2 = 0.1173	
R indices (all data)	R1 = 0.0503, wR2 = 0.1264	
Largest diff. peak and hole	0.400 and -0.206 e.Å^{-3}	

Table 2 Atomic coordinates (x 10^4) and equivalent isotropic displacement parameters (Å^{2}x 10^3) for C6. U(eq) is defined as one third of the trace of the orthogonalized U^{ij} tensor.

	x	y	z	U(eq)
C(1)	2443(2)	1172(1)	2228(1)	16(1)
C(2)	3478(2)	912(1)	3174(1)	16(1)
O(1)	2460(1)	1398(1)	4292(1)	19(1)
C(11)	148(2)	2317(1)	4472(1)	18(1)
C(12)	-586(2)	2741(1)	5754(1)	18(1)
C(13)	-3021(2)	3746(1)	6033(1)	18(1)
C(14)	-3824(2)	4154(1)	7328(1)	19(1)
C(15)	-6299(2)	5085(1)	7620(1)	24(1)
C(16)	-7108(2)	5506(2)	8908(1)	31(1)
C(3)	5799(2)	63(1)	3064(1)	17(1)
C(4)	7045(2)	-479(1)	2002(1)	17(1)
C(4A)	6054(2)	-236(1)	980(1)	15(1)
C(9)	2707(2)	799(1)	115(1)	16(1)
C(9A)	3703(2)	591(1)	1105(1)	15(1)

Table 3 Bond lengths [Å] and angles [°] for C6

C(1)-C(2)	1.3671(13)
C(1)-C(9A)	1.4313(12)
C(1)-H(1)	0.9500
C(2)-O(1)	1.3704(11)
C(2)-C(3)	1.4274(13)
O(1)-C(11)	1.4367(11)
C(11)-C(12)	1.5127(12)
C(11)-H(11A)	0.9900
C(11)-H(11B)	0.9900
C(12)-C(13)	1.5254(13)
C(12)-H(12A)	0.9900
C(12)-H(12B)	0.9900
C(13)-C(14)	1.5262(13)
C(13)-H(13A)	0.9900
C(13)-H(13B)	0.9900
C(14)-C(15)	1.5245(13)
C(14)-H(14A)	0.9900
C(14)-H(14B)	0.9900
C(15)-C(16)	1.5222(15)
C(15)-H(15A)	0.9900
C(15)-H(15B)	0.9900
C(16)-H(16A)	0.9800
C(16)-H(16B)	0.9800
C(16)-H(16C)	0.9800
C(3)-C(4)	1.3608(13)
C(3)-H(3)	0.9500
C(4)-C(4A)	1.4327(12)
C(4)-H(4)	0.9500
C(4A)-C(9)#1	1.3964(13)
C(4A)-C(9A)	1.4357(13)
C(9)-C(4A)#1	1.3964(13)

C(9)-C(9A)	1.3998(12)
C(9)-H(9)	0.9500
C(2)-C(1)-C(9A)	119.68(9)
C(2)-C(1)-H(1)	120.2
C(9A)-C(1)-H(1)	120.2
C(1)-C(2)-O(1)	125.39(8)
C(1)-C(2)-C(3)	121.11(9)
O(1)-C(2)-C(3)	113.49(8)
C(2)-O(1)-C(11)	117.15(7)
O(1)-C(11)-C(12)	107.66(7)
O(1)-C(11)-H(11A)	110.2
C(12)-C(11)-H(11A)	110.2
O(1)-C(11)-H(11B)	110.2
C(12)-C(11)-H(11B)	110.2
H(11A)-C(11)-H(11B)	108.5
C(11)-C(12)-C(13)	111.72(8)
C(11)-C(12)-H(12A)	109.3
C(13)-C(12)-H(12A)	109.3
C(11)-C(12)-H(12B)	109.3
C(13)-C(12)-H(12B)	109.3
H(12A)-C(12)-H(12B)	107.9
C(12)-C(13)-C(14)	112.73(8)
C(12)-C(13)-H(13A)	109.0
C(14)-C(13)-H(13A)	109.0
C(12)-C(13)-H(13B)	109.0
C(14)-C(13)-H(13B)	109.0
H(13A)-C(13)-H(13B)	107.8
C(15)-C(14)-C(13)	112.78(8)
C(15)-C(14)-H(14A)	109.0
C(13)-C(14)-H(14A)	109.0
C(15)-C(14)-H(14B)	109.0
C(13)-C(14)-H(14B)	109.0
H(14A)-C(14)-H(14B)	107.8
C(16)-C(15)-C(14)	113.09(9)

C(16)-C(15)-H(15A)	109.0
C(14)-C(15)-H(15A)	109.0
C(16)-C(15)-H(15B)	109.0
C(14)-C(15)-H(15B)	109.0
H(15A)-C(15)-H(15B)	107.8
C(15)-C(16)-H(16A)	109.5
C(15)-C(16)-H(16B)	109.5
H(16A)-C(16)-H(16B)	109.5
C(15)-C(16)-H(16C)	109.5
H(16A)-C(16)-H(16C)	109.5
H(16B)-C(16)-H(16C)	109.5
C(4)-C(3)-C(2)	120.30(8)
C(4)-C(3)-H(3)	119.8
C(2)-C(3)-H(3)	119.8
C(3)-C(4)-C(4A)	121.06(9)
C(3)-C(4)-H(4)	119.5
C(4A)-C(4)-H(4)	119.5
C(9)#1-C(4A)-C(4)	121.98(8)
C(9)#1-C(4A)-C(9A)	119.87(8)
C(4)-C(4A)-C(9A)	118.13(8)
C(4A)#1-C(9)-C(9A)	121.66(8)
C(4A)#1-C(9)-H(9)	119.2
C(9A)-C(9)-H(9)	119.2
C(9)-C(9A)-C(1)	121.84(8)
C(9)-C(9A)-C(4A)	118.47(8)
C(1)-C(9A)-C(4A)	119.70(8)

Symmetry transformations used to generate equivalent atoms: #1 -x+1,-y,-z

Table 4 Anisotropic displacement parameters ($Å^2$x 10^3) for C6. The anisotropic displacement factor exponent takes the form: $-2\pi^2$[h^2 $a^{*2}U^{11}$ + ... + 2 h k a* b* U^{12}]

	U^{11}	U^{22}	U^{33}	U^{23}	U^{13}	U^{12}
C(1)	15(1)	17(1)	16(1)	-1(1)	-2(1)	-2(1)
C(2)	19(1)	16(1)	13(1)	-2(1)	-2(1)	-4(1)
O(1)	18(1)	25(1)	13(1)	-4(1)	-3(1)	0(1)
C(11)	17(1)	20(1)	16(1)	-2(1)	-4(1)	-2(1)
C(12)	19(1)	20(1)	14(1)	-2(1)	-3(1)	-3(1)
C(13)	18(1)	20(1)	17(1)	-1(1)	-3(1)	-2(1)
C(14)	18(1)	19(1)	19(1)	-2(1)	-2(1)	-2(1)
C(15)	21(1)	22(1)	26(1)	-3(1)	-1(1)	0(1)
C(16)	30(1)	26(1)	30(1)	-5(1)	5(1)	0(1)
C(3)	18(1)	19(1)	16(1)	0(1)	-6(1)	-4(1)
C(4)	15(1)	18(1)	17(1)	-1(1)	-5(1)	-2(1)
C(4A)	16(1)	15(1)	15(1)	0(1)	-4(1)	-4(1)
C(9)	14(1)	16(1)	16(1)	-1(1)	-3(1)	-2(1)
C(9A)	17(1)	14(1)	14(1)	0(1)	-3(1)	-4(1)

Table 5 Hydrogen coordinates (x 10^4) and isotropic displacement parameters ($Å^2$x 10 ^{3}) for C6

	x	y	z	U(eq)
H(1)	895	1737	2315	19
H(11A)	-913	1612	4263	21
H(11B)	108	3374	3974	21
H(12A)	517	3415	5956	21
H(12B)	-536	1673	6242	21
H(13A)	-4112	3081	5810	22
H(13B)	-3056	4823	5556	22
H(14A)	-3715	3081	7807	23
H(14B)	-2776	4867	7541	23
H(15A)	-6409	6154	7136	29
H(15B)	-7346	4369	7409	29
H(16A)	-6897	4464	9396	46
H(16B)	-8748	5999	9059	46
H(16C)	-6199	6326	9100	46
H(3)	6478	-125	3735	21
H(4)	8597	-1026	1939	20
H(9)	1148	1337	189	19

Table 6 Torsion angles [°] for C6

C(9A)-C(1)-C(2)-O(1)	-179.68(8)
C(9A)-C(1)-C(2)-C(3)	-0.15(14)
C(1)-C(2)-O(1)-C(11)	-2.64(14)
C(3)-C(2)-O(1)-C(11)	177.80(7)
C(2)-O(1)-C(11)-C(12)	-178.95(7)
O(1)-C(11)-C(12)-C(13)	179.17(7)
C(11)-C(12)-C(13)-C(14)	178.67(8)
C(12)-C(13)-C(14)-C(15)	-177.25(8)
C(13)-C(14)-C(15)-C(16)	-179.66(8)
C(1)-C(2)-C(3)-C(4)	1.17(14)
O(1)-C(2)-C(3)-C(4)	-179.25(8)
C(2)-C(3)-C(4)-C(4A)	-0.98(14)
C(3)-C(4)-C(4A)-C(9)#1	-179.27(9)
C(3)-C(4)-C(4A)-C(9A)	-0.19(14)
C(4A)#1-C(9)-C(9A)-C(1)	179.71(8)
C(4A)#1-C(9)-C(9A)-C(4A)	-0.47(15)
C(2)-C(1)-C(9A)-C(9)	178.80(9)
C(2)-C(1)-C(9A)-C(4A)	-1.02(14)
C(9)#1-C(4A)-C(9A)-C(9)	0.46(15)
C(4)-C(4A)-C(9A)-C(9)	-178.64(8)
C(9)#1-C(4A)-C(9A)-C(1)	-179.71(8)
C(4)-C(4A)-C(9A)-C(1)	1.19(13)

Symmetry transformations used to generate equivalent atoms: #1 -x+1,-y,-z